THE BELL SYSTEM TECHNICAL JOURNAL

DEVOTED TO THE SCIENTIFIC AND ENGINEERING ASPECTS OF ELECTRICAL COMMUNICATION

Volume 58 April 1979 Number 4

Spurious Signal Criteria for Voiceband Telephone Equipment

By G. MILLER and T. C. SPANG

(Manuscript received September 28, 1978)

A set of requirements is derived for spurious metallic and longitudinal signals generated by voiceband terminals which will assure that those signals will not interfere with other systems and services using the same multipair cable. These requirements are necessary because of the crosstalk coupling which exists between the pairs of a cable. The requirements were derived from cable crosstalk measurements and the susceptibilities to interference of voice services, program services, single channel carrier systems, and multichannel carrier systems.

I. INTRODUCTION

A customer's telephone terminal equipment is usually connected to the serving central office by a pair of wires. This pair of wires, referred to as a loop, is normally a part of a multipair cable containing 6 to 2700 pairs. Most of these pairs will be used for voice frequency service for other customers. However, pairs within this cable can be used for services such as data and broadcast program channels or systems such as subscriber loop carrier used to serve multiple customers. These other services and systems are not restricted to voiceband frequencies but can cover a frequency range from dc to several megahertz.

Pairs within a common cable sheath are in very close proximity to each other and, as a result, a small portion of the electromagnetic field, set up by the customer's communication signal, can couple into other pairs. Cable design and manufacturing techniques are used to minimize this coupling but cannot eliminate it. This coupled signal can interfere

with other signals in the cable if its level is not controlled. To control this interference, requirements are placed on the maximum allowed signal levels and administrative rules, referred to as spectrum management,[1] are used. Because of the large number of voiceband terminals, specialized administrative processes are not used for them. Such use would lead to inefficient use of cable facilities and would be economically burdensome. The interference caused by voiceband systems is controlled by requirements on the maximum allowed signal levels. These requirements provide reasonable assurance that the interference to other users will be kept to a satisfactory level without unduly affecting the customer's performance.

The output signal of a voiceband terminal can be categorized as follows:

(*i*) The desired metallic signal in the nominal 100 to 4000 Hz voiceband.

(*ii*) A sparious metallic signal above 4000 Hz.

(*iii*) A spurious longitudinal signal above 100 Hz.

This paper derives signal power limits on the two kinds of spurious signals. The maximum signal power limitations on the desired metallic signal are controlled by a different constraint, multichannel carrier overload, rather than multipair cable crosstalk. Spurious signals can cause unwanted signals into systems and services in the same cable via the crosstalk coupling between pairs. These unwanted signals generally appear as unintelligible noise-like signals. The requirements for controlling these signals are derived by considerations of (*i*) the coupling characteristics of cables and (*ii*) vulnerability to interference of systems and services which may share the same cable. The paper examines each of these considerations and concludes with a discussion of the derivation of the actual requirements for each type of spurious signal.

Limits on the output signal power of voiceband terminals that may be connected to the switched telephone network are specified in the FCC registration rules.[2] The limits on spurious signals derived in this paper are somewhat different from the existing FCC rules. On May 10, 1977 AT&T petitioned the FCC to amend its requirements on spurious signals to conform to the limits derived in this paper.[3]

II. CABLE CROSSTALK COUPLING CHARACTERISTICS

The amount of spurious signals coupled from one pair into other pairs in a multipair cable depends on the cable characteristics and the characteristics of the terminations.[4-8] The cable characteristics of importance are the design parameters such as pair twist lengths, stranding and cabling lays, and pair unbalance, and the relative positions of the pairs in the cable. In addition, the coupling is influenced

by the frequency, mode of excitation, and terminating impedances of the disturbing and the disturbed pairs.

Cable design and manufacturing techniques reduce but do not eliminate the coupling. The most significant couplings are those to the nearby or adjacent pairs. In general, pairs that are more separated have substantially reduced coupling because they are shielded from one another and because electromagnetic fields due to a signal on a wire pair decrease rapidly as the distance from that pair increases. Because of these facts, the development of signal level limitations is primarily concerned with the coupling into nearby or adjacent pairs. It is assumed that, if spurious signals from any one adjacent pair are controlled, the amount of coupling from all other pairs will be small.

The amount of coupling to nearby or adjacent pairs must be determined by measurement. Identification of that pair which will have the lowest coupling loss to a particular disturbed pair is difficult to make. Measurements of all two-pair combinations are made. Generally, the worst couplings of this distribution are those from each pair to each adjacent pair. Thus the average adjacent pair coupling can be determined from this larger distribution. Traditionally, the 1-percent worst coupling is taken as being the average adjacent pair coupling.

The mode of excitation of the applied signal greatly influences the amount of this coupling. There are two principal modes of excitation on cables; metallic and longitudinal. In cables, the two insulated conductors of the disturbing pair are twisted and close together. For metallic excitation, the currents in the two conductors are in opposite directions so that coupling to other pairs in the cable due to minor asymmetries that occur in cable manufacture is small. Crosstalk losses are large in this case. However, when a longitudinal signal is applied, the currents in the two conductors of the disturbing pair are in the same direction, with the return current in the sheath. The effect of manufacturing asymmetries on coupling is greatly increased because of the larger spacing and lack of twisting between the pairs and sheath that are carrying currents in the opposite direction. Thus, a much larger amount of interference is induced into an adjacent pair with a longitudinal signal than for an equal value of metallic signal. Coupling losses from a longitudinal signal are commonly 25 dB less than from a metallic signal. Some control is needed for crosstalk due to longitudinally induced noise signals. Usually they are at significantly lower levels than metallic signals.

As indicated, couplings between pairs in a cable must be determined by measurement. For convenience, the coupling is stated in terms of the amount of attenuation (loss) which a signal on a disturbing pair would experience in coupling to the disturbed pair. This crosstalk loss is defined as being near-end (NEXT) or far-end (FEXT). Each of these types of crosstalk is illustrated in Fig. 1. Figures 2 and 3 show smoothed

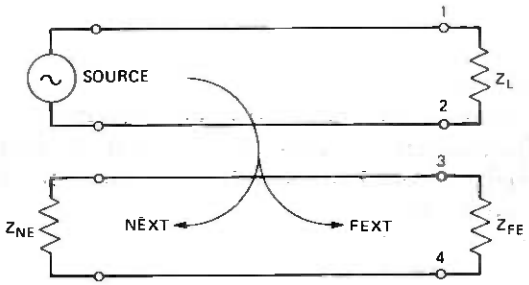

Fig. 1—Basic crosstalk circuit.

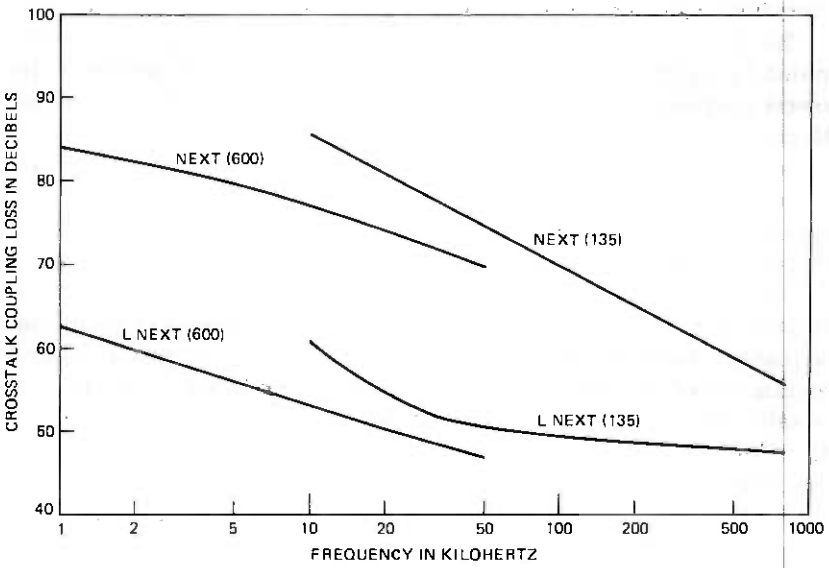

Fig. 2—One-percent metallic and longitudinal near-end crosstalk loss used in deriving the revised signal power criteria.

composite 1-percent metallic and longitudinal near-end and far-end coupling losses measured on a number of cables. Their values were used in this study. The loss is indicated in terms of the impedance of the systems which could occupy the disturbed pair. Low-frequency systems are typically designed to an impedance of 600 ohms, while at higher frequencies, systems are designed to an impedance of 135 ohms.

III. VULNERABILITY OF SYSTEMS AND SERVICES

A customer's voiceband terminal is usually assigned a cable pair at random. Thus, the customer's pair may be adjacent to a pair containing any of a large number of services and systems. The adjacent pair could contain any of the following services:

(*i*) Voiceband services.

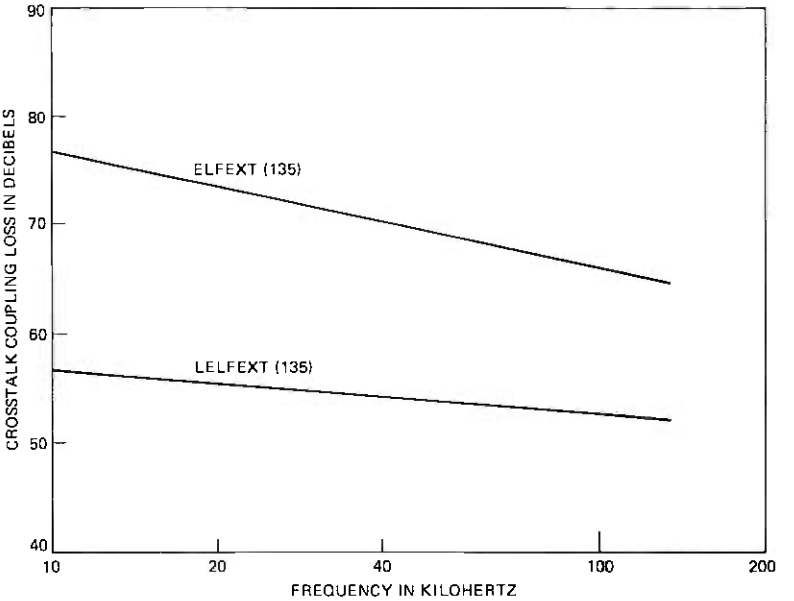

Fig. 3—One-percent metallic and longitudinal equal-level far-end crosstalk for 3 kft of cable used in deriving the revised signal power criteria.

(*ii*) Program audio transmission services.
(*iii*) Private-line, baseband data services.
(*iv*) Slow-scan, video-type services.

Carrier systems are also being increasingly used to provide more than one voice channel over a cable pair. The types of carrier systems that could be used on an adjacent pair are:

(*i*) Analog single channel loop carrier systems.
(*ii*) Analog multichannel loop and trunk carrier systems.
(*iii*) Digital multichannel loop and trunk carrier systems.

The signal power of the customer's terminal must be controlled so that performance of any of the above systems and services is not degraded. Performance of a service or system is considered degraded when the interference caused by a customer's terminal is greater than its allocated share of the service or system's noise objective. The maximum allowed value of signal power at the output of a customer's terminal is that value which causes interference in the disturbed system or service to just equal the noise allotted to interference from other systems.

The allocation is a function of the particular type of system or service. This section derives the maximum disturbing spurious signal levels for each type, considering the desired performance of the service or system, the equipment design, and crosstalk coupling. These maximum levels for spurious signals are combined into a single requirement in Section IV by considering the system or service most vulnerable to

interference at each frequency. Our current analysis indicates that carrier system considerations control the maximum allowable level above 4 kHz, while program audio and voiceband services are controlling below 4 kHz.

3.1 Voice services

Voiceband services are susceptible to interference in the frequency range from 100 Hz to 4 kHz from other voiceband terminals in the same cable. When terminals meet the metallic voiceband signal limitations as set in the FCC registration rules, the resulting noise interference into other voiceband services will not be excessive. However, signal level limitations on spurious longitudinal energy are necessary to assure protection of voiceband services in the frequency range 100 Hz to 4 kHz.

These longitudinal signal limitations depend upon the following:

(*i*) Noise requirement for voiceband service.

(*ii*) The crosstalk coupling between pairs.

The noise requirement is stated in terms of a weighted noise power across the voiceband. The maximum total noise objective for voiceband service is 20 dBrnC.[9] Half this noise is allocated to crosstalk interference; therefore, $N = 17$ dBrnC. The maximum longitudinal signal voltage that may be introduced by a voiceband terminal at any given frequency, (f), is:

$$V_S(f) = N - 92.2 - W(f) + \text{NEXT}\ (f),$$

where

$V_S(f)$ is maximum allowed single frequency longitudinal voltage on the disturbing pair in dBV.

N is the maximum permissible noise interference on the disturbed pair due to crosstalk in dBrnC. To convert this to dBV across 600 ohms, 92.2 must be subtracted.

$W(f)$ is the C-message noise weighting (see Fig. 6).

NEXT(f) is the near-end longitudinal crosstalk coupling loss in decibels (see Fig. 2).

For a signal not having all its voiceband longitudinal energy in a relatively narrow band, the single frequency maximum longitudinal voltage at any one frequency must be reduced to account for energy at other frequencies. To set proper limits on longitudinal signals that contain tones at more than one frequency in the voiceband and/or "broadband" energy, the following mathematical relationship must be satisfied:

$$N - 92.2 \leq 20 \log \int_{100}^{4000} 10^{\{[W(f) - \text{NEXT}(f) + V(f)]/20\}}\, df,$$

where $V(f)$ is the frequency spectrum of the longitudinal voltage on the disturbing pair expressed in dBV per hertz. If $V(f)$ is just a single frequency tone at some frequency f_0 and has no energy at any other frequencies, it may be treated as a delta function, the right-hand side of the above equation will reduce to $W(f_0) - \text{NEXT}(f_0) + V(f_0)$, and one obtains the constraint given previously for the single frequency tone.

The maximum single frequency allowable voltage level can be computed from the values shown in Table I. The output voltage that a signal source applies is a function of the input impedance of the cable pair it is connected to. If the maximum allowable longitudinal voltage levels are specified across an impedance that is different from the actual input impedance of the cable pair, a correction must be made. For longitudinal signals, a high impedance source was assumed and the compliance testing value was assigned a constant value of 500 ohms. Since the input impedance of a cable varies widely with frequency, an adjustment was necessary and the correction formula is:

$$\text{Impedance Correction (Longitudinal)} = 20 \log \left| \frac{Z_{in}}{500} \right|,$$

where Z_{in} is the longitudinal input impedance* of a cable as shown in Fig. 4. The impedance corrections were used in computing Table I.

3.2 Program audio transmission services

Program services are furnished over private-line, baseband circuits having a frequency range from about 30 Hz up to either 5, 8, or 15 kHz. Figure 5 illustrates the method used in implementing a typical program service, and the possible coupling of interference from a voiceband terminal. A program circuit is usually implemented using nonloaded cable with amplifiers and equalizers to compensate for the loss and frequency response characteristics of the cable.

The output of a voiceband terminal will contain its primary voiceband output signal in the frequency range from 300 Hz to 4 kHz and possibly some additional energy in the 4 to 15-kHz band. Some of the energy in both bands is coupled into the program channel and will appear as noise in that channel. Signal limitations on voiceband terminals must be specified to control this noise. A metallic voiceband signal must meet the voiceband limitations set forth in the FCC registration rules. The noise interference resulting from such a signal would be at least 10 dB below that permitted for a signal in the 4- to 15-kHz band. It would, therefore, have little influence on the total

* The longitudinal input impedance of a cable pair is the input impedance of a transmission line where one conductor is the sheath of the cable and the other is that obtained by simplexing the two conductors of that pair together.

Table I—Maximum allowable single frequency voltage levels into voice and program circuits

System	Frequency (kHz)	Noise Objective With Weighting (dBV-600Ω)	Gain of Amplifier Equalizer Combination $G(f)$ (dB)	Metallic NEXT(f) (dB)	Metallic Maximum Allowable Noise $V(f)$ Across Z_{in} (dBV)	Metallic Maximum Allowable Noise $V(f)$ Across 300Ω (dBV)	Longitudinal NEXT(f) (dB)	Longitudinal Maximum Allowable Noise $V(f)$ Across Z_{in} (dBV)	Longitudinal Maximum Allowable Noise $V(f)$ Across 500Ω (dBV)
FM Broadcast	0.1	−62.2	2.5	93.0	29.2	22.3	71.5	7.8	4.3
	0.5	−62.2	5.7	87.0	20.1	14.1	65.5	−1.4	−3.9
	1.0	−62.2	8.9	84.0	12.9	8.5	62.5	−8.6	−12.1
	2.0	−62.2	12.5	82.0	7.3	5.0	59.5	−15.1	−15.5
	4.0	−62.2	17.5	80.0	0.3	0.0	57.0	−22.7	−19.6
	6.0	−62.2	20.8	78.8	−4.2	−3.3	55.7	−27.7	−22.5
	8.0	−62.2	23.5	78.0	−7.7	−5.4	54.0	−31.6	−25.1
	10.0	−62.2	25.8	77.0	−11.0	−8.5	53.3	−34.8	−26.8
	12.5	−61.5	28.1	76.0	−13.6	−10.0	52.3	−37.3	−28.6
	15.0	−58.7	30.0	75.0	−13.7	−10.0	51.5	−37.2	−27.8
AM 8 kHz	0.1	−33.2	3.0	93.0	56.2	49.2	71.5	34.7	31.2
	0.5	−53.2	7.0	87.0	26.2	20.2	65.5	4.7	1.2
	1.0	−59.2	11.1	84.0	13.7	9.3	62.5	−7.8	−11.3
	2.0	−63.0	15.9	82.0	3.1	0.4	59.5	−19.3	−19.7
	4.0	−65.3	22.3	80.0	−7.6	−7.9	57.0	−30.6	−27.5
	6.0	−64.8	26.5	78.8	−12.5	−11.6	55.7	−36.0	−31.0
	8.0	−60.6	30.0	78.0	−12.6	−10.5	54.0	−36.5	−30.0
AM 5 kHz	0.1	−33.2	3.5	93.0	56.3	49.3	71.5	34.8	31.3
	0.5	−53.2	7.5	87.0	26.3	20.3	65.5	4.8	1.3
	1.0	−59.2	12.0	84.0	12.8	8.4	62.5	−8.7	−12.2
	2.0	−63.0	17.1	82.0	1.9	−0.4	59.5	−10.5	−20.9
	4.0	−65.3	24.0	80.0	−9.3	−9.6	57.0	−32.3	−29.2
	5.0	−65.2	26.2	79.3	−12.1	−11.8	56.0	−35.3	−31.1
Voice	0.1	−32.7	—				71.5	38.8	35.3
	0.5	−67.7	—				65.5	−2.2	−5.7
	1.0	−75.2	—		Not Applicable		62.5	−12.7	−16.2
	2.0	−73.9	—				59.5	−14.4	−14.8
	3.0	−72.7	—				58.0	−14.7	−13.2
	4.0	−60.7	—				57.0	3.8	6.8

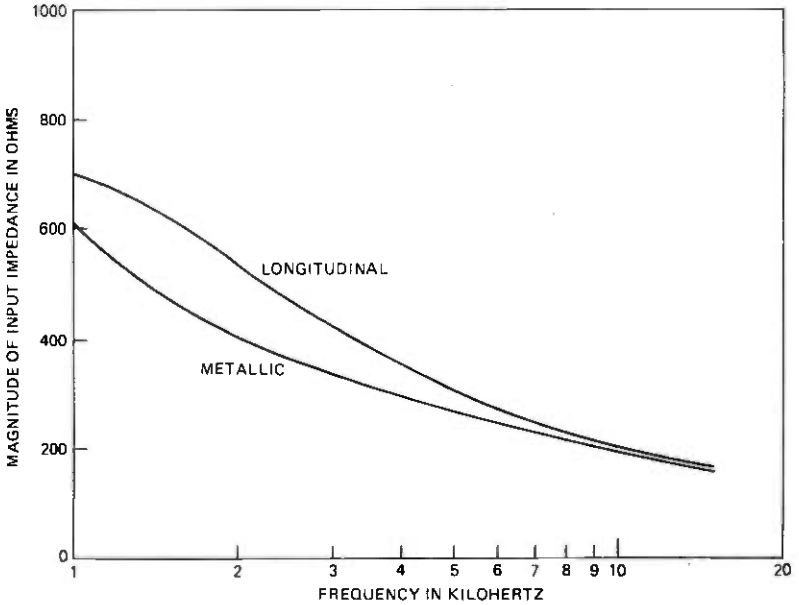

Fig. 4—Metallic input impedance of 5.5 miles of 22-gauge cable terminated in 600 ohms and longitudinal input impedance of 6 miles of 26 gauge cable terminated in 100 ohms.

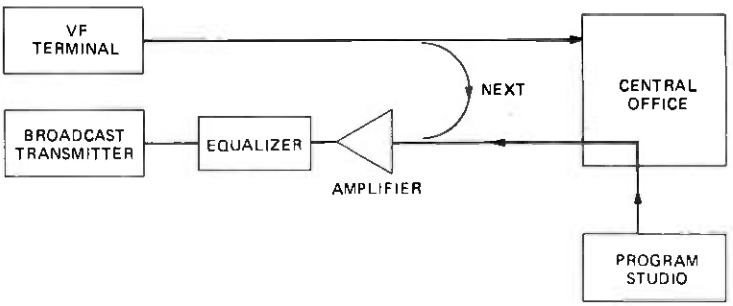

Fig. 5—Noise interference model for program circuit.

noise power in the program channel. Thus, the metallic signal limitation need be examined only in the 4- to 15-kHz band. However, signal level limitations on spurious longitudinal energy must be considered both for the voiceband as well as the 4- to 15-kHz band.

The following factors must be examined in developing the signal limitation:

(*i*) Noise requirement for program service.

(*ii*) The crosstalk coupling between cable pairs.

(*iii*) Gain of the amplifier.

(*iv*) Frequency shaping of the equalizer.

The maximum total noise levels permitted for AM, FM, and TV audio are set forth in Part 73 of the FCC Rules and Regulations[10] applicable to the broadcast industry. Noise induced on common carrier services carrying broadcast material must be below these levels. The allocation of noise requirements is shown in Table II. The terms "program" and "15 kHz flat" refer to the weighting filter used in measuring the noise with a Western Electric Type 3 noise measuring set. The weighting filter frequency characteristics are shown in Fig. 6.

Program circuits are implemented with amplifiers and equalizers which are spaced at the lesser distance corresponding to 30-dB loss at the highest channel frequency, or 12-dB loss at 1000 Hz. Application of this requirement results in the spacing of the amplifier-equalizer combinations shown in Table III.

Throughout their bandwidth, program circuits are designed to have an end-to-end loss or attenuation distortion of not greater than ±1 dB. To achieve this, the combination of the amplifier and equalizer has a gain characteristic shown in Fig. 7.

The maximum out-of-band metallic or longitudinal signal voltage is obtained in the same manner as the maximum allowable voiceband longitudinal signal. In this case, the single frequency maximum voltage is given by the equation:

$$V_S(f) = N - W(f) - G(f) + \text{NEXT}(f),$$

where

$V_S(f)$ is the maximum allowed single frequency metallic or longitudinal voltage on the disturbing pair in dBV.

Table II—Noise requirements allocation

	Total Circuit Requirement		Allocation for Crosstalk	
	dBrn	dBm	dBm	dBV (600 ohm)*
AM (5 kHz or 8 kHz) program	36	−54	−57	−59.2
FM 15 kHz flat	33	−57	−60	−62.2
TV audio 15 kHz flat	38	−52	−55	−57.2

* dBV is dB relative to 1 volt and is related to dBm by the formula dBV = dBm − 2.2 across 600 ohms.

Table III—Amplifier-equalizer combinations

	Cable Gauge	
Type of Circuit	22	24
AM 5 kHz	6.6 mi	4.9 mi
AM 8 kHz	6.9 mi	5.1 mi
FM and TV 15 kHz	5.5 mi	4.0 mi

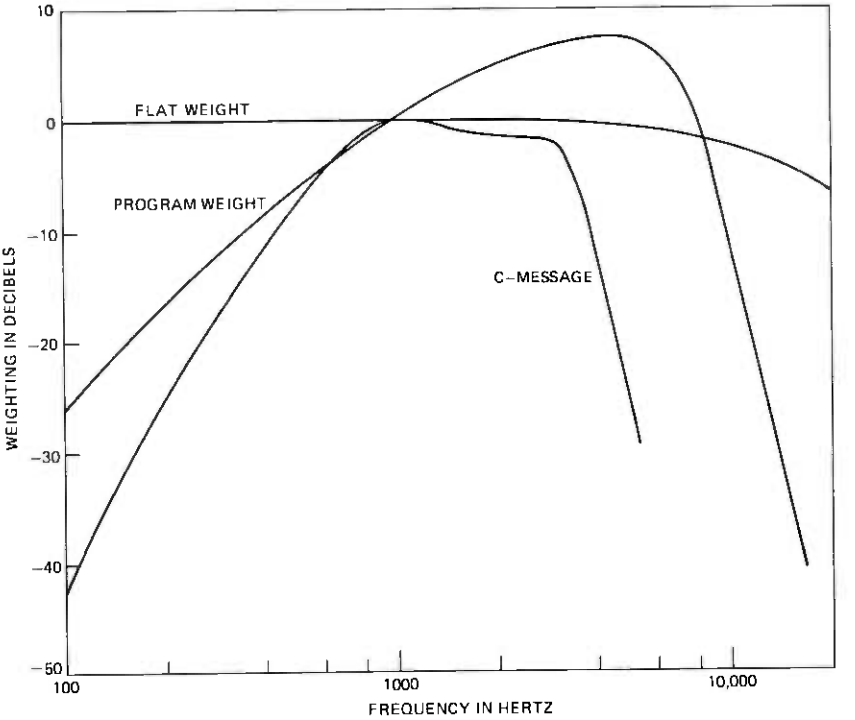

Fig. 6—3A noise measuring set program, C-message, and flat weighting curves.

N is the maximum permissible noise interference on the disturbed pair due to crosstalk in dBV.
$W(f)$ is noise weighting in dB.
$G(f)$ is gain of the amplifier and equalizer in dB.
NEXT(f) is the near-end metallic or longitudinal crosstalk coupling loss in decibels.

At the maximum repeater spacing, the maximum allowed voltage is independent of the cable gauge used in implementing the circuit since $G(f)$ and NEXT(f) are not functions of gauge. Table I shows the results of this computation by frequency for metallic and longitudinal signals.

These maximum allowable voltage levels are computed at the input to a cable pair. They may be specified across the input impedance of the cable which varies widely with frequency or, to simplify the overall requirement, a constant value of 300 ohms may be used for metallic voltages and a correction made in the maximum allowable voltages to account for impedance variation. Assuming the voice terminal has a source impedance for metallic signals of 600 ohms, the difference in dBV between the voltage measured across a 300-ohm load and the

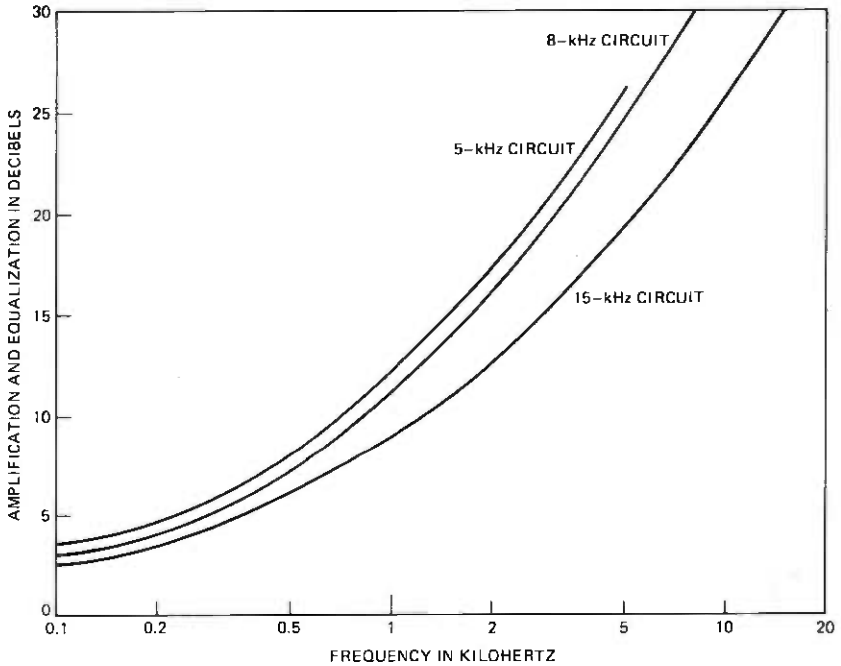

Fig. 7—Gain of amplifier-equalizer combination for 5-, 8-, and 15-kHz program circuits.

input impedance of the cable is:

$$\text{Impedance Correction (Metallic)} = 20 \log \left| \frac{Z_{in}(f) + 600}{3Z_{in}(f)} \right|.$$

$Z_{in}(f)$ for 22 gauge cable is shown in Fig. 4. For longitudinal signals, the same approach was used as for voice service. These impedance corrections were used in computing the results shown in Table I.

3.3 Private-line baseband data services and digital multichannel carrier systems

The number of baseband and high-speed data services and digital carrier systems present in the same cables with voiceband services is constantly increasing. These systems, however, are not as prone to noise interference as analog services and carrier systems. For digital carrier systems, information is represented in terms of 0 or 1 bits, which are sent as pulse or no pulse signals. To interfere with a digital system, the noise must be sufficiently high to hamper the pulse/no pulse decision process. This must be a relatively higher level of noise than that required to interfere with analog services and carrier systems if the noise is spread over a reasonable time period. However, it is possible if the interference is concentrated in a relatively short time

period, as a noise spike, to cause interference into a data service or digital carrier system but meet the average noise requirement for analog systems. To avoid this problem, the final requirement was formulated in terms of the rms voltage rather than an average voltage.

3.4 Analog single and multichannel carrier systems

Increasingly greater use is being made of analog carrier systems to provide more than one voiceband telecommunication channel over a cable pair. These systems, known as subscriber loop carrier systems, are of two classes: single channel systems and multichannel systems.* These systems are susceptible to interference from about 4 kHz up to 1 MHz. Voiceband terminal equipment may emit energy in this frequency range along with its primary voiceband energy. A portion of this spurious high frequency energy will be introduced into adjacent pairs in the same cable through crosstalk coupling. Hence, both a desired signal and an interfering signal appear at the input to the receiving carrier terminal. This composite signal is demodulated in the receiving carrier terminal (by a process analogous to that occurring in an AM radio receiver) and appears at the output of the carrier terminal as a voice signal plus noise. Thus, the customer whose service is provided over the carrier system will experience degradation of service by this noise signal which originally was in the 4-kHz to 1-MHz frequency band. In *N*3 carrier systems, in addition to increased channel noise, excessive signal or tones at or near any of its 24 nominal carrier frequencies may "beat" with the carrier. This will cause a slow variation in the amplitude of the derived channel and will be perceived by the customer as variations in volume of the conversation.

Single and multichannel carrier systems that conform to REA[11] (Rural Electrical Administration) specifications use the frequency band between 4 and 60 kHz for communication from the subscriber terminal to the central office and frequencies above 60 kHz for transmission from the central office to the subscriber.† Spurious energy in the frequency range from 4 to 60 kHz will interfere with the signal transmitted toward the central office, while energy above 60 kHz will interfere with the signal transmitted toward the subscriber.

For convenience, interference into a carrier system will be classified into three types. Figures 8 and 9 depict the two types of interference which may occur at the central office. In Type 1 interference (Fig. 8), energy in the 4- to 60-kHz band is coupled via far-end crosstalk into the carrier receiver. In Type 2 interference (Fig. 9), energy from a far-

* Multichannel subscriber systems typically provide services to 6 to 8 customers. In addition, *N*3 and *T*1 carrier systems may be used in subscriber loop plant to provide larger numbers of channels.

† In some multichannel carrier systems, the lower frequency band may be extended to 76 kHz.

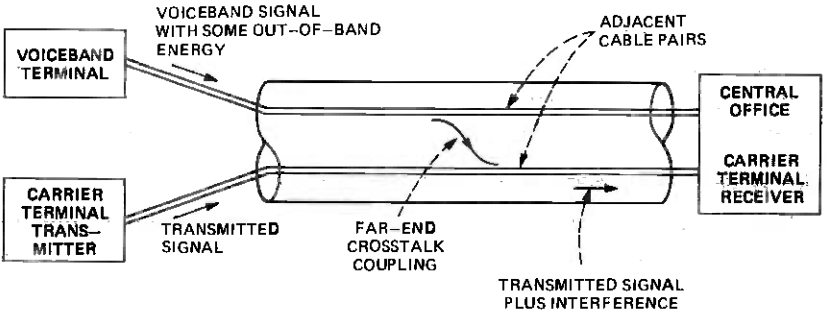

Fig. 8—Type 1 interference-voiceband terminal interfering with carrier system at central office terminal.

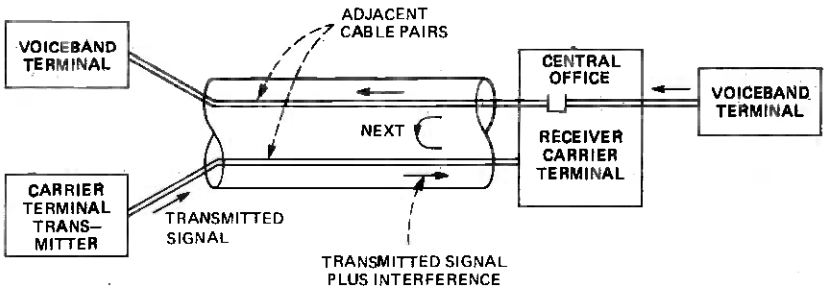

Fig. 9—Type 2 interference—voiceband terminal interfering with carrier system at central office terminal via near-end crosstalk.

end voiceband terminal is coupled via near-end crosstalk at the central office to a carrier terminal. The interference to the carrier system in this case is particularly insidious because the spurious noise source could be any loop connected to the central office. In Type 3 interference (Fig. 10), spurious energy above 60 kHz can interfere with the remote carrier terminal. In this case, the energy is coupled into the carrier system due to near-end crosstalk.

Depending upon the type of carrier system and the frequency spectrum of the out-of-band interference, one of these three types of interference will determine the maximum disturbing signal level that may be applied by a voiceband terminal. The approach taken in developing the appropriate limitations was to quantitatively determine for each type of carrier system the value of the disturbing signal which causes the noise in the disturbed channel to equal its system noise objective. The systems considered were typical of each of the classes of carrier systems. The classes considered were noncompandored and compandored single channel carrier systems, multichannel carrier systems, and the *N*3 carrier system.

The amount of induced noise will depend on the following factors:

(*i*) The frequency spectrum of the voiceband terminal output.

(*ii*) The physical layout of the cable.

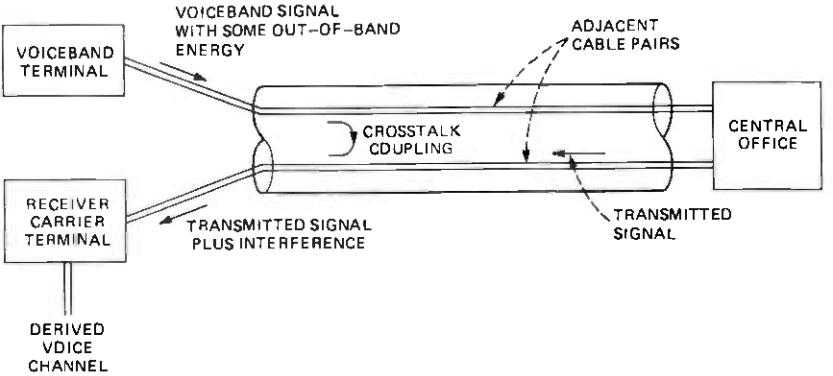

Fig. 10—Type 3 interference-voiceband terminal interfering with carrier system at remote terminal.

(*iii*) The design of the carrier system.

(*iv*) The interference path loss.

The following sections present the noise objectives and discuss each of the above factors. The values used for these factors in deriving maximum allowable levels are summarized in Tables IV, V, and VI.

3.4.1 Frequency spectrum of voiceband terminal output

The receivers for all analog carrier systems are designed to receive only the energy present on the line in a narrow band about the carrier for that channel. The amount of energy present in that channel will depend on the frequency spectrum of the interfering signal from the voiceband terminal. For instance, a terminal whose frequency spectrum decreases more rapidly at higher frequencies may interject less noise than a terminal having a relatively flat spectrum. For single channel and multichannel carrier systems, which are double-sideband, amplitude-modulated systems, the narrow band for receiving noise is that 8-kHz band occupied by each channel. *N*3 carrier, on the other hand, being a single sideband amplitude modulation system, has a band that is 4 kHz wide.

In addition to its susceptibility to random noise in these 4-kHz bands, the *N*3 carrier system is susceptible to "beats" at each of its 24 carrier frequencies. Beat interference may occur when the interfering tones are within a few hertz of the carrier frequencies. To meet the overall *N*3 system beat objective, a carrier-to-intersystem interference ratio of at least 51 dB is required.* Since energy is also present from the voiceband signal being carried on the *N*3 channel, spurious signals at or near the carrier frequency must be at least 53 dB below the power of the carrier signal at the input to the carrier system's gain regulator.

* The beat objective for *N*3 carrier is the same as that for *N*2 carrier derived in Ref. 12.

Table IV—Maximum allowable random noise signal into single channel and multichannel carrier systems

System	Controlling Interference Types	Frequency Band (kHz)	Received Carrier Level (dBm)	Noise Objective (dBrnC)	Susceptibility to Noise dBV-(135Ω)	Metallic		Longitudinal	
						Interference Path Loss (dB)	Maximum Allowable Noise dBV-(135Ω)	Interference Path Loss (dB)	Maximum Allowable Noise dBV-(90Ω)
NSCC	1	24–32	−18	20	−97	75	−22	55	−42
	3	72–80	−39	20	−118	72	−46	50	−68
CSCC	2	24–32	−40	20	−121	86	−35	59	−56
	3	72–80	−47	20	−96	72	−24	50	−46
MCC1	1	12–20	−40	15	−97	77	−20	56	−41
		20–28	−40	15	−97	76	−21	55	−42
		28–36	−40	15	−97	75	−22	54	−43
		36–44	−40	15	−97	74	−23	54	−43
		44–52	−40	15	−97	73	−24	54	−43
		52–60	−40	15	−97	73	−24	54	−43
	3	72–80	−42	15	−99	72	−27	50	−49
		80–88	−41	15	−98	71	−27	49	−49
		88–96	−41	15	−98	70	−28	49	−49
		96–104	−41	15	−98	69	−29	49	−49
		104–112	−41	15	−98	69	−29	49	−49
		112–120	−40	15	−97	68	−30	49	−48
MCC2	1	8–16	−40	15	−96	78	−18	57	−39
		16–24	−40	15	−96	77	−19	56	−40
		24–32	−40	15	−96	76	−20	55	−41
		32–40	−40	15	−96	75	−21	55	−41
		40–48	−40	15	−96	74	−22	54	−42
		48–56	−40	15	−96	73	−23	54	−42
		56–64	−40	15	−96	73	−23	53	−43
		64–72	−40	15	−96	72	−24	53	−43
	3	92–100	−40	15	−93	70	−23	49	−44
		100–108	−40	15	−93	69	−24	49	−44
		108–116	−40	15	−93	69	−24	49	−44
		116–124	−40	15	−93	68	−25	49	−44
		124–132	−40	15	−93	68	−25	49	−44
		132–140	−40	15	−93	67	−26	49	−44
		140–148	−40	15	−93	67	−26	49	−44
		148–156	−40	15	−93	67	−26	48	−45
MCC3	1	4–12	−40	15	−96	79	−17	61	−37

Table V—Maximum allowable random noise signal into N3

System	Frequency Band (kHz)	Minimum Received Carrier Level (dBm)	Noise Objective (dBrnC)	Susceptibility to Random Noise (dBv-135Ω)	Metallic		Longitudinal	
					Interference Path Loss (dB)	Maximum Allowable Signal (dBv-135Ω)	Interference Path Loss (dB)	Maximum Allowable Signal (dBv-90Ω)
N3	40 ± 4	−41	20	−84	81	−3	56	−28
	48 ± 4	−41	20	−84	81	−3	56	−28
	56 ± 4	−42	20	−85	80	−5	56	−29
	64 ± 4	−43	20	−86	79	−7	56	−30
	72 ± 4	−44	20	−87	78	−9	56	−31
	80 ± 4	−45	20	−88	78	−10	56	−32
	88 ± 4	−46	20	−89	78	−11	56	−33
	96 ± 4	−47	20	−90	77	−13	56	−34
	104 ± 4	−48	20	−91	76	−15	56	−35
	112 ± 4	−49	20	−92	76	−16	56	−36
	120 ± 4	−50	20	−93	75	−18	56	−37
	128 ± 4	−51	20	−94	75	−19	56	−38
	176 ± 4	−52	20	−95	73	−22	56	−39
	184 ± 4	−53	20	−96	73	−23	56	−40
	192 ± 4	−53	20	−96	73	−23	56	−40
	200 ± 4	−54	20	−97	73	−24	56	−41
	208 ± 4	−54	20	−97	72	−25	56	−41
	216 ± 4	−55	20	−98	72	−26	56	−42
	224 ± 4	−55	20	−98	72	−26	56	−42
	232 ± 4	−56	20	−99	72	−27	57	−42
	240 ± 4	−56	20	−99	72	−27	57	−42
	248 ± 4	−57	20	−100	72	−28	57	−43
	256 ± 4	−57	20	−100	72	−28	57	−43
	264 ± 4	−58	20	−101	72	−28	57	−44

Table VI—Maximum allowable single frequency levels that will not cause excessive beat interference with N3 carrier systems

System	Frequency Band (kHz)	Minimum Received Carrier Level (dBm)	Interference-to-Carrier Ratio to Meet Beat Objective (dB)	Susceptibility to Tones (dBv-135Ω)	Metallic		Longitudinal	
					Interference Path Loss (dB)	Maximum Allowable Tone (dBv-135Ω)	Interference Path Loss (dB)	Maximum Allowable Tone (dBv-90Ω)
N3	40 ± .1	−41	−53	−103	81	−22	56	−47
	48 ± .1	−41	−53	−103	81	−22	56	−47
	56 ± .1	−42	−53	−104	80	−24	56	−48
	64 ± .1	−43	−53	−105	79	−26	56	−49
	72 ± .1	−44	−53	−106	78	−28	56	−50
	80 ± .1	−45	−53	−107	78	−29	56	−51
	88 ± .1	−46	−53	−108	78	−30	56	−52
	96 ± .1	−47	−53	−109	77	−32	56	−53
	104 ± .1	−48	−53	−110	76	−34	56	−54
	112 ± .1	−49	−53	−111	76	−35	56	−55
	120 ± .1	−50	−53	−112	75	−37	56	−56
	128 ± .1	−51	−53	−113	75	−38	56	−57
	176 ± .1	−52	−53	−114	73	−41	56	−58
	184 ± .1	−53	−53	−115	73	−42	56	−59
	192 ± .1	−53	−53	−115	73	−42	56	−59
	200 ± .1	−54	−53	−116	73	−43	56	−60
	208 ± .1	−54	−53	−116	72	−44	56	−60
	216 ± .1	−55	−53	−117	72	−45	56	−61
	224 ± .1	−55	−53	−117	72	−45	56	−61
	232 ± .1	−56	−53	−118	72	−46	57	−61
	240 ± .1	−56	−53	−118	72	−46	57	−61
	248 ± .1	−57	−53	−119	72	−47	57	−62
	256 ± .1	−57	−53	−119	72	−47	57	−62
	264 ± .1	−58	−53	−120	72	−48	57	−63

3.4.2 Physical layout of cable

The transmitted carrier signal will be attenuated by the cable. The amount of attenuation to the receiver will depend upon the cable gauge and length between the carrier transmitter and receiver. The receiver increases its gain in proportion to the attenuation, thus increasing its sensitivity to noise. Hence, for interference Types 2 and 3 (see Figs. 9 and 10), the carrier terminal will be more sensitive to a disturbing signal when used on longer length cable. To assure that these types of interference do not exceed the noise objective for all applications of the carrier system, the carrier system must be evaluated where the system is operating at its longest design length.

For Type 1 interference, the carrier signal and the interference simultaneously decrease for longer length cable. To assure that this type of interference remains below the noise objective, the carrier system needs to be evaluated for those applications where the ratio of the interference signal-to-carrier signal is a maximum. This ratio was calculated under the following conditions:

(*i*) The voiceband terminal is located 3.5 kft from the central office, and

(*ii*) for single channel carrier systems, the carrier terminal is located in close proximity to the voiceband terminal, or

(*iii*) for multichannel carrier systems, the carrier terminal is located at least 3.5 kft from the central office.

3.4.3 Design of the carrier system

The characteristics of the receiving carrier terminal control the conversion of the incoming high-frequency signal into a voice frequency output. The characteristics that need to be considered are: the lowest expected received carrier level, the type of modulation used (single or double sideband), the demodulation efficiency, and compandor efficiency, if used.* Based on these characteristics, the maximum allowable interfering signal level can be calculated on the disturbed pair which will cause the voice frequency channel to equal its noise objective. This signal level is called the "susceptibility" of the system and is expressed in dBm.

The susceptibility is a function of the receiver characteristics. The response of a carrier receiver to noise is of the form:

$$P_0 = P_I - P_c + K,$$

where P_0, P_I, and P_c are the power levels in dBm of the receiver

* A compandor is used to reduce the effect of noise induced in the cable. This device compresses the range of the speech signal at the transmitting terminal and expands it back at the receiver.

output, the interfering noise in the sideband(s), and the carrier, respectively. The constant K depends on the particular receiver and compandor characteristics.* Once the value of K has been established for a particular system, the susceptibility of any particular system may be determined by solving for P_I with the output power P_0 of the receiver equal to the noise objective, and the carrier power P_c equal to the received carrier level.†

The noise objective for a carrier system depends on its application. The overall loop noise objective is 20 dBrnC. With a single channel system, the remote carrier terminal is normally located on the customer's premises. The channel noise objective for a single channel system, therefore, equals the loop noise objective. For a multichannel carrier system (MCC), the remote carrier terminal is usually located some distance from the customer's premises. Therefore, 15 dBrnC is allocated to that portion of the loop between the central office and the MCC remote terminal. This allocation allows for the additional noise occurring on the remaining portion of the loop from the MCC terminal to the customer's premises. The random noise objective for *N*3 carrier is the trunk noise objective of 28 dBrnC.[13] The allocation for intersystem interference is 20 dBrnC.

3.4.4 Interference path loss

The amount of noise introduced into a particular carrier system depends on the interference path loss between the disturbing and disturbed pairs. The interference path loss (IPL) in decibels is defined as:

$$\text{IPL} = 20 \log \frac{V_2}{V_1},$$

where

V_1 is the voltage appearing on the disturbed pair,
V_2 is the voltage of the signal applied by the disturbing voice terminal.

This loss is primarily due to the crosstalk coupling loss. However, pairs in close proximity to one another within the cable do not always

---

* The susceptibility in dBm is converted to dBV by subtracting 9 dB, since the nominal impedance of a carrier terminal is approximately 135 ohms and

$$\text{dBV} = \text{dBm} - 10 \log \frac{1000}{R} = \text{dBm} - 9$$

at 135 ohms.

† *N*3 carrier, all multichannel loop carriers, and some single channel loop carrier systems are compandored. Typically, a compandor will give a system an additional 30-dB noise advantage.

terminate at the same physical location. Thus, path loss can consist of the following two components:

(*i*) Crosstalk coupling loss.

(*ii*) Cable attenuation to the point of crosstalk exposure.

For Type 1 interference, the interference path loss is equal to the far-end coupling loss. As the length of the cable increases from the central office, far-end coupling loss will first decrease due to the increased amount of exposure between pairs and then begin to increase due to cable attenuation of the coupled signal. The coupling loss will be a minimum at about 3.5 kft. For Type 2 interference, the path loss is equal to the near-end crosstalk coupling loss plus the loss through the office and the cable to the voiceband terminal. To assure that the noise objective for the carrier system would not be exceeded, the cable attenuation for a short loop (2 kft, 26 gauge) was used.

For Type 3 interference, the path loss is equal to the near-end coupling loss plus the added loss between the point of crosstalk exposure and the voiceband terminal. Usually this added loss will be zero. In most instances, the voiceband terminal and the carrier terminal will be in relatively close proximity. This is because binder groups of 50 to 100 pairs would normally be assigned to serve neighboring homes, or adjacent businesses. On the other hand, for the *N*3 carrier systems, the carrier terminal is usually not located in close proximity to the voiceband terminal. Thus, it was assumed that at least 2 kft of cable exists between the disturbing terminal and the *N*3 carrier terminal.

3.4.5 Calculation of the maximum allowable voltages

The maximum allowable disturbing metallic and longitudinal voltages were calculated for each of the three types of interference for the single channel, multichannel, and *N*3 systems. The formula used was:

$$\text{Maximum voltage} = \text{Susceptibility} + \text{Interference Path Loss}.$$

At a given frequency, one of the types of interference was found to be controlling. Tables IV, V, and VI present the values for the controlling type of interference for each of the systems.

IV. DEVELOPMENT OF THE METALLIC AND LONGITUDINAL REQUIREMENTS

Section III developed the maximum allowable metallic and longitudinal disturbing signals for each of the systems considered. These calculated values above 4 kHz are graphically depicted as a function of frequency in Figs. 11 and 12. Figure 13 depicts the calculated longitudinal values between 100 Hz and 4 kHz. In each of these curves, the line segments represent the frequency band over which the voltage is applicable. For instance, in Fig. 11 the maximum allowable metallic

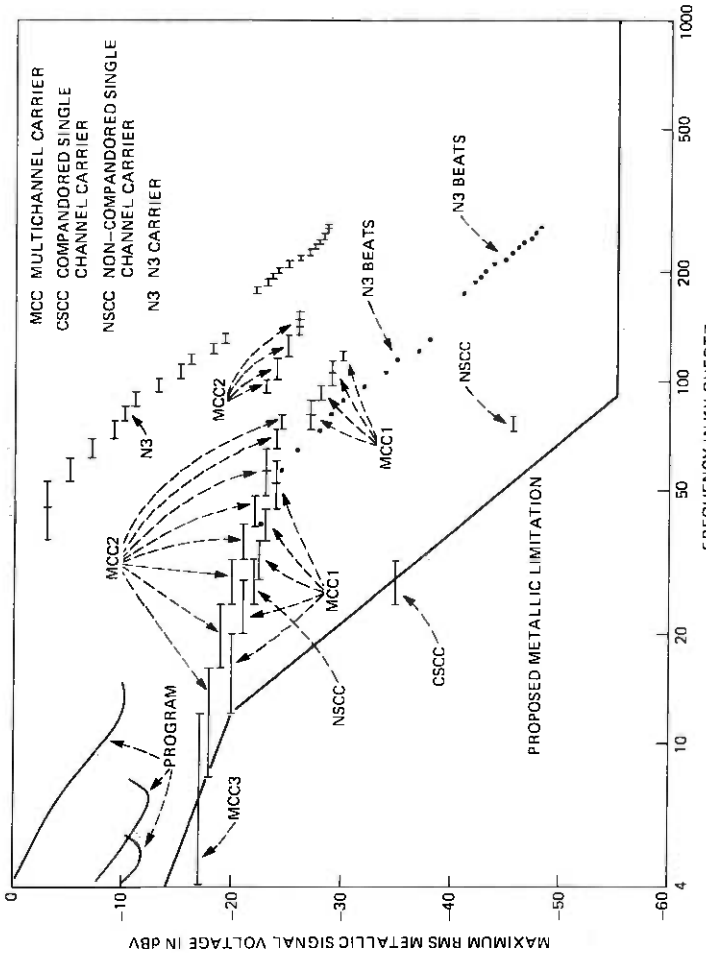

Fig. 11—Maximum permissible metallic voltage from 4 kHz to 1 MHz.

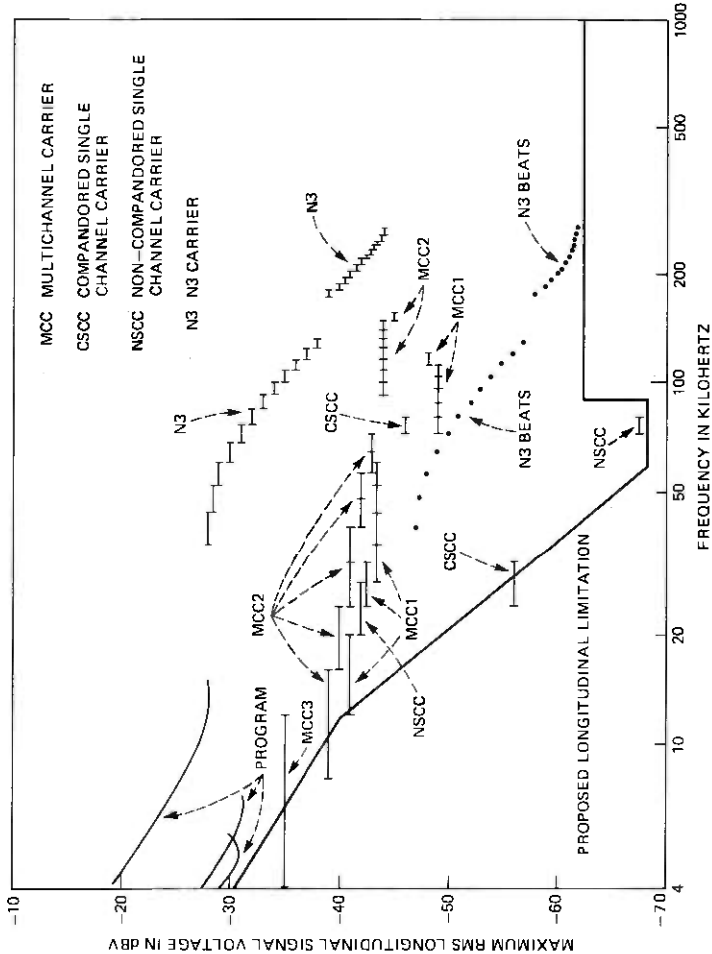

Fig. 12—Maximum permissible longitudinal voltage from 4 kHz to 1 MHz.

disturbing signal for a typical compandored single channel carrier system (CSCC) is −35 dBV between 24 kHz and 32 kHz.

The systems depicted on the figures are only examples of systems which could use this band. Other systems can and will be developed which have similar sensitivities but use different frequencies. Thus, requirements applicable over the entire band are needed. A requirement is needed to protect voice in the 100-Hz to 4-kHz band and to protect program circuits in the 100-Hz to 15-kHz band. Above 4 kHz, a requirement is needed which limits the total power into carrier systems.

As indicated in Figs. 11 and 12, the maximum allowable metallic and longitudinal voltage required to protect multichannel subscriber carrier systems (MCC1, MCC2 and MCC3) between 4 kHz and 15 kHz is sufficient to protect program circuits. Thus, the requirements from 100 Hz to 4 kHz are based on the susceptibility of voice and program services and from 4 kHz to 1 MHz, on the susceptibility of carrier systems.

The longitudinal requirement in the band from 100 Hz to 4 kHz was developed based on the maximum allowable voltages indicated in Fig. 13. This figure depicts the loci of the maximum allowable signal levels as a function of frequency for narrowband noise signals such as single frequency tones for program services and voice service. The voltage limitation which would satisfy all of these requirements is indicated on this figure. This voltage limitation curve permits a signal having frequency components near 100 Hz to be applied at a higher level than

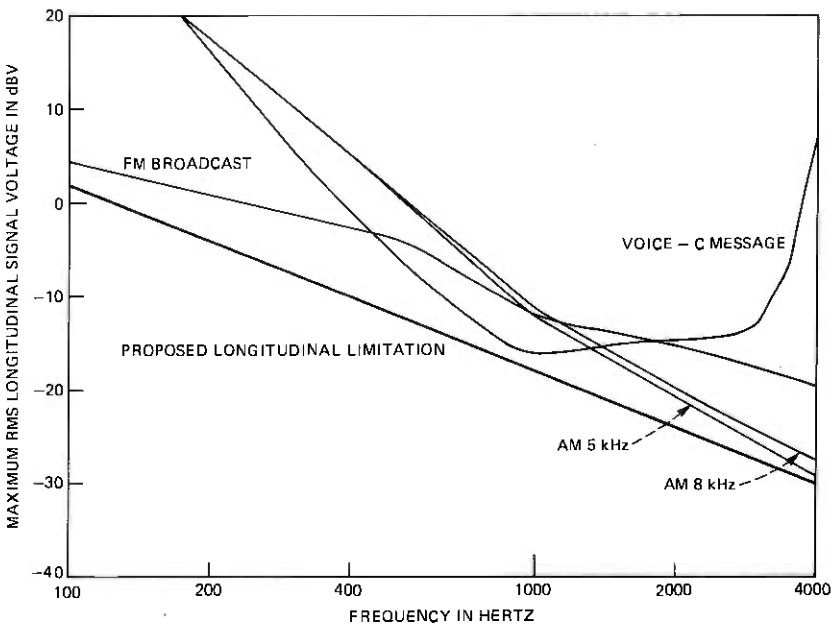

Fig. 13—Maximum permissible longitudinal voltage from 100 Hz to 4 kHz.

one having components near 4 kHz. To allow maximum flexibility for signals having relatively narrow bandwidths and yet control the total noise power in the program channel for signals having energy over the entire band, a weighting filter approach was developed. This approach achieves the relationship given by the integral in Section 3.1. With this approach, a signal in the 100-Hz to 4-kHz band is applied to a filter. The rms voltage at the output of the filter is measured to determine compliance with the criteria. The desired filter frequency transfer characteristics is the inverse of this voltage limitation.

In the 4-kHz to 1-MHz band, requirements are needed to limit the total power into carrier systems. Carrier systems are sensitive to noise in 8-kHz bands centered about their carrier frequencies. Since the frequencies of the carriers can be assigned anywhere within the 4-kHz to 1-MHz frequency range, the requirement must be stated over all possible 8-kHz bands. The magnitude of the maximum allowable voltage decreases with increasing frequency. The proposed metallic and longitudinal limitations in this band must be chosen to be at least equal to the maximum allowable voltages required by each of the systems.

At frequencies above 50 kHz, metallic voltage levels must be limited to values slightly lower than those determined solely by the foregoing carrier system metallic signal level susceptibility considerations. At these frequencies, the longitudinal balance of a series or parallel connected device is difficult to control. The longitudinal balance for many devices will decrease to close to 6 dB above 50 kHz. Spurious high-frequency metallic voltage applied by a voiceband terminal which is connected to a cable pair having at least one other terminal device on it will be converted into a longitudinal signal due to such imbalance. If the applied metallic voltage level was equal to a requirement based only on metallic carrier system susceptibility, the resulting longitudinal signal would exceed the maximum allowable longitudinal signal level specified in Fig. 12. The metallic signal voltage requirement must be no greater than 7 dB above the longitudinal voltage requirement at frequencies above 50 kHz.

In order not to cause interference into data services, the signal levels given in Figs. 11, 12, and 13 were expressed as requirements in terms of root-mean-square (rms) voltages averaged over 100 ms. The voltage requirement has been chosen (as opposed to power) as the more appropriate measure because cable crosstalk is, by definition, a voltage phenomenon. The 100-ms averaging interval corresponds approximately to the ability of the human ear to respond to noise.

V. CONCLUSION

The metallic and longitudinal signal level requirements developed in this paper are shown graphically in Figs. 11, 12, and 13. These

requirements are given in the appendix as they were proposed on May 10, 1977 by AT&T in a petition for rulemaking to Part 68 of the FCC Rules and Regulations. These signal level requirements reflect more accurately than the current requirements the present vulnerability of carrier systems and services in the loop cable plant today.

VI. ACKNOWLEDGMENTS

The authors would like to thank their co-workers for their advice and help, particularly R. K. Even, L. M. Smith, and J. Kreutzberg.

APPENDIX

May 10, 1977 AT&T Proposed Changes in Longitudinal and Metallic Signal Power Rules of Part 68 of the FCC Rules and Regulations

A1. Longitudinal voltage in the 100-Hz to 4-kHz frequency range

The weighted root-mean-squared voltage* averaged over 100 ms that is the result of all the component longitudinal voltages in this band after weighting according to the curve in Fig. 14 shall not exceed the maximum indicated under the conditions stated in Section A3. The weighting curve in Fig. 14 has an absolute gain of unity at 4 kHz.

Frequency Range	Max rms Voltage	Longitudinal Terminating Impedance
100 Hz to 4 kHz	−30 dBV	500 ohms

A2. Voltage in 4-kHz to 1-MHz frequency range

The root-mean-squared voltage as averaged over 100 milliseconds at the telephone connections of registered terminal equipment and registered protective circuitry, in all of the possible 8-kHz bands within the indicated frequency range and under the conditions specified in Section A3 shall not exceed the maximum indicated below.

(*i*) Metallic Voltage

Frequency of 8-kHz Band	Maximum Voltage in All 8-kHz Bands	Metallic Terminating Impedance
4 kHz to 12 kHz	$-(6.4 + 12.6 \log f)$ dBV	300 ohms
12 kHz to 90 kHz	$(23-40 \log f)$ dBV	135 ohms
90 kHz to 1 MHz	−55 dBV	135 ohms

where

f = center frequency in kilohertz of each of the possible 8-kHz bands beginning at 8 kHz

dBV = 20 $\log_{10}$ voltage in volts

* Average magnitudes may be used for signals that have peak to rms ratios of 20 dB and less. Root-mean-square limitations must be used instead of average values if the peak-to-rms ratio of the interfering signal exceeds this value.

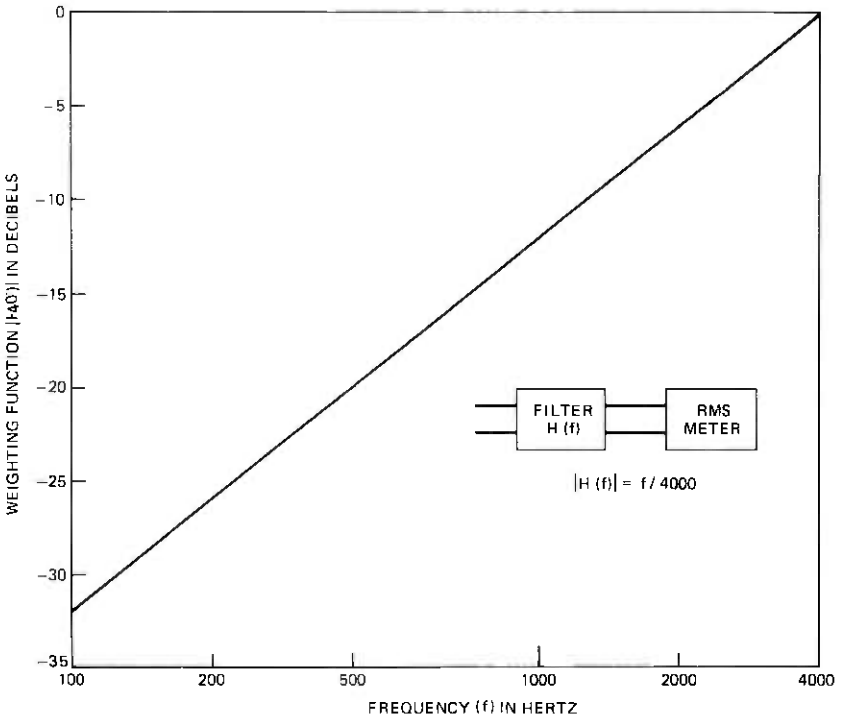

Fig. 14—Weighting function.

(*ii*) Longitudinal Voltage

Frequency of 8-kHz Band	Maximum Voltage in All 8-kHz Bands	Longitudinal Terminating Impedance
4 kHz to 12 kHz	$-(18.4 + 20 \log f)$ dBV	500 ohms
12 kHz to 60 kHz	$(3-40 \log f)$ dBV	90 ohms
60 kHz to 90 kHz	−68 dBV	90 ohms
90 kHz to 1 MHz	−62 dBV	90 ohms

A3. Requirements in Sections A1 and A2 apply under the following conditions:

(*i*) All registered terminal equipment and all registered protective circuitry must comply with the limitations when connected to a termination equivalent to the circuit depicted in Fig. 15 and when placed in all operating states of the equipment except during network control signaling.

(*ii*) All registered terminal equipment and all registered protective circuitry must comply with the limitations in off-hook states over the range of loop currents that would flow with the equipment connected to a loop simulator circuit.

(*iii*) Registered terminal equipment and registered protective circuitry with provision for through transmission from other

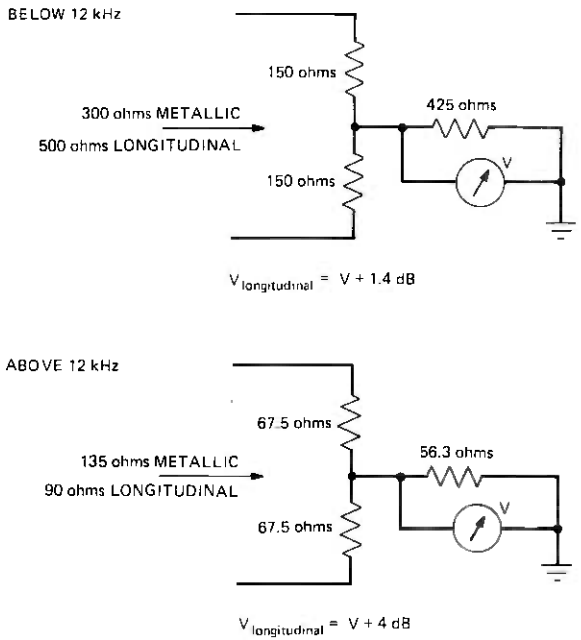

Fig. 15—Measurement terminations.

equipments shall comply with the limitations, with a 1000-Hz tone applied from a 600-ohm source (or, if appropriate, a source which reflects a 600-ohm impedance across tip and ring) at the maximum level that would be applied during normal operation. Registered protective circuitry for data shall also comply with the tone level 10 dB higher than that expected during normal operation.

(*iv*) Voice terminal equipment containing electroacoustic transducers for live voice input, including recording services, shall comply with the limitations with a 1000-Hz acoustic signal applied to the electro-acoustic transducers that results in a power delivered into the 600-ohm load impedance of −13 dB with respect to one milliwatt.

REFERENCES

1. R. K. Even, J. Kreutzberg, G. Miller, and L. M. Smith, "Spectrum Management in the Loop Plant," The International Symposium on Subscriber Loops and Services, March 20–24, 1978.
2. FCC Memorandum and Opinion Order in Docket 19528, released March 15, 1976, Section 68.308.
3. Petition for Rulemaking-Proposal for Revision to Part 68 of Commission's Rules and Regulations Pertaining to Signal Power Levels, May 10, 1977.
4. G. A. Campbell, "Dr. G. A. Campbell's Memoranda of 1907 and 1912," B.S.T.J., *14* (October 1935), pp. 558–572.
5. N. A. Strakhov, "Crosstalk on Multipair Cable—Theoretical Aspects," 1973 Nat. Telecommun. Conf., *1*, November 26–28, 1973.

6. G. S. Eager, L. Jachimowicz, I. Kolodny, and D. E. Robinson, "Transmission Properties of Polyethylene-insulated Telephone Cables at Voice and Carrier Frequencies," Trans. AIEE, Part-1, *78* (November 1959), pp. 618–639.
7. T. C. Henneberger and M. D. Fagen, "Comparative Transmission Characteristics of Polyethylene Insulated and Paper Insulated Communication Cables," Trans. AIEE, Part-1, *81* (March 1962), pp. 27–33.
8. L. Jachimowiz, J. A. Olszewski, and J. Kolodny, "Transmission Properties of Filled Thermoplastic Insulated and Jacketed Telephone Cables at Voice and Carrier Frequencies," IEEE Trans. Commun. Tech., *COM-21* (March 1973), pp. 203–209.
9. D. A. Lewinski, "A New Objective for Message Circuit Noise," B.S.T.J., *43,* No. 2 (March 1964), pp. 719–740.
10. FCC Rules and Regulations, Vol. III, January 1964, Part-73, Subpart A—Standard Broadcast Stations, Par. 73.4 (4), Subpart B—FM Broadcast Stations, Par. 73.254(4), Subpart E—TV Broadcast Stations, Par. 73.686(5).
11. Rural Electrification Administration, Specification for Station Carrier Equipment, PE-62, March 1969.
12. R. C. Boyd and F. J. Herr, "The N2 Carrier Terminal Objectives and Analysis," B.S.T.J., *44,* No. 5 (May–June 1965), pp. 731–759.
13. F. T. Andrews, Jr. and R. W. Hatch, "National Telephone Network Transmission Planning in the American Telephone and Telegraph Company," IEEE Trans. Commun. Tech., *COM-19* (June 1971), pp. 302–314.

THE BELL SYSTEM TECHNICAL JOURNAL
Vol. 58, No. 4, April 1979
Printed in U.S.A.

A Digital Simulation of the Telephone System

By C. E. SCHMIDT, L. R. RABINER, and D. A. BERKLEY

(Manuscript received March 20, 1978)

An increasing number of practical systems for speech communications have been proposed in the past few years. Such systems often must operate over both wideband channels and standard telephone connections. Thus, it is useful to be able to simulate the telephone channel as well as the other speech processing parts of the given system. This paper describes a digital network which provides a simple, controlled simulation of the properties of both the standard carbon microphone and the telephone transmission system. The simulation consists of a combination of nonlinear distortion, noise addition, and bandpass filtering. Both wideband and telephone signals were recorded simultaneously using a 2-channel A/D converter. The wideband signal was processed by the simulation system, whereas the telephone signal provided a reference signal for purposes of comparison. The parameters of the simulation were manually adjusted to provide optimum matches to several telephone links. The telephone simulation was then subjectively evaluated in two listening experiments. In both experiments, utterances from the simulations were paired with the corresponding telephone recording. In the first experiment, a group of listeners was asked to select the actual telephone recording from each pair of utterances. In the second experiment, a new group of listeners was asked to rank the similarity of the two utterances on a 1-to -10 scale. Results of the evaluations indicated that, for some sets of simulation parameters, the network provided a fairly good psychophysical simulation of a variety of telephone channels.

I. INTRODUCTION

In recent years, an increasing number of systems for speech communications have been proposed which must operate over both wideband channels and standard telephone connections.[1-5] Included among such systems are waveform coders, speech analysis-synthesis systems, and systems for man-machine communication by voice—e.g., speech

recognizers or speaker verifiers. To investigate the capabilities of such systems in a controlled manner, it is useful to be able to simulate the effects of the telephone channel on the speech signal as well as the other signal processing parts of the system. The conventional approach to telephone simulations of speech processing systems is to repeatedly dial up a new line for each input utterance to obtain a reasonable distribution of lines. However, not only is this method clumsy, but it does not guarantee good statistical sampling of telephone lines. As an alternative, it would be desirable to substitute a controlled simulation of a telephone channel which attempted to model the system from the handset to the earphone—that is, the telephone carbon button, the telephone line, the switching, and the receiver.

Figure 1 is a set of block diagrams that illustrate the various types of simulations one can consider using. The simplest simulation, in Fig. 1a, is an "end-to-end" simulation in which the input signal (to either the telephone line or the black box simulation) is obtained directly from a talker, and the simulation output is sent directly to a listener. In such cases, the "black box" simulation need not in any way physically model the actual telephone system. It is sufficient for the black box to model only the psychophysically significant effects of the telephone system.

The type of simulation in Fig. 1b is a more demanding one in that the end result of the simulation is subjected to subsequent processing by a physical system prior to evaluation by either a listener or some form of measurement system (e.g., a computer). In order for the black box to be a good simulation of the telephone system, it must be a physical simulation of the relevant processing which actually occurs in the telephone system. For some, if not most cases, one would not expect an end-to-end simulation (such as that shown in Fig. 1a) to perform well in systems which require physical simulations.

The situations shown in Figs. 1c and 1d represent modified versions of the cases shown in Figs. 1a and 1b. For these cases, the input signal is preprocessed prior to the telephone line. *A priori*, one would expect that physical simulations of the telephone line would perform well in both situations (i.e., the systems of Figs. 1c and 1d). However, the end-to-end type of simulation would probably be most successful (because of the placement of nonlinear elements in the system) in the system of Fig. 1c (depending on the details of the preprocessing), whereas in the system of Fig. 1d it would often not be useful.

In this paper, we are primarily concerned with end-to-end simulations of the telephone system. We have chosen this alternative for two main reasons. The first, and perhaps most important, reason is the difficulty in obtaining a good physical characterization of the processing in the actual telephone system from the handset to the receiver. A previous attempt at a physical simulation of only the telephone trans-

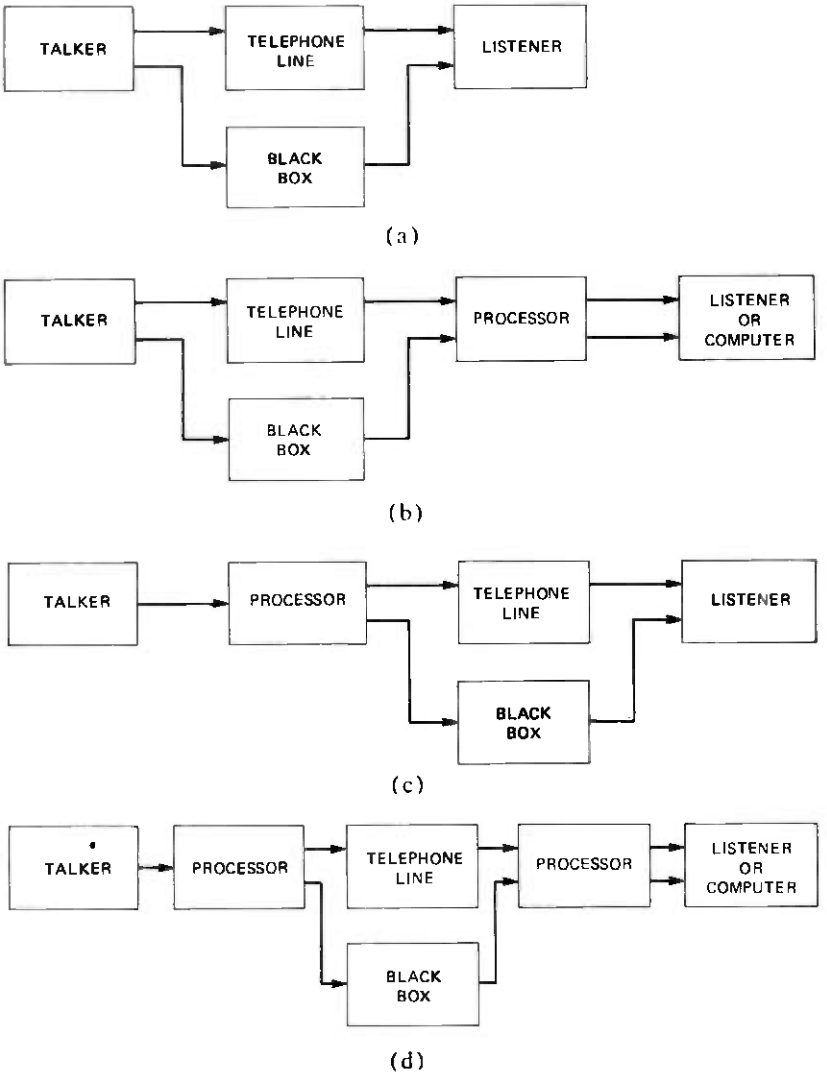

Fig. 1—Block diagrams of typical arrangements of telephone system simulations.

mission system was made at Lincoln Laboratories, based on a set of measurements of continental U.S. and European voice and data grade lines.[6,7] The simulation, run on the real-time signal processor at Lincoln Laboratories, modelled some transmission characteristics of the lines. The effects that were included in this simulation were linear filtering, quadrature distortion (phase jitter), carrier frequency offset, and various types of noise. Effects that occur in satellite transmissions, as well as echo suppression, cross talk, etc. were not included in the Lincoln simulation.[8] Although this simulation was quite sophisticated, the

model is overly complex for many applications. For example, for local lines the amount of quadrature distortion and carrier frequency offset is negligible and hence need not be considered in the simulation. In addition, in the Lincoln simulation, no model was provided for the telephone handset itself—i.e., the carbon microphone. Although the characteristics of the carbon microphone are highly nonlinear[9] and not very well understood, a considerable measure of the "telephone" quality of speech is imparted by the carbon microphone. Thus, it is necessary for any end-to-end *or* physical simulation of the telephone system for use with speech input to model both the telephone carbon microphone and the transmission system.

A second reason for our interest in end-to-end simulations is that a number of simplifications can be made in the model, since we need only be concerned with aspects of the telephone system that are psychophysically significant. Hence, we can rely on both our knowledge of auditory and speech perception and past experience with systems that process telephone quality speech to aid in the selection of components of the model. In addition, we are free to investigate simpler models for an end-to-end simulation than could be justified for a physical simulation.

The purpose of this paper is to describe a simple digital network that provides an end-to-end simulation of the combined standard carbon microphone and the telephone transmission system. The network, implemented via digital simulation, has the flexibility of allowing the user to vary parameters of the model, thereby simulating a wide variety of telephone lines. By systematically varying these parameters, we have been able to match the characteristics of several different links and have obtained signals which perceptually have most of the "telephone quality" attributes.

The organization of this paper is as follows. In Section II, we describe the telephone model and the resulting simulation. In Section III, we describe a series of two experiments conducted to determine the effectiveness of the simulation in perceptually matching selected telephone links. In Section IV, we present the results of the experiments and discuss their significance.

II. SIMULATION OF THE TELEPHONE LINE

Figure 2 is a block diagram of how the telephone line simulation is organized. The overall line is modelled as a cascade of a model for the telephone handset (i.e., the carbon microphone) and a model for the telephone transmission channel. Ideally, the Lincoln Laboratories simulation would provide a sophisticated physical model for the telephone transmission. However, in line with our stated objectives, we chose to implement a considerably simpler model.

A more detailed block diagram of the telephone model and the system used to evaluate it is given in Fig. 3. The input to the model is assumed to be a speech signal, bandpass-filtered from 100 to 3000 Hz and sampled at a 10-kHz rate. The transmitter model consists of an interpolator, a nonlinearity (center clipper), and a decimator. The interpolator changes the sampling rate to 50 kHz, keeping the bandwidth the same as at the low rate through the use of a high-order, linear-phase, FIR digital filter.[10] The center clipper has a center clipping (CC) level which is a percentage of the peak signal level for each utterance. The decimator first filters the nonlinearly distorted signal to the original bandwidth and then reduces the sampling rate back to 10 kHz. The 5-to-1 change in sampling rate was sufficient to guarantee that the high-frequency, nonlinear distortion products of the center clipper would not affect the speech baseband.

If we call the input signal to the interpolator $x(n)$ and the output signal from the interpolator $y(n)$, then

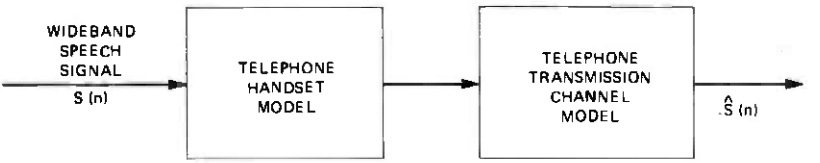

Fig. 2—Block diagram of telephone system model.

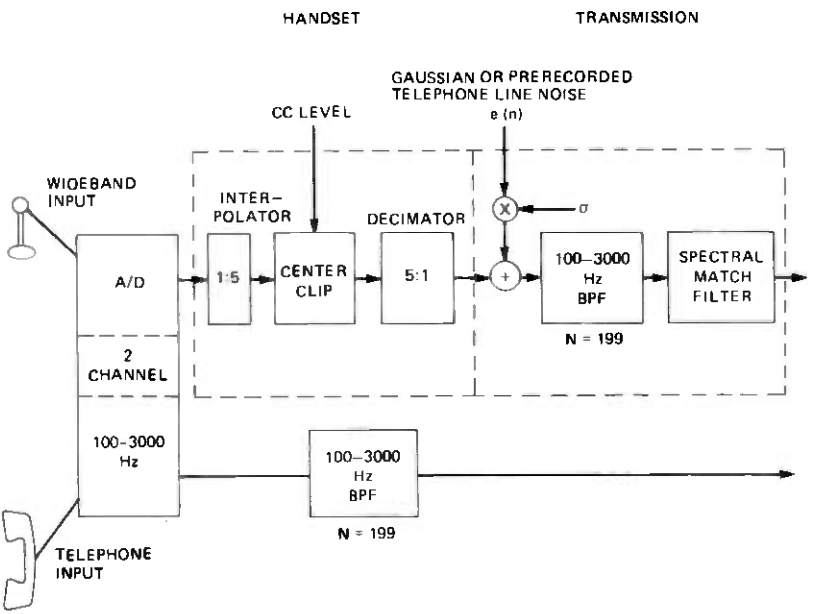

Fig. 3—Block diagram of experimental system used to test the simulation.

$$y(n) = v(n) * h(n) = \sum_{m=0}^{L-1} h(m)v(n-m),$$

where

$$\begin{aligned} v(n) &= x(n/5) \qquad n = 0, \pm 5, \pm 10, \cdots \\ &= 0 \qquad\quad \text{otherwise,} \end{aligned}$$

and $h(n)$ is an L-point FIR linear phase lowpass filter with bandwidth 3 kHz. Thus $y(n)$ and $x(n)$ have the same frequency spectrum in the band $0 \leq f \leq 3$ kHz.

The center clipper has an input-output characteristic of the form

$$\begin{aligned} \hat{y}(n) &= y(n) \quad \text{if} \quad |y(n)| > C_n \\ &= 0 \qquad\quad \text{otherwise,} \end{aligned}$$

where

$$C_n = k \cdot \max_n [\,|x(n)|\,]$$

and n ranged over all samples in the utterance. (In the experiment, k was a variable that was investigated.)

To eliminate the high-frequency distortion products in $\hat{y}(n)$, due to the nonlinearity (i.e., the center clipper), the signal $\hat{y}(n)$ was again filtered by the lowpass filter $h(n)$ to give the output $z(n)$, computed as

$$z(n) = \sum_{m=0}^{L-1} h(m)\hat{y}(n-m).$$

The decimated signal, $\hat{x}(n)$, was obtained by retaining every fifth sample of $z(n)$, i.e.,

$$\hat{x}(n) = z(5n).$$

Efficient signal processing techniques were used to implement both the interpolator and the decimator.[10]

The telephone transmission model consisted simply of three components: an additive wideband noise whose amplitude was variable; a fixed-FIR, linear-phase, bandpass filter; and a variable digital filter which provided a spectral shaping that could match any desired shape. The noise used in the simulation was one of two types—either a wideband Gaussian noise or a prerecorded telephone line noise. The spectral matching filter was implemented as a cascade of two digital filters. The first filter was a 25-point, FIR, linear-phase filter which provided a gross spectral match to the signal spectrum of an average telephone line—i.e., it provided an approximation to the general non-flat frequency weighting in the system. The second filter was a 255-point, FIR, minimum-phase filter which provided a detailed match of the simulation spectrum to the spectrum of a specified telephone line.

The lower path of the system shown in Fig. 3 represents a direct recording of a telephone signal at the receiver of the called party—i.e., after the speech signal has been transduced by the carbon microphone of the transmitter, sent over a link to a central office, and returned to a different telephone at the same location where the call was initiated. A 2-channel, analog-to-digital converter was used to simultaneously digitize the original speech signal (from a high-quality microphone) and the resulting telephone speech signal. Both signals were bandpass-filtered from 100 to 3000 Hz and digitized at 10-kHz rates.

Using the model of Fig. 3, a series of investigations were made to see to what extent the signal at the output of the simulation could perceptually match the telephone signal recorded simultaneously with the original wideband signal. In the next section, we describe these investigations.

III. EXPERIMENTAL INVESTIGATIONS

To evaluate how well the system shown in Fig. 3 could model the perceptual characteristics of various telephone lines, a series of recordings was made under the following conditions:

(*i*) Two speakers—one male, one female.
(*ii*) Two sentences.
(*iii*) Three telephone links.
  (*a*) Single PBX loop within Bell Laboratories (Murray Hill to Murray Hill). This is a standard Centrex line.
  (*b*) Double PBX loop (Murray Hill to Whippany to Murray Hill).
  (*c*) Double PBX loop (Murray Hill to Holmdel to Murray Hill).

The double PBX should be typical of local exchange carrier transmission—i.e., the transmission path typically contains channel bank filters (analog or digital) and some form of companding.[8]

To illustrate a typical recording, Fig. 4 is a plot of the long-term average spectrum for one of the wideband sentences. Included in this plot are both the long-time average spectrum (computed using a 1024-point FFT analysis), and a cepstrally smoothed representation of the long-time average spectrum.[11] The speech spectrum is seen to fall by about 40 dB at 5 kHz.

Similarly, Fig. 5 is a plot of the long-time average spectrum (and its cepstrally smoothed representation) for the telephone recording which corresponds to the wideband recording of Fig. 4. The most significant difference in the spectra of the respective signals is the reduced bandwidth of the telephone recording. However, careful comparisons between spectra shows significant differences in the region from 100 to 3000 Hz. The spectral matching filter was intended to model these differences.

Preliminary informal experimentation with the model of Fig. 3 for the above set of recording, indicated that clipping levels below 1

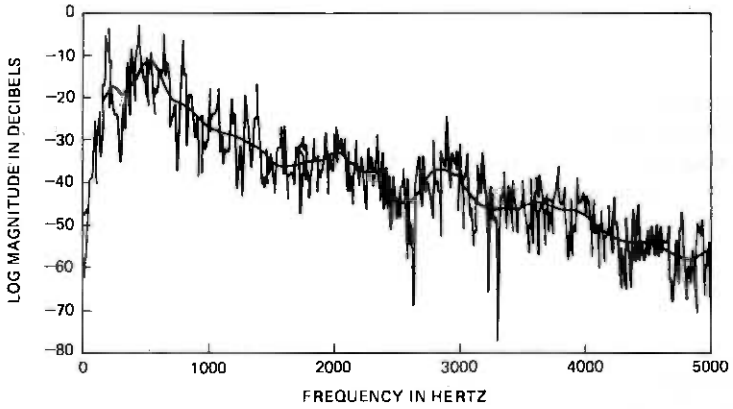

Fig. 4—Long-time average spectrum (irregular curve) and cepstrally smoothed version (smooth curve) for a typical wideband speech signal.

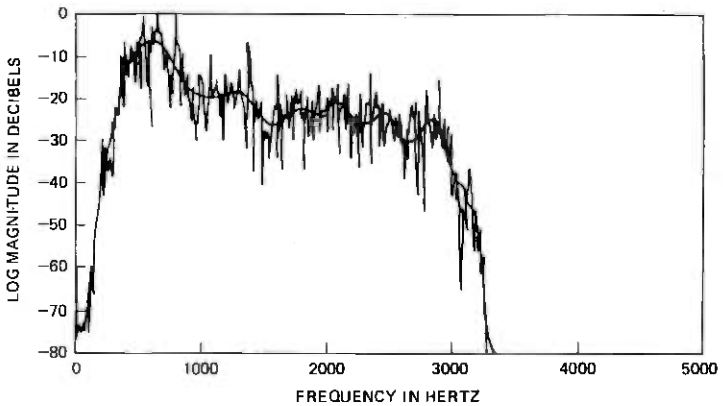

Fig. 5—Long-time average spectrum (irregular curve) and cepstrally smoothed version (smooth curve) for a typical telephone speech signal.

percent had no significant effect on the speech, whereas those above 2 percent produced excessive distortion in the speech. Thus, a choice of 3 clipping levels was made, namely 1 percent, 1½, and 2 percent of the peak signal level of the signal throughout the utterance.

The range of noise gains (σ in Fig. 3) was also determined by informal listening. For the Gaussian case, it was found that noise levels corresponding to signal-to-noise ratios in the range from 30 to 40 dB were optimal. As such, two noise gains were chosen corresponding to approximately 30- and 40-dB signal-to-noise ratios. For the prerecorded telephone line noise, the original signal was obtained at the level of a normal single PBX loop by recording directly off the telephone line with no speech present. Two gain levels of $\sigma = 1$ and $\sigma = 2$ were used in the experiment.

Once the center clipping and noise level ranges were determined, the remaining factor in the simulation was the design of the spectral match filter. To formulate an idea of the requirements on the spectral match filter, plots of the smoothed, long-time spectral differences between the digitally filtered telephone signal and the signal at the output of the bandpass filter in the model were obtained. Figure 6 shows one of these plots. In the region from 100 to 3000 Hz, the real telephone signal spectrum was from 0 to 15 dB above the simulation spectrum. The variation in this spectral difference among speakers, sentences, and telephone links was not very large. Thus, a rough approximation to this spectral difference was used to design a 25-point, FIR, linear-phase digital filter which provided a gross spectral match (to within ±5 dB) of the simulation spectrum to the telephone spectrum in the range from 100 to 3000 Hz. Figure 7 shows the frequency response of a typical gross spectral match filter. The filter provides a fairly good match near the peaks of the difference curve but is significantly worse near the valleys.

Although informal listening comparisons between the simulation output (after the gross spectral match filter) and the telephone input

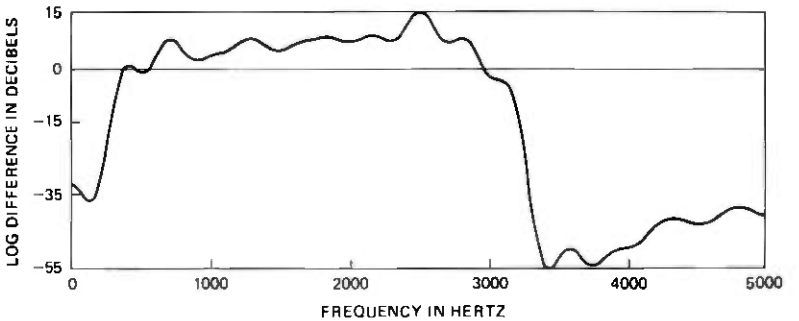

Fig. 6—Long-time spectral difference between a telephone signal and the simulation output after simple bandpass filtering.

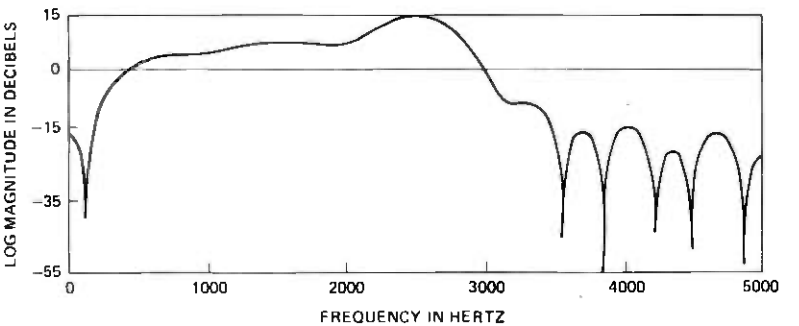

Fig. 7—Frequency response of a typical gross spectral match filter.

indicated a strong similarity between the simulations and the actual telephone speech, there were equally significant differences in both temporal and spectral detail. To assess to what degree the spectral differences were significant, a second spectral match filter was implemented using a high-order (255-point, FIR minimum phase filter) match to the difference spectrum. Figure 8 shows the frequency response to a typical fine spectral match filter, and Fig. 9 shows the resulting spectral difference. As seen in this figure, spectral deviations of about ¼ dB are obtained in the range from 100 to 3000 Hz.

An alternative measure of the spectral similarity between two utterances is the LPC distance or the log likelihood ratio as proposed by Itakura.[12] This measure shows, on a *frame-by-frame* basis, the log spectral difference between two utterances. Figure 10 shows a pair of plots of the LPC distance between the original wideband recording and the original telephone input. The LPC distance is not exactly symmetrical. Thus, the plots show both distances associated with the pair of

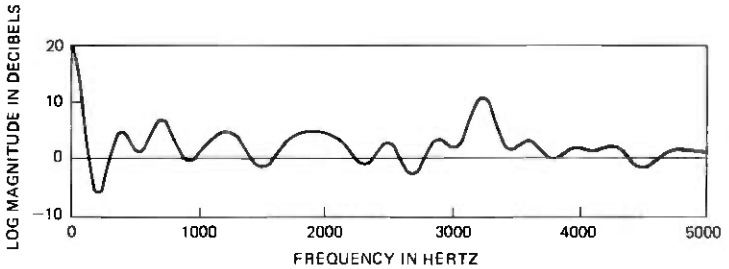

Fig. 8—Frequency response of a typical fine spectral match filter.

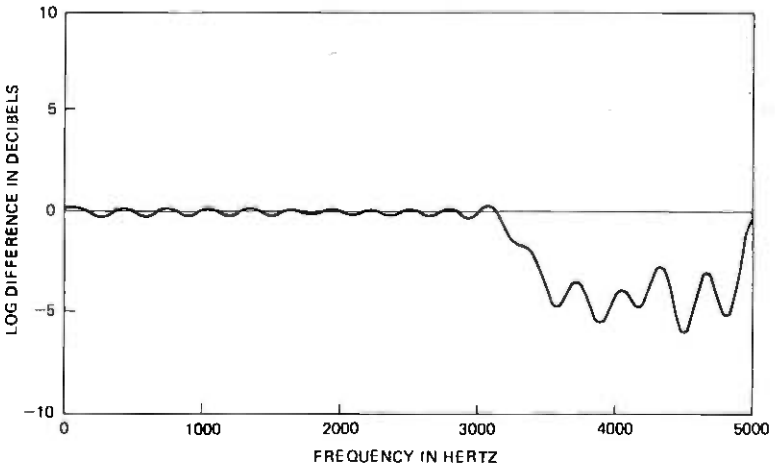

Fig. 9—Long-time spectral difference between a telephone signal and the final simulation output.

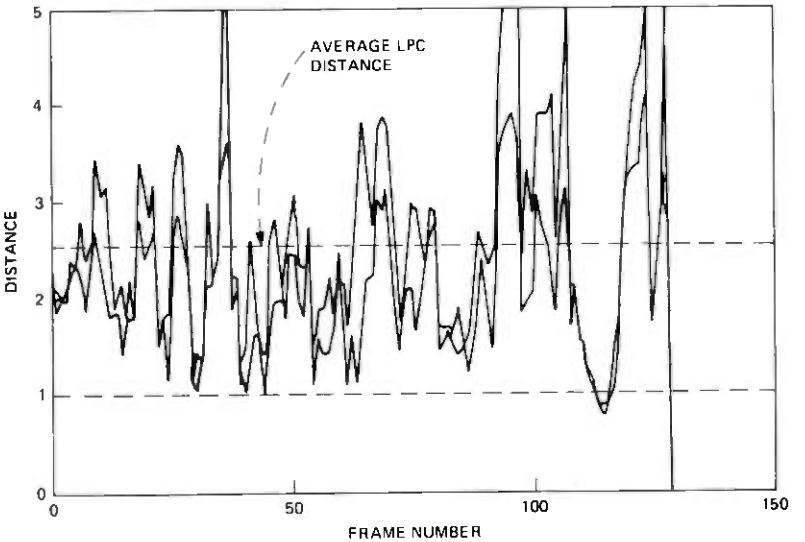

Fig. 10—Plots of frame-by-frame LPC distances between an original wideband signal and the corresponding telephone signal.

utterances. The dotted line at the bottom (at a distance of about 1) is a threshold for which the spectral differences between frames is perceptually significant.[13] From Fig. 10, it is seen that, for almost every frame in the utterance, the distance was significant. The average LPC distance for this example was about 2.6.

In contrast, Fig. 11 shows a pair of plots of the LPC distance between the original telephone input and the output after the gross spectral match filter (Fig. 11a) and after the fine spectral match filter (Fig. 11b). The average LPC distance is about 0.66 for the plots of Fig. 11a and 0.57 for the plots of Fig. 11b. Both these distances are well below the perceptually significant threshold. However, it is still seen in both Figs. 11a and 11b that for a number of frames, the LPC distance exceeds the perceptual threshold. These differences are due to both temporal and short-time spectral differences between the utterances which the simulation is incapable of handling.

Based on the informal observations and the objective measurements described above, further evaluation of the simulation was achieved through two subjective experiments. The first was an A-B comparison between the output of the model and the actual telephone signal to see how well listeners could identify the actual telephone signal. The second experiment was a similarity ranking test between the simulation output and the actual telephone signal.

Table I provides a summary of the experimental factors included in the tests. We have already discussed the first six factors in the test; namely, speakers, sentences, transmission links, center clipping levels,

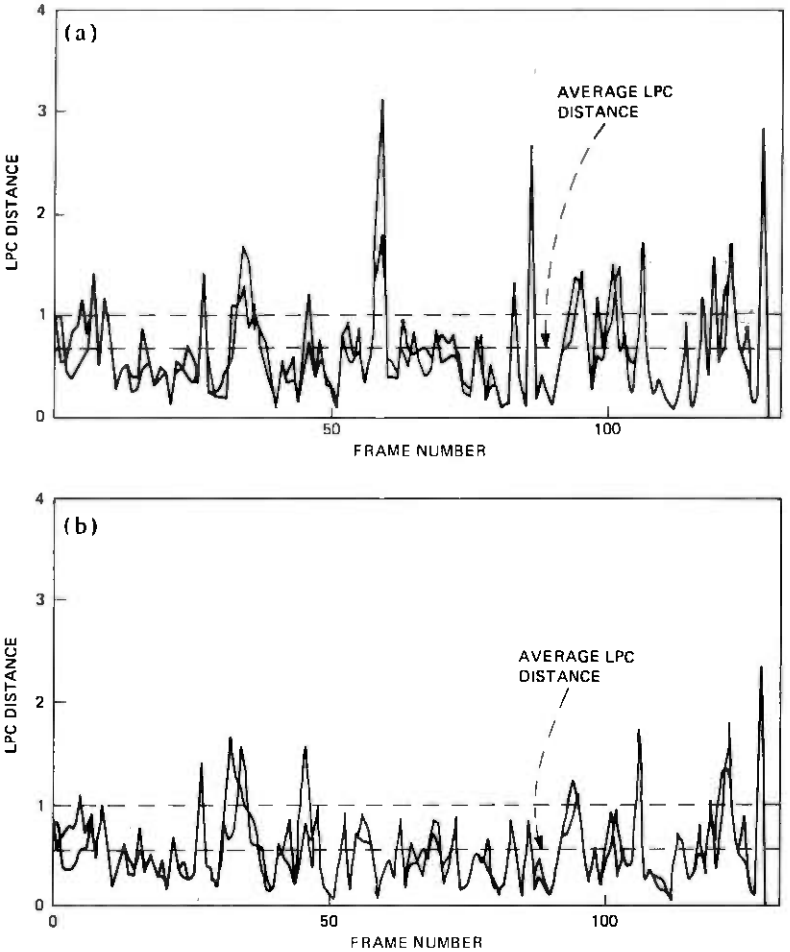

Fig. 11—Plots of frame-by-frame LPC distances between the simulation output and the corresponding telephone signal; (a) after the gross spectral match filter; (b) after the fine spectral match filter.

Table I—Summary of experimental factors in the listening experiment

Experimental Factors
1. Speakers (2-1 male, 1 female).
2. Sentences (2).
3. Transmission links (MH-MH, WH-MH, HO-MH).
4. Center clipping levels (3).
5. Types of noise (2).
6. Noise levels (2).
7. Levels of filtering (3).
8. Listeners (8).
Experiments
1. A-B comparison for identifying actual telephone line.
2. Similarity ranking between simulation and actual telephone line (scale 1-10).

types of noise, and noise levels. The seventh factor was the three levels of filtering; namely, a flat bandpass filter alone, a combination of a flat bandpass filter and the gross spectral match filter, and the triple combination of the flat bandpass filter, the gross spectral match filter, and the fine spectral match filter. The last factor was listeners (eight were used). In both experiments, the simulation utterances were paired with the corresponding telephone recordings in a random ordering. For the A-B test, a simple choice was required of the listeners as to which of the pair was the actual telephone signal. In the ranking tests, the listeners were asked to rank the similarity of the pair on a scale of 1 to 10 where 1 was most similar and 10 was not at all similar. Results of these experiments are given in the next section.

IV. RESULTS

For the telephone identification experiment (the A-B comparison test), a score of 1 was given if the simulation was identified as the telephone, and a score of 0 was given if the listener correctly chose the actual telephone recording. Data were collected over a 1-week period. An analysis of variance of the results indicated that the only significant factors in the experiment were listeners and types of filtering. The fact that the center clipping level was not a significant experimental factor was not surprising since the *range* of this parameter had been carefully chosen to be reasonable for typical telephone lines. Although the noise level factor was not significant, the type of noise was treated as an independent factor since the data for each type of noise were obtained in separate runs, and this factor is an interesting one from the simulation point of view. We shall see that there were surprisingly small differences in this factor.

It was not surprising that the factors of speakers and sentences were not significant; however, it was somewhat unexpected that the transmission link factor was not significant. This result implies that, to a first order, a linear system provides a good (or a uniformly bad, which seems very unlikely) approximation to differences in transmission.

The average identification scores, as a function of level of filtering, were computed from the raw data and are shown in Fig. 12a. Figure 12b shows a more detailed set of results in which the listener scores are individually plotted for the Gaussian noise case. For these plots, a mean score of 0.5 indicates that the listener could not identify the actual telephone recording, and scores close to 0 indicate the listener could always identify the actual telephone line. The brackets in Fig. 12a indicate the range for one standard deviation. The extreme variability in mean scores across listeners can readily be seen in Fig. 12b. However, it can be seen that, for all but two of the listeners, for both noise types, the mean identification scores got larger (headed towards chance identification) as the complexity of filtering increased. Fur-

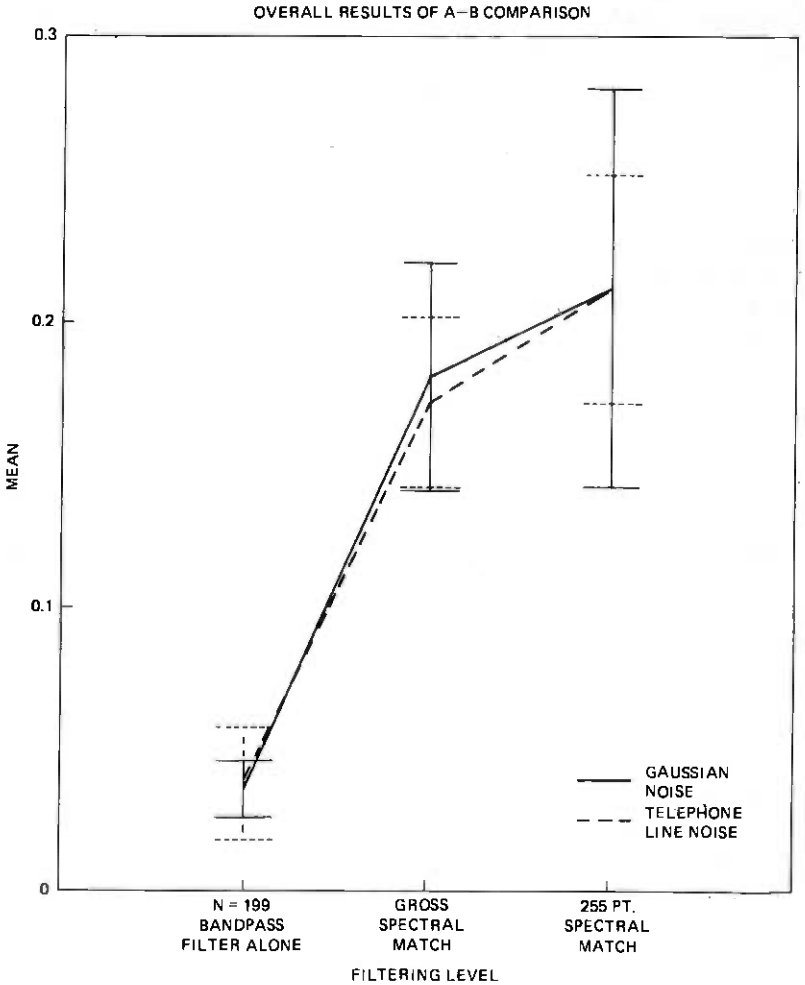

Fig. 12a—Mean identification scores for experiment 1 as a function of filtering level averaged across all conditions.

thermore, for the fine spectral match, the mean identification score was quite close to the score for the gross spectral match filter, thereby indicating the small improvement obtained with the final filter. The standard deviation of the results using the telephone noise was somewhat smaller than for the comparable Gaussian noise. The mean identification score of 0.22 indicates that, even for the best cases, listeners could distinguish between an actual telephone recording and the simulation output approximately 50 percent of the time in an A/B test. However, such a test is a very severe one as any flaw in the simulation will immediately cue the listener as to which of the pair of

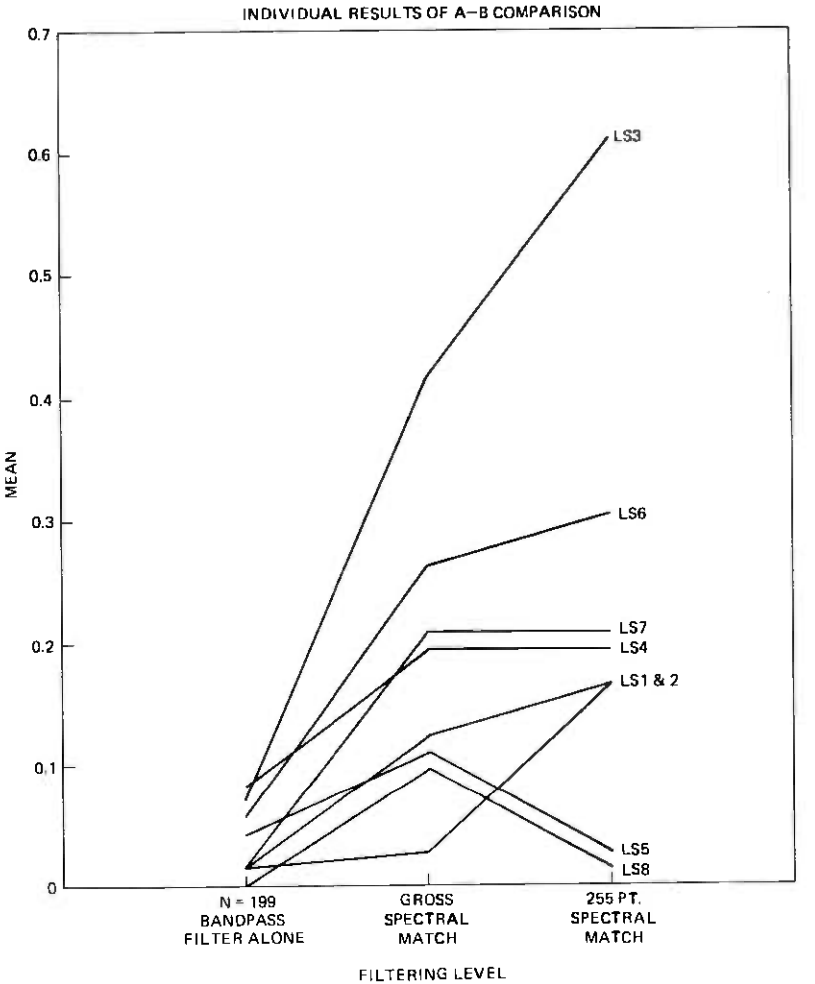

Fig. 12b—Mean identification scores for experiment 1 as a function of listener using Gaussian noise.

utterances is the simulation. Thus, the average score of 0.22 is actually an encouraging one in such a test.

For the similarity ranking experiment, a score of 1 indicated high similarity between sentences, whereas a score of 10 indicated large differences between sentences. For this experiment, a new group of 8 listeners was used and test data were again recorded over a 1-week period. An analysis of variance of the results again showed that the only significant experimental factors were listeners and filtering complexity. Again, however, results are shown for both types of noise. Figure 13 shows a plot of the overall mean ranking score as a function

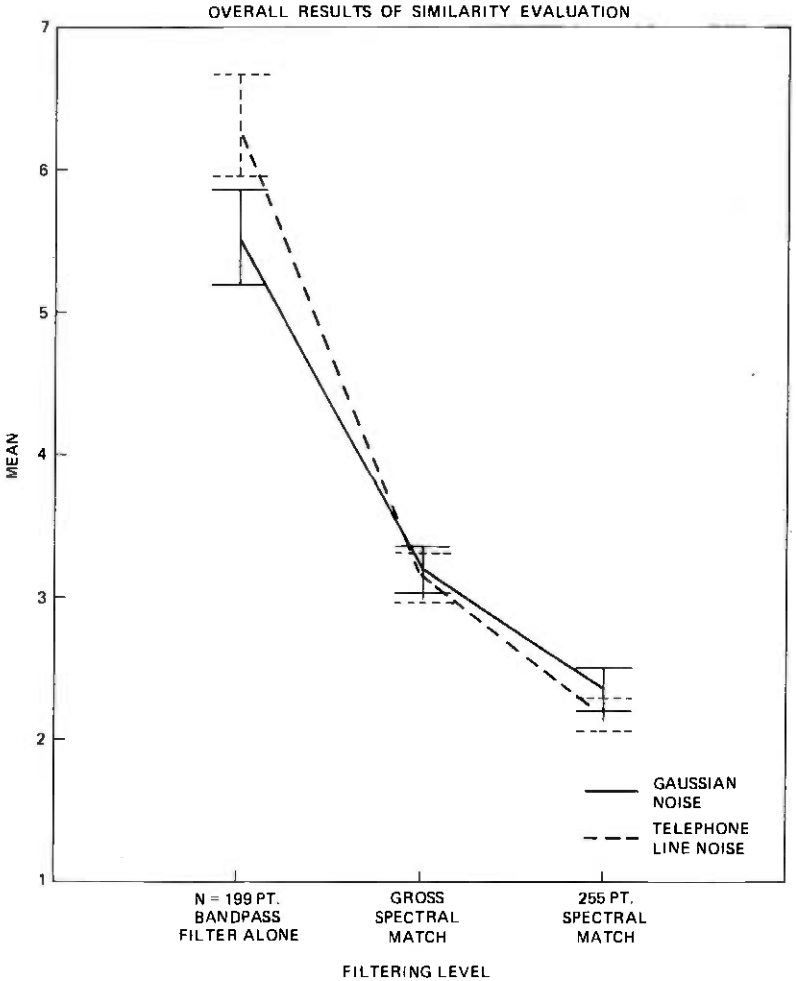

Fig. 13—Mean identification scores for experiment 2 as a function of filtering level averaged across all conditions.

of the level of filtering. It can be seen that the average ranking score was about 3.2 for the gross spectral match filter, whereas it was 2.3 for the fine spectral match filter, thereby indicating a very strong similarity between the simulation output and a real telephone recording. It is also seen that the ranking scores are very similar for both the Gaussian and prerecorded telephone noises, again showing this is not a critical feature of the simulation. The results presented in this figure confirm that the simulation produced an output which listeners considered highly similar to actual telephone recordings.

V. SUMMARY

The results of the experimental evaluations indicated that a fairly simple simulation of a telephone channel can provide a good approxi-

mation (in a perceptual sense) to a variety of actual telephone lines. Informal listening indicated that, to give speech the "telephone-like" quality (as opposed to matching an individual telephone line), a general spectral matching filter along with the center clipping nonlinearity was adequate. Although the best results were obtained with a combination of a gross spectral match filter and a fine spectral match filter, the results obtained with the low-order gross spectral match filter alone were quite good and undoubtedly would be adequate for a variety of applications.

The intended purpose of this simulation was to provide a digital network which would be controlled in such a way as to make it interchangeable with a real telephone line for perceptual testing and evaluating speech communications systems. The next step in evaluating the applicability of this model to other situations is to compare objective performance on a speech communication system over real telephone lines with results using the simulation. If these comparisons are favorable, then models such as the one proposed here should be useful for testing and evaluating speech processing systems without the need for extensive evaluation over actual telephone lines.

In summary, we have proposed a simple digital network which provides an end-to-end simulation model of a telephone line from the handset to the receiver. Subjective evaluations indicate that a good match to a variety of telephone lines can be obtained.

REFERENCES

1. J. L. Flanagan, "Computers that Talk and Listen: Man-Machine Communication by Voice," Proc. IEEE, *64*, No. 4 (April 1976), pp. 405–415.
2. A. E. Rosenberg, "Automatic Speaker Verification: A Review," Proc. IEEE, *64*, No. 4 (April 1976), pp. 475–487.
3. L. R. Rabiner, "On Creating Reference Templates for Speaker Independent Recognition of Isolated Words," IEEE Trans. on Acoustics, Speech, and Signal Proc., *ASSP-26*, No. 1 (February 1978).
4. A. E. Rosenberg, "Evaluation of an Automatic Speaker-Verification System Over Telephone Lines," B.S.T.J., *55*, No. 6 (July–August 1976), pp. 723–744.
5. L. R. Rabiner, C. E. Schmidt, and B. S. Atal, "Evaluation of a Statistical Approach to Voiced-Unvoiced-Silence Analysis for Telephone-Quality Speech," B.S.T.J., *56*, No. 3 (March 1977), pp. 455–482.
6. S. Seneff, "A Real-Time Digital Telephone Simulation on the Lincoln Digital Voice Terminal," Technical Note 1975–65, M.I.T. Lincoln Laboratory, 30 December 1975.
7. U. S. Government Study of Continental U.S. Voice Grade and Data Lines, unpublished work.
8. Bell Telephone Laboratories, *Transmission Systems for Communications*, 1970.
9. R. W. Kett, "Carbon Microphones for Communication," Proceedings I.R.E.E. Australia (April 1964), pp. 250–256.
10. R. W. Schafer and L. R. Rabiner, "A Digital Signal Processing Approach to Interpolation," Proc. IEEE, *61* (June 1973), pp. 692–702.
11. A. V. Oppenheim, R. W. Schafer, and T. G. Stockham, "Nonlinear Filtering of Multiplied and Convolved Signals," Proc. IEEE, *56* (August 1968), pp. 1264–1291.
12. F. Itakura, "Minimum Prediction Residual Applied to Speech Recognition," IEEE Trans. on Acoustics, Speech, and Signal Proc., *ASSP-23*, No. 1 (February 1975), pp. 67–72.
13. M. R. Sambur and N. S. Jayant, "LPC Analysis/Synthesis From Speech Inputs Containing Quantizing Noise or Additive White Noise," IEEE Trans. on Acoustics, Speech, and Signal Proc., *ASSP-24*, No. 6 (December 1976), pp. 488–494.

THE BELL SYSTEM TECHNICAL JOURNAL
Vol. 58, No. 4, April 1979
Printed in U.S.A.

Adaptation of Ordering Techniques for Facsimile Pictures with No Single Element Runs

By A. N. NETRAVALI, F. W. MOUNTS, and K. A. WALSH

(Manuscript received September 18, 1978)

We present a simple strategy for modification of two-level facsimile pictures and adapt our earlier published ordering techniques to take advantage of the modification. Picture modification consists of eliminating all horizontal runs of "black" or "white" elements which are of length one. For pictures with high resolution (e.g., 200 dots/inch), such a modification does not excessively degrade the picture quality. The resulting entropy of the coded pictures is between 0.018 to 0.115 bits/pel for the eight CCITT *pictures, which are scanned and sampled at approximately 200 dots/inch. This amounts to an average reduction of 48 percent compared to one-dimensional run-length coding and 10 percent compared to our previously published best ordering technique.*

I. INTRODUCTION

Coding of two-tone facsimile pictures is gaining considerable importance. Many sophisticated algorithms which use the two-dimensional correlation present in the facsimile pictures have been developed. Most of these code the picture in such a way that an exact reproduction of the picture is possible at the receiver. Considerable bit-rate reduction is possible, however, by approximating the original picture by another picture which can be coded more efficiently than the original. Success of such schemes will depend upon the type of approximation used. Approximations that introduce the least visible distortion in the picture but reduce the bit rate significantly are the most desirable. Problems of picture modification and evaluation of their advantages for two-level facsimile signals have recently begun to receive some attention.[1-5]

We present a simple method of picture modification and then evaluate its advantages with respect to ordering techniques.[6] Pictures

are modified so that runs of single "white" (="0") or "black" (="1") elements along a scan line are suppressed. At high resolution of 200 dots/inch; such a modification does not degrade the picture significantly. This preprocessing allows us to modify our earlier published ordering techniques[6-8] in an advantageous way by treating even and

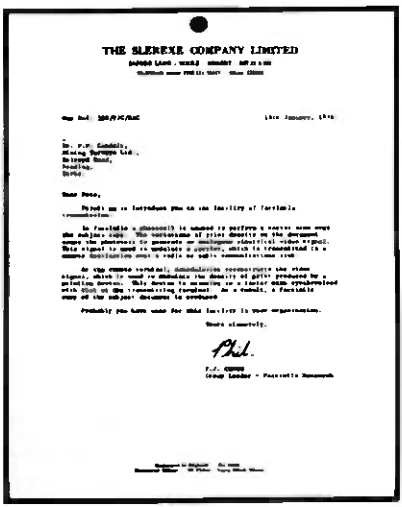

1

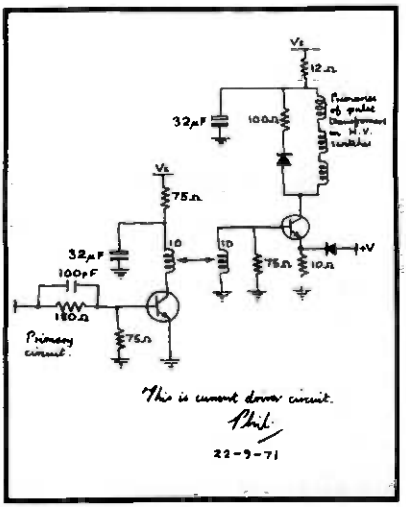

2

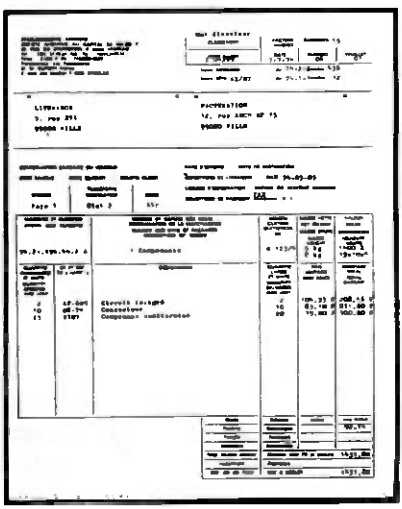

3

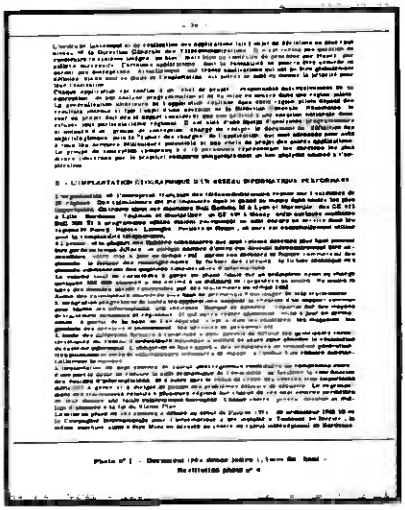

4

Fig. 1—Original eight CCITT documents. These are scanned and sampled at approximately 200 dots/inch. Each document is approximately 8½ by 11 inches and contains 2128 scan lines, each with 1728 picture elements.

odd samples along a scan line differently. The preprocessing combined with one of our ordering techniques results in entropies for the eight CCITT coded pictures between 0.018 and 0.115 bits/pel. The decrease in entropy due to picture modification is, on the average, 10 percent compared to our previously published best ordering technique.

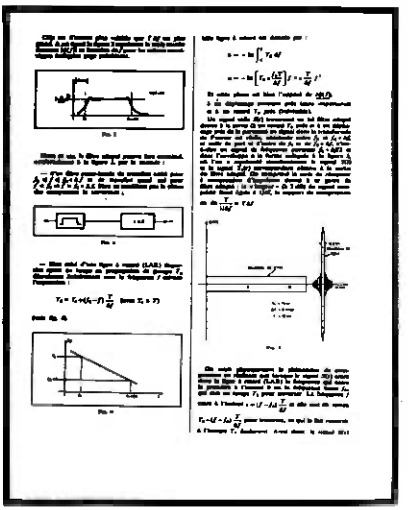

5

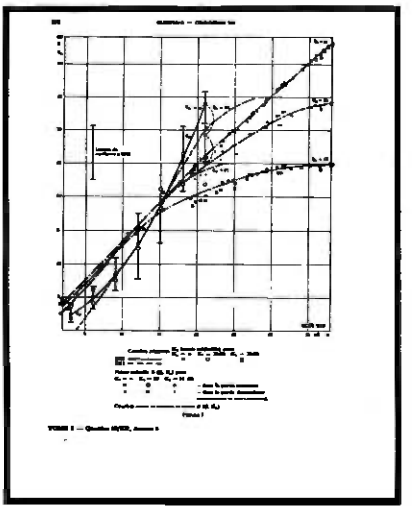

6

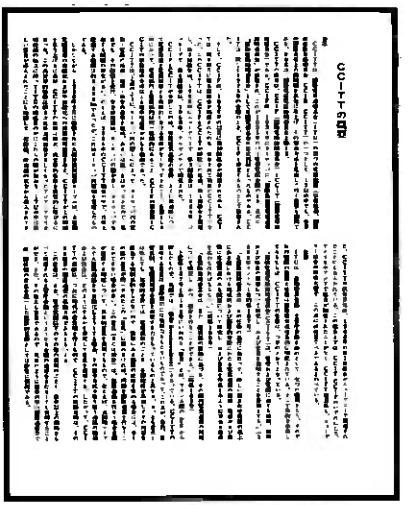

7

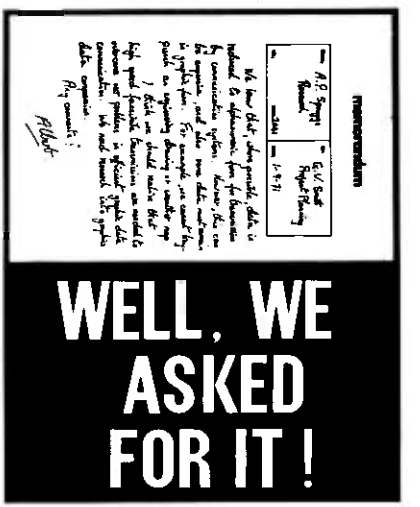

8

Fig. 1 *(continued)*

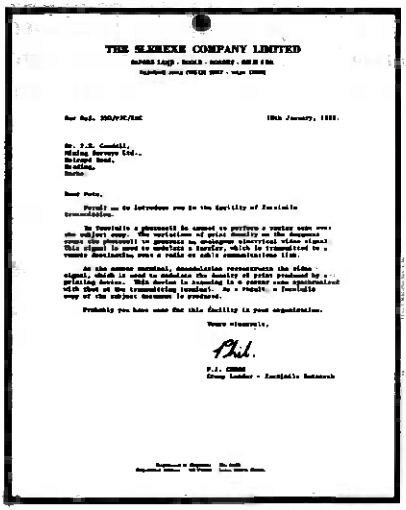

1

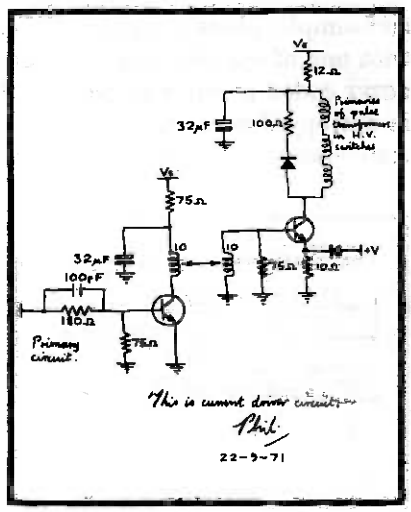

2

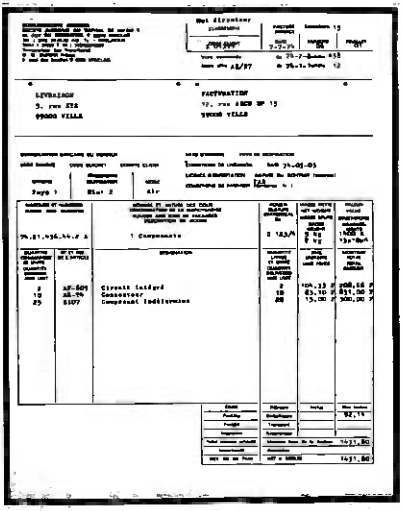

3

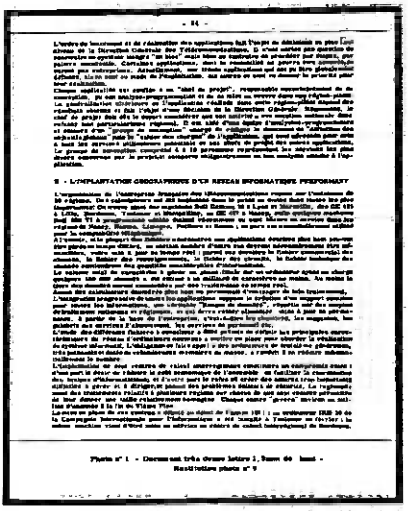

4

Fig. 2—Modified CCITT documents with suppression of single element runs.

II. ALGORITHM AND SIMULATION RESULTS

In this section we give details of the picture modification strategy, the ordering technique, and the simulation results. More details on the ordering technique can be found in Ref. 8.

As mentioned earlier, we have looked at a simple picture modification strategy. In this strategy, we eliminate all runs of single elements

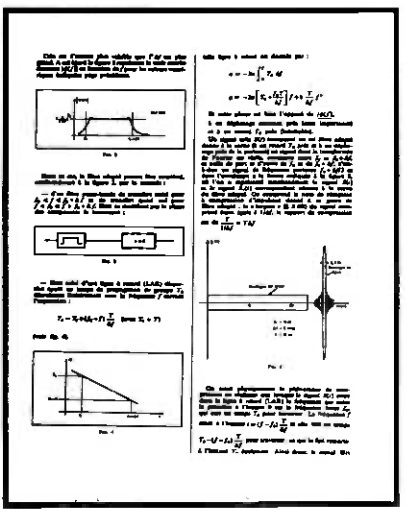

5

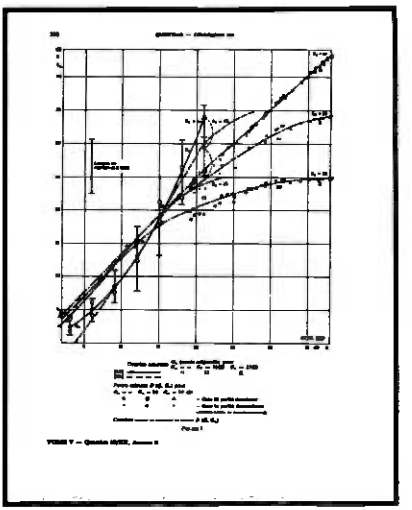

6

7

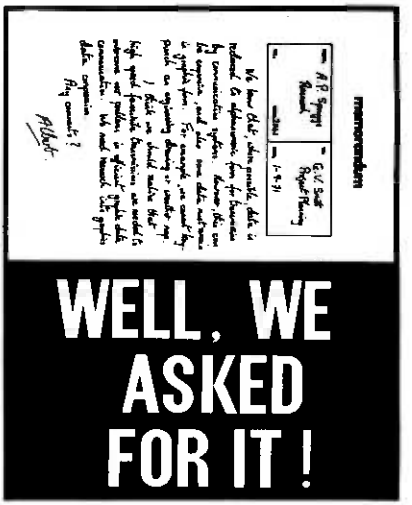

8

Fig. 2 *(continued)*

"black" or "white" along a scan line. At a resolution of 200 dots/inch, most of the single runs are due to noise in the digitizing (two-level) process, and these are eliminated, while runs more than one element long are kept intact. Thus, sharpness of the pictures is very rarely reduced. It should be noted that this modification strategy is superior to the one in which a 2:1 horizontal subsampling of the picture material is attempted, since in our case there is virtually no loss of horizontal

resolution (except for edges which are one element wide), whereas subsampling entails a definite loss of resolution. Figures 1 and 2 show the results of such preprocessing. Eight original CCITT pictures are shown in Fig. 1, and the modified pictures are shown in Fig. 2. The eight CCITT documents are approximately 8 ½ by 11 inches in size and contain 2128 scan lines with 1728 picture elements (pels) per line. Comparison of pictures in Fig. 1 and Fig. 2 indicates that, for most documents, the distortion due to picture modification is hardly noticeable. There is some distortion, however, as seen in Document 6. In this document, some vertical lines in the graph are broken. This is expected, since any vertical line that is only one pel wide will be removed if the black pel falls on an even sample and is surrounded by odd samples that are white. A slight degradation is seen in some of the other documents (4 and 7) which have small case text material. Whether such a distortion is tolerable or not may depend upon the contents of the document. In any case, it appears that for the majority of the documents the distortion may be tolerable.

Having modified the picture, we now describe adaptation of one of our ordering techniques. Elimination of single runs allows us to process alternate samples differently. As shown in Fig. 3a, even and odd samples are treated differently. Every odd sample is predicted by the previously transmitted pels, as shown in Fig. 3b. Prediction error of the even samples is obtained and used only when necessary. The

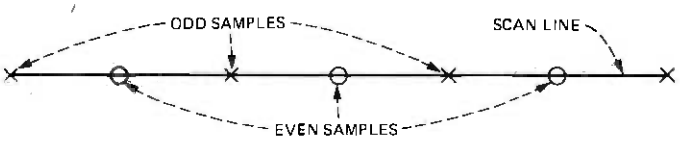

(a)

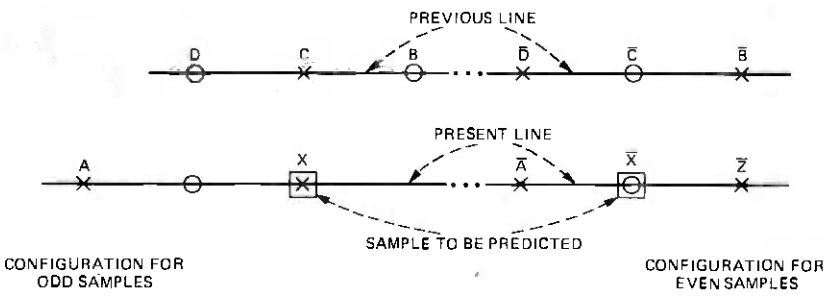

NOTE: SAMPLE X (OR $\bar{X}$) IS PREDICTED BY USING SAMPLES A, B, C, D (OR $\bar{A}$, $\bar{B}$, $\bar{C}$, $\bar{D}$)

(b)

Fig. 3—(a) Definition of alternate samples and (b) Corresponding prediction patterns.

predictor is developed in a standard way as the one which minimizes the probability of making an error if the surround has a given pattern. The pattern used for making the prediction is given in Fig. 3b. More details of the predictor appear in Ref. 8. Since all the single runs have been eliminated by preprocessing, if the two adjacent odd samples are of the same color, the in-between even sample is also of the same color and, therefore, excluded from transmission. Also, in certain other patterns (e.g., 01X0 or 10X1; X = even sample), where the color of the even sample is predictable, its prediction is not transmitted. However, in cases where the color of the adjacent odd samples is different and the color of the in-between even samples is not always predictable, the even sample is predicted by using the pattern shown in Fig. 3b. We note that sample $\bar{Z}$ is not used in the prediction process. Since knowing the color of $\bar{A}$, the color of $\bar{Z}$ is known in all cases where it is required to predict the even samples. In our simulations, we tried predicting even sample, $\bar{X}$, by using the surrounding pattern produced by pels $\bar{A}$, $\bar{B}$, $\bar{C}$, and $\bar{D}$, as well as by only using pel $\bar{C}$. We found very little difference in the results and, therefore, used $\bar{C}$ as the predictor for reasons of simplicity. Having obtained the prediction errors, we now order them. Many variations of the ordering are possible. We describe one of them and mention another. A memory having a number of cells equal to the number of elements in a line (N) is used. As shown in Fig. 4a, if the cells are numbered 1 to N, then the prediction errors corresponding to good states of odd samples are loaded in the memory starting with cell address 1 and increasing sequentially by one; however, the prediction errors corresponding to bad states of odd samples are loaded in the memory starting with the address ($N/2$) and decreasing sequentially by one. The prediction errors of the required even

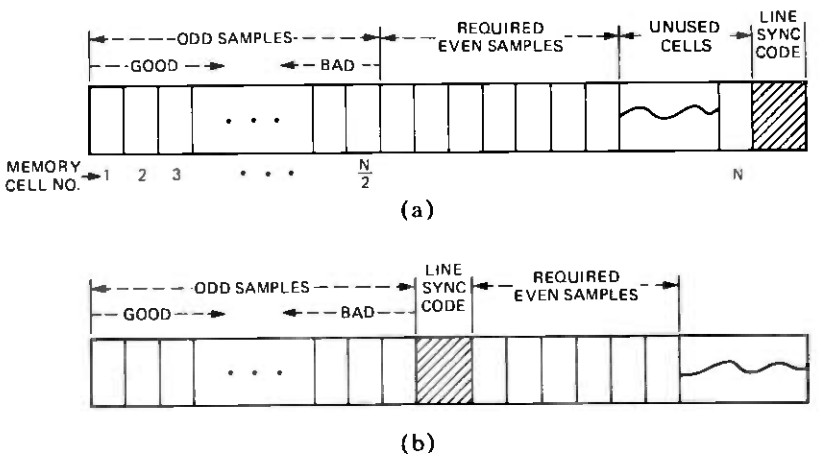

Fig. 4—Two configurations for ordering data from odd and even samples.

samples, on the other hand, are loaded in the memory starting address $(N/2 + 1)$ and increasing sequentially by one. For most of the lines, this line memory containing ordered prediction errors will not be filled, since the required even samples will be less than $(N/2)$. Having ordered the line, we code the run lengths of the contents of the memory, skipping the unfilled memory cells. Here again, many variations are possible. We have used two separate codebooks: one for the run lengths of prediction errors from odd samples and one for the run lengths of prediction errors from even samples. The run is broken at $N/2$, i.e., the boundary between the even and odd samples. This does not allow us to drop any runs of odd samples. To drop the first run in the good region of the odd samples, an alternative arrangement, shown in Fig. 4b, is used. Here the line sync is transmitted between the coded data from the even and odd samples of a line. Dropping the first run is possible since the same code is used for the good and bad region of the odd samples and since the number of encoded odd samples in a line is fixed $(=N/2)$. If it is desired to use three sets of codes (one for the good region of the odd samples, one for the bad region of the odd samples, and one for the required even samples), then the first run of the odd samples cannot be dropped. However, we can still use our previously published extensions of ordering techniques[8] such as bridging, dropping last decodable run for the data from odd samples, since the boundary between the data from the odd and even samples is clearly defined by the line sync code. Here again, we skip the unfilled memory cells of the even samples. Although these extensions would make the algorithm more efficient, we did not simulate them.

Table I shows the simulation results for the eight CCITT pictures. We show results of three other schemes (taken from Ref. 8) for the purposes of comparison. For each scheme and each picture, we compute statistics of run lengths of "zeros" (no prediction errors) and "ones" (prediction errors) and then calculate entropy in bits/pel. The predictor is optimized for each individual picture. It is seen from this table that the ordering techniques with picture modification (row 4) result in entropies which are between 0.018 to 0.115 bits/pel. Compared to one-dimensional run-length coding, these entropies are less by 48 percent on the average. Also, comparing with one of our best ordering techniques (from Ref. 8), the reduction in entropy is 10 percent on the average. We note that many extensions of ordering techniques which were used to generate entropy numbers of row 3, Table I, can be used along with picture modification for further reduction in bit rate.

III. CONCLUSIONS

The picture modification strategy described in this paper is rather simple, easy to implement, and does not result in excessive degradation

Table I—Entropy results for the eight CCITT documents. Note that the entropy numbers do not include certain bits required for housekeeping (line sync, color of the beginning run of each line, etc.) and the predictor is optimized for each picture.

No.	Coding Algorithm	Entropy (bits/pel) CCITT Image Number							
		1	2	3	4	5	6	7	8
1	One-dimensional run-length coding	0.0505	0.0447	0.0914	0.1652	0.0988	0.0679	0.1791	0.0870
2	Run-length coding of prediction errors	0.0466	0.0373	0.0693	0.1640	0.0795	0.0482	0.1678	0.0678
3	Run-length coding of ordered prediction errors with two sets of codes for good and bad region, bridging of good-bad boundary, last decodable run dropped	0.0324	0.0210	0.0506	0.1239	0.0569	0.0312	0.1250	0.0398
4	Ordering techniques with picture modification (single element runs eliminated)	0.0294	0.0183	0.0441	0.1130	0.0505	0.0309	0.1153	0.0351

of the pictures. Our previously described ordering techniques can be modified to reduce the bit rates. The new technique gives bit rates between 0.018 to 0.115 bits/pel. This is about 48 percent less than bit rates obtained by simple one-dimensional run-length coding.

REFERENCES

1. M. Takagi and T. Tsuda, "Comparison of Facsimile Bandwidth Compression Using Two-Dimensional Prediction and Signal Modification," Proc. Int. Commun. Conf. 1976, Vol. III, pp. 47-26 to 47-31.
2. V. Margner and P. Zamperoni, "Representation of Two-Level Images Via Reduced Pattern Supply," Nachr. Electron., *5* (1976), pp. 109–113.
3. V. Margner and P. Zamperoni, "Data Reduction for Print and Graphics by Means of Feature Reduction," Nachrichtentech. Z., *29*, No. 7 (1976), pp. 525–530.
4. T. Usubichi, S. Mizuno, and K. Iinuma, "Efficient Facsimile Signal Data Reduction by Using a Thinning Process," NTC Proc. 1977, pp. 49:2–1 to 49:2–6.
5. D. Ting and B. Prasada, "Preprocessing Techniques for Digital Facsimile," Proc. Int. Conf. Commun., June 1978, pp. 48.5.1–48.5.6.
6. A. N. Netravali, F. W. Mounts, and E. G. Bowen, "Ordering Techniques for Coding of Two-Tone Facsimile Pictures," B.S.T.J., *55* No. 10 (December 1976), pp. 1539–1552.
7. A. N. Netravali, F. W. Mounts, and J. D. Beyer, "Techniques for Coding of Dithered Two-Level Pictures," B.S.T.J., *56* No. 5 (May–June 1977), pp. 809–819.
8. F. W. Mounts, A. N. Netravali and K. A. Walsh, "Some Extensions of the Ordering Techniques for Compression of Two-Level Facsimile Pictures," B.S.T.J., *57*, No. 8 (October 1978), pp. 3057–3067.

THE BELL SYSTEM TECHNICAL JOURNAL
Vol. 58, No. 4, April 1979
Printed in U.S.A.

Rapid Automatic Index Profiling of Whole-Fiber Samples: Part I

By L. M. BOGGS, H. M. PRESBY, and D. MARCUSE

(Manuscript received May 1, 1978)

A new interferometric method not requiring any sample preparation is presented for determining the refractive-index profiles of optical fibers. The whole fiber is immersed in index-matching oil and placed transversely under an interference microscope. The determination of the refractive index distribution for an arbitrary, circularly symmetric fiber core requires the solution of an integral equation. In this first of two papers on the subject, we describe a method which accomplished its solution by assuming that the fiber core consists of a large number of concentric circular cylinders of step-wise constant refractive index. The index distribution can then be obtained by determining the index values of each layer successively. The method has been applied to double- and single-pass interferometric arrangements which are being compared here. The single-pass method is reproducible to about 1 percent and provides the complete index distribution within minutes with the help of a computer-controlled video-analysis system. The results of this method are in excellent agreement with profiles obtained from polished slabs of the same fiber.

I. INTRODUCTION

Multimode optical fiber systems can achieve high bandwidth if the refractive index profile of the fiber core approximates very closely the theoretically predicted almost-parabolic shape. This poses the problem for the fiber fabricator of being able to produce preselected index profiles with high accuracy and also of being able to check whether the desired profile has actually been obtained. It is thus necessary to have measuring equipment capable of displaying the index profiles of fibers after manufacture quickly, accurately, and, if possible, nondestructively.

Means for measuring refractive index profiles by accurate interferometric techniques have previously been described.[1-3] However, the

most successful earlier technique, the slab method, requires elaborate sample preparation because a thin slice has to be cut out of the fiber and polished to a high degree of flatness and parallelism.

If the interferogram could be made by shining light not longitudinally but transversely through the fiber core, fiber preparation would become unnecessary, except for the need for preventing the fiber cladding from contributing a very large amount of fringe shift. This can be accomplished by submerging the fiber in index-matching oil. This general idea has been described in Ref. 4. A similar method has been used in Ref. 5, but the analysis used to extract the refractive index profile from the interferogram was restricted to power law profiles that can be characterized by two constants, the refractive index difference (between the maximum value at the core center and the cladding value) and the power law coefficient. Actual fibers have refractive index distributions that do not fit a simple power law. Most fibers at present have an index depression on axis and at the core boundary. But even the comparatively regular parts between core center and core boundary do not always conform to one definite power law profile. It is thus necessary to evaluate the transverse interferograms without assuming a particular functional shape for the index distribution. We describe such a method in this paper.

Because the fiber need not be cut and polished for transverse illumination, we call this procedure the "whole-fiber method."

The refractive index distribution $n(r)$ is related to the fringe shift pattern by an integral equation which we solve by replacing the function $n(r)$ by a staircase approximation. Our method is based on the assumption that the index profile is of rotational symmetry and neglects the effect of ray bending inside the core. The staircase approximation of the index curve is equivalent to an approximation of the original integral (of the integral equation) by a discrete sum and to solving the resulting system of coupled equations.

As a particular matter, the interferogram can be obtained in two different ways. If a single-pass interference microscope is available, the light beam need pass the fiber core only once. Some conventional microscopes can be equipped with an interference objective attachment that functions as an interferometer if the sample is placed on a mirror and the light beam is allowed to pass back and forth through it. This double-pass method suffers from the disadvantage that each ray is bent much more severely in passing the core twice, so that ray bending is no longer negligible. We present a comparison of the single- and double-pass methods in this paper. Furthermore, we describe an automated, computer-controlled video system for performing the interference measurements and data evaluation automatically and compare the results of the whole-fiber method with those of the more accurate slab method.

II. CIRCULAR INDEX METHOD: DOUBLE-PASS INTERFEROMETER

The experimental arrangement for double-pass interferometric observations is shown in Fig. 1. The double-pass interferometer has the advantage of being much cheaper than a commercial interference microscope because it utilizes an interference objective as an attachment to an ordinary microscope. A short section of the fiber is immersed in index matching oil and placed on a metallized optical flat serving as a mirror. The optical flat can be heated to achieve perfect match between the oil and the fiber cladding. The light source is a He-Ne laser whose beam is passed through a moving diffuser. A typical interferogram is shown in Fig. 2. The information needed to compute the refractive index distribution of the fiber core is obtained by measuring the displacement of one of the fringes from its straight level in the cladding.

Next, we describe how the information about the refractive index distribution is extracted from the interferogram. We assume that the light rays pass the fiber core without deflection, using only the fact that their phases are retarded according to the length of their optical paths. In addition, we assume that the fiber core consists of a large number of concentric rings each with a constant index of refraction. We now evaluate the index step by step beginning at the periphery and proceeding toward the center. Figure 3 shows clearly that it is possible to determine the index value of each ring if we use the fact

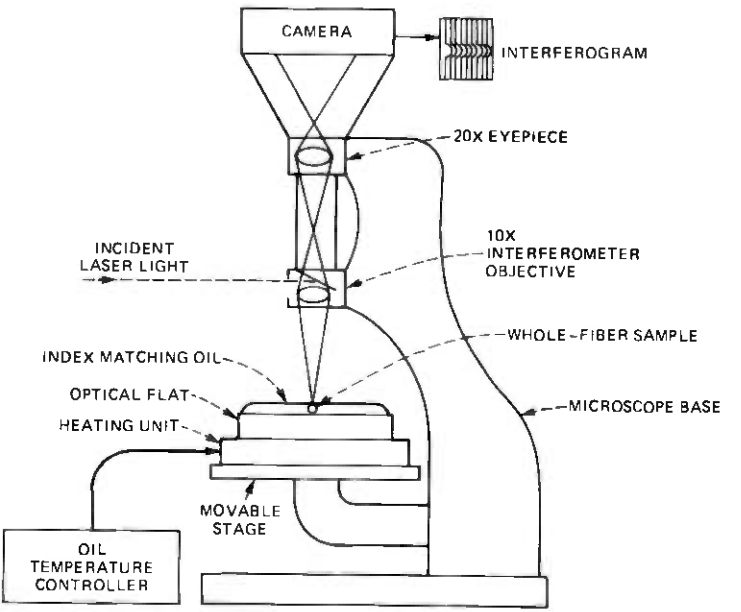

Fig. 1—Microscope set-up for making double-pass interferogram.

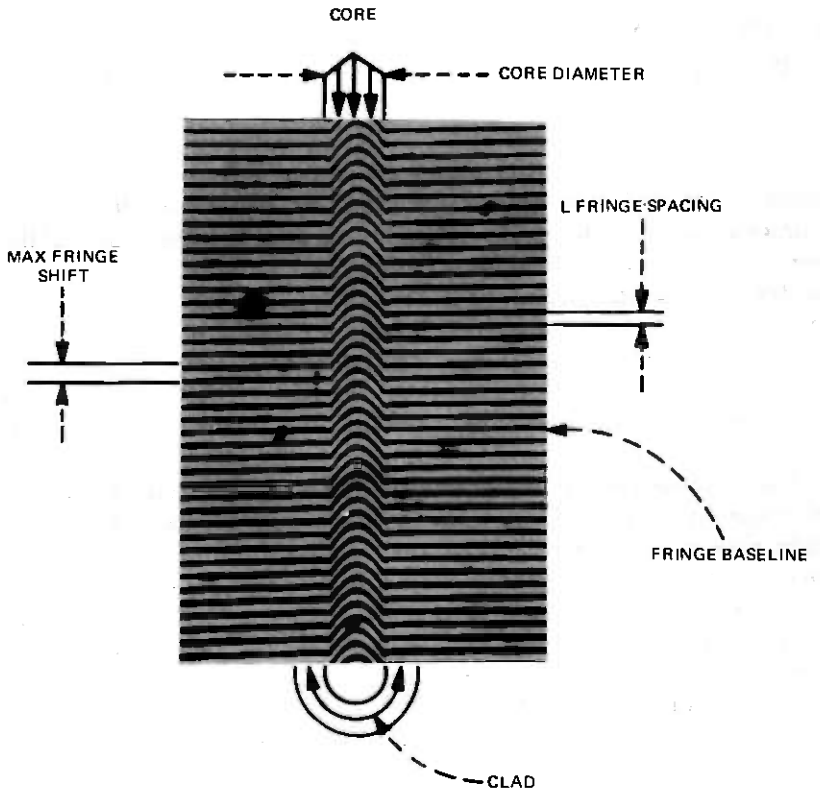

Fig. 2—Interferogram of whole-fiber sample obtained with double-pass set-up.

that the index values of all preceding rings are already known. We call this method of analysis the "circular index method."

The relationship between the relative optical phase shift ψ, fringe spacing L, and fringe shift Q is

$$Q(P) = \frac{L}{2\pi}\psi(P). \tag{1}$$

If we designate the radius of the Jth ring by $R(J)$ and note that the length of a single path through ring J is

$$S(P, J) = 2\{[R^2(J-1) - R^2(P)]^{1/2} - [R^2(J) - R^2(P)]^{1/2}\}, \tag{2}$$

we find that the double-path fringe shift through the core, passing through ring P on the horizontal axis, can be expressed as follows:

$$Q(P) = 2\frac{L}{\lambda}\left\{\Delta n(P)S(P, P) + \sum_{J=1}^{P-1}\Delta n(J)S(P, J)\right\}.$$

$\Delta n(J)$ is the difference between the refractive index value of ring J and the index of the cladding. Solving for $\Delta n(P)$ yields the relative

refractive index of ring P in terms of the phase shift (measured at the corresponding position) in terms of the relative index values of all preceding rings.

$$\Delta n(P) = \frac{1}{S(P, P)} \left\{ \frac{\lambda Q(P)}{2L} - \sum_{J=1}^{P-1} \Delta n(J) S(P, J) \right\}. \tag{3}$$

The iterative evaluation of this equation starts at an arbitrary radius large enough to ensure that $Q(1) = 0$ and $\Delta n(1) = 0$.

Note that the thickness of the rings, and hence the spacing at which the fringe shift values are sampled, need not be uniform. Our method of analysis also shows clearly that measurement errors must build up so that the refractive index near the fiber axis is known far less accurately than the index near the core boundary. This problem is aggravated by the fact that the weighting factor $1/S(P, P)$ in (3) becomes larger closer to the core center. However, these features of our method seem unavoidable since the same type of error build-up

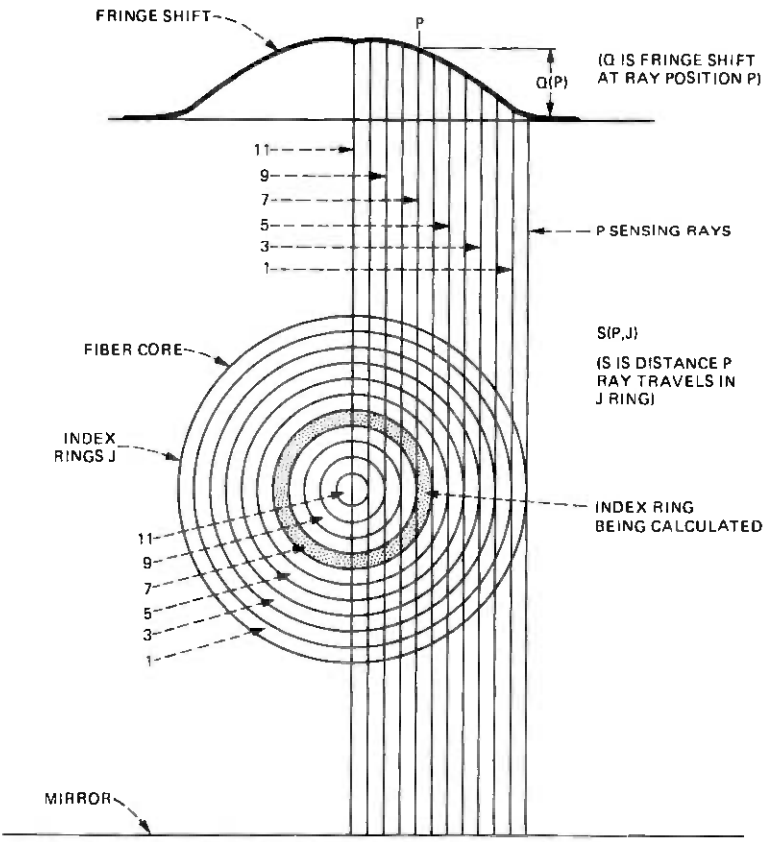

Fig. 3—Circular-index calculation scheme.

occurs also in another method (described in a companion article[6]), which is based on an analytical solution of the integral equation. Figure 4 shows a typical plot of Δn vs radial position together with a power law curve fitted to the data. Four points near the fiber core center are omitted from the curve-fitting program, since they clearly did not conform to a simple power law.

III. CIRCULAR INDEX METHOD: SINGLE-PASS INTERFEROMETER

The circular index method, previously discussed, ignores bending of the sensing light rays as they pass through the core on their way to the mirror and on their return through the fiber. In actuality, ray bending does occur, and the amount of bending is readily computed by successive applications of Snell's law. Figure 5 shows the rays vertically incident from the top of the core and tilted from the vertical direction on the return from the mirror. This figure shows clearly that

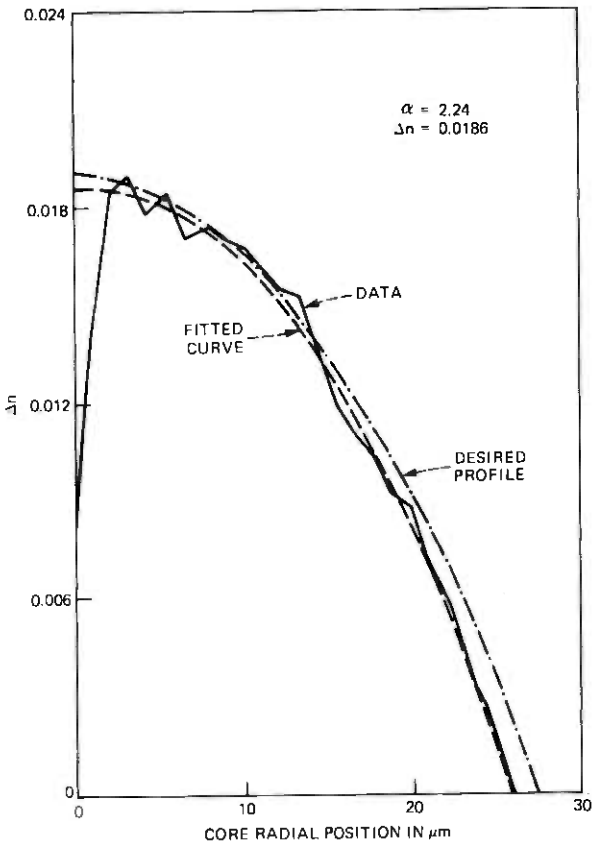

Fig. 4—Index profile obtained from double-pass interferogram.

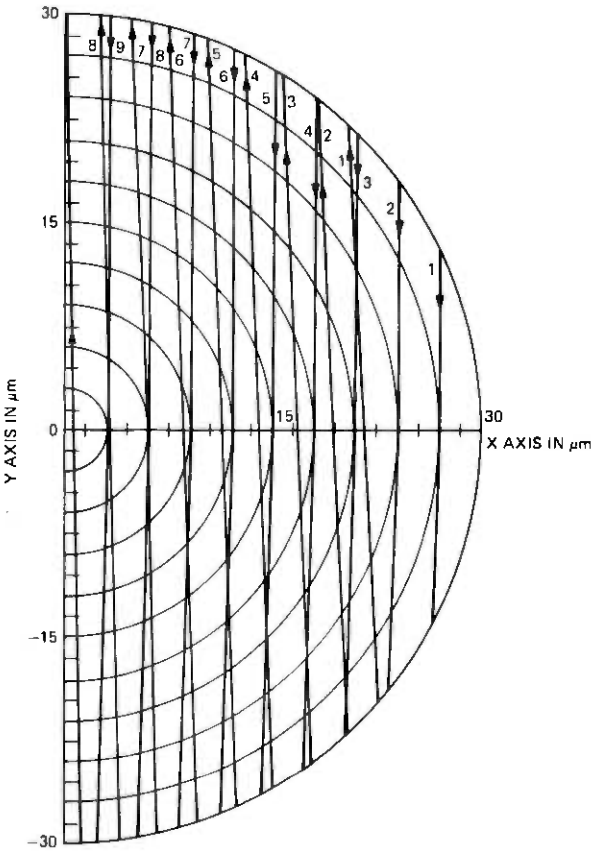

Fig. 5—Ray bending of incident and reflected rays in double-pass arrangement.

significant ray displacement occurs, particularly near the core boundary. If single-pass interferometry of the Mach-Zender type were used, the sensing ray would pass through the fiber only once. The amount of ray bending in this case is shown in Fig. 6. The point at which the ray exits the core is translated only about ⅛ the distance experienced in the two-pass case. Furthermore, the change in the exit angle caused by the core is only about ½ the amount of the two-pass case.

Although an α of 1.0 was assumed for the calculated ray bending effects shown in Figs. 5 and 6, equally significant ray bending occurs for other α values, for example, for $\alpha = 2$. The ray displacement shown in Fig. 5 suggests that the double-pass method tends to eliminate fine structure from the interferogram and hence from the refractive index curve. Fibers made by modified chemical vapor deposition typically

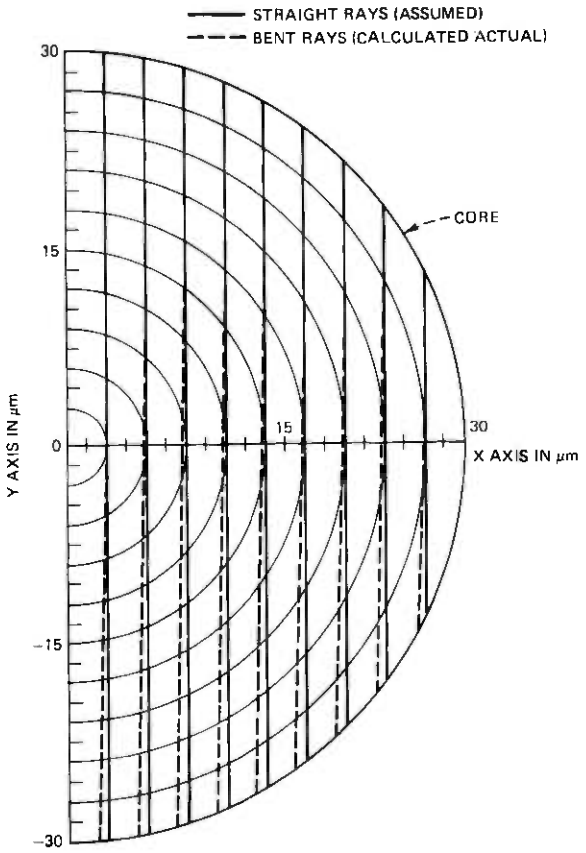

Fig. 6—Ray bending of incident rays in single-pass arrangement.

show the deposition layers if high resolution methods are used. Such fine structure is usually seen with the single-pass method, particularly near the fiber axis.

A comparison of double-pass and single-pass interferograms of the same fiber sample is shown in Fig. 7. The different magnification used for the two methods is inherent in their practical realization. Interference objectives for conventional microscopes are at present not available with high magnification. Interference microscopes, on the other hand, are equipped with high power objectives. Close scrutiny of Fig. 7 reveals that the single-pass interferogram shows the central dip[7] in the fiber core while this feature is less obvious from the double-pass interferogram. The more sophisticated single-pass method, using a

high precision interference microscope, is a definite necessity if fine detail of the refractive index distribution is to be resolved. To take full advantage of the inherently rapid nature of this profiling method makes it desirable to automate the measurement. A description of the automated equipment is presented in the following section.

IV. AUTOMATIC SINGLE-PASS PROFILING

The experimental arrangement for automatic single-pass profile measurements is shown in Fig. 8. The heart of the system is a Leitz dual-beam, single-pass, transmission interference microscope. This instrument is essentially a combination of two microscopes and an interferometer in such a way that the magnified image of the object appears together with interference fringes. The interference microscope has been extensively used to perform precise refractive index profiling of optical fibers by examining polished slab samples.[1-3] Techniques have also been developed to make measurements of the fringe

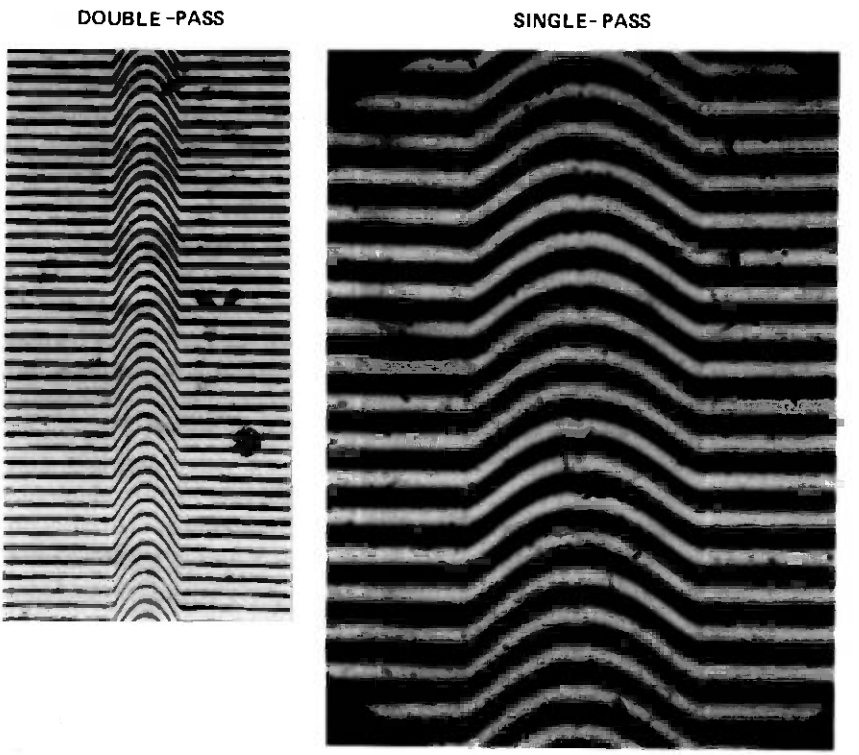

Fig. 7—Comparison of double-pass and single-pass interferograms of the same fiber sample.

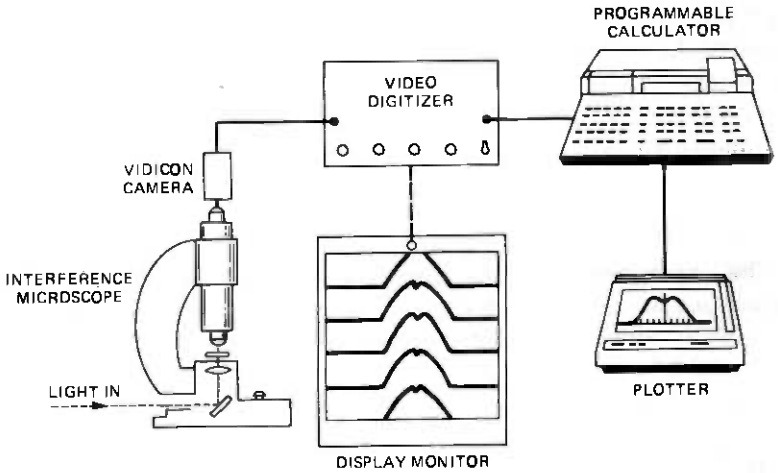

Fig. 8—Elements of the set-up to perform automatic-refractive index profiling of whole-fiber samples with a single-pass interference microscope and a video analysis system.

displacements directly in the microscope's output field[3,8-11] without the time-consuming need to process photographs.

In our application, a short length of fiber (~1 cm) is inserted into index-matching oil in the sample arm of the microscope. However, if desired, the unbroken fiber could be placed under the microscope. A similar thickness of matching oil is placed in the reference beam. We found that an excellent match to the cladding could be achieved at an observation wavelength of $\lambda = 0.9$ μm with matching oil of index $n = 1.457 \pm 0.0005$; no heating of the oil was employed.

The subsequent measurement procedure is similar to that of Ref. 9 and involves video detection and digitization of the interference fringes under computer control. The output field of the microscope is detected with an infrared-enhanced, silicon-target vidicon whose electronics were modified to optimize signal stability and to reduce voltage drift to minimum levels. The video signal is sent to a video digitizer that has the capability of addressing and encoding discrete picture elements in the television frame. The digitizer resolves 480 picture elements on the Y axis and 512 elements on the X axis. The X and Y position data inputs are provided by the 16-bit duplex input/output (I/O) interfaces of a Hewlett Packard 9825A computer. Encoding is to 8 bits or 256 gray levels and the digitized video is received by the calculator as 8 bits, parallel binary.

The digitizer also incorporates a video output display which permits the observation of the scene being processed and the monitoring of the encoding on the same screen. Figure 9 is a photograph of the display showing a sample of an index-matched graded-index fiber observed at

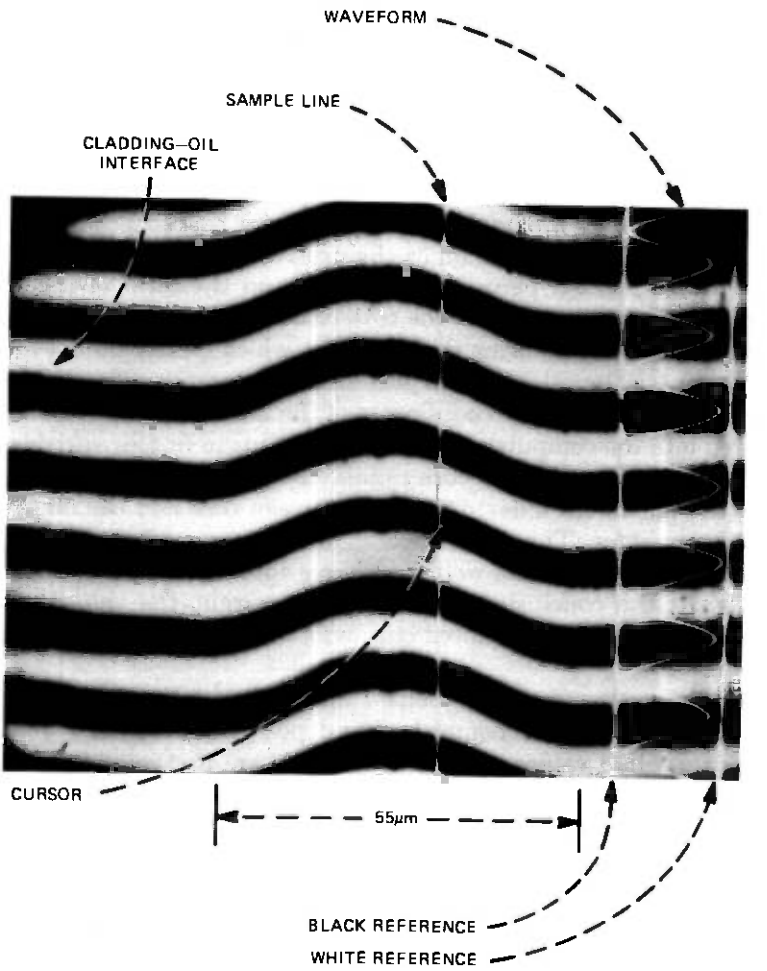

Fig. 9—Photograph of monitor showing graded-index fiber and associated encoding display of sample line, cursor, and intensity waveform. Note that the interface between the matching oil and the cladding is barely visible, indicating a good match.

a wavelength of $\lambda = 0.9$ μm. Location of the point being encoded is indicated by a dot cursor and the gray-scale value for all Y elements along a sample line at the selected X positions is displayed as a waveform at the side of the monitor screen. Care is taken when setting up the sample to ensure that the axis of the fiber is normal to the vidicon scanning axis and that the straight fringes in the cladding region lie nearly parallel to the scanning axis. Residual fringe tilt relative to the scan lines is compensated for by the data evaluation program.

The objective of the encoding process is to accumulate intensity-vs-position data so that the displacement of a fringe from its cladding

level can be determined accurately as a function of radial position. This is accomplished by a new automatic, rapid, fringe finding and tracking procedure the details of which are presented in a companion paper.[6] Having determined the fringe displacement, the computer calculates Δn by the method described in a previous section and then plots the index profile along with coordinates and labeling on an XY plotter.

The computer's program then determines a best-fit power-law (α) curve to the index profile. Since the profiles of most currently fabricated fibers contain perturbations, mainly in the form of a central index depression and tails at the core-cladding interface, the program provides means of ignoring these regions, which clearly do not follow the power law, by selecting the portions of the profile over which a fit is to be determined. The coordinates of the limits of these regions are entered into the computer which then proceeds to fit four variables to the given profile, viz., the core radius, the shift of the center of the core, the maximum index difference between core and cladding, and the α parameter. The program also determines a "fitting error" to provide a measure of how well the α curve approximates the measured profile. At the conclusion of the fitting program, the values of the various parameters are printed out and a best-fit α curve is drawn by the plotter.

The above procedure was used on eight different GeO_2-doped fibers fabricated by modified chemical vapor deposition (MCVD). The results, giving the fitted values as described above, are presented in Table I

Table I—FIT parameter comparison

Fiber ID	Δn	Core-radius (μm)	Alpha	FIT Error (%)	FIT Bounds (μm)
20G61BX					
Slab	0.0202	22.29	2.23	1.5	5–20
Whole	0.0190	21.39	2.36	2.3	5–20
14F305B					
Slab	0.0183	27.67	2.32	1.1	5–25
Whole	0.0174	27.07	2.35	0.8	5–25
20W97A					
Slab	0.0227	27.89	1.49	1.0	5–25
Whole	0.0220	26.69	1.57	1.0	5–25
20W99A					
Slab	0.0230	27.22	1.48	0.8	8–25
Whole	0.0221	27.04	1.45	0.8	8–25
19F53BX					
Slab	0.0207	22.94	2.17	0.9	4–21
Whole	0.0194	22.31	2.39	1.9	4–21
15F309B					
Slab	0.0184	25.60	2.25	1.2	5–22
Whole	0.0185	24.76	2.43	2.7	5–22
14A186B					
Slab	0.0212	26.74	1.70	0.6	12–25
Whole	0.0228	26.94	1.75	0.6	12–25
19A118A					
Slab	0.0094	24.95	2.06	0.7	3–22
Whole	0.0089	24.90	2.04	1.47	3–22

across the rows labeled "Whole." Also shown are the limits of the fitted region. It is important to note that, since these profiles are not ideal α distributions, the value of α depends on the limits of the region over which the fit is made. We have found that slight changes of these limits can affect the α value by about 5 percent.

The reproducibility of the measured profile is limited mainly by the build-up of errors in the integration scheme, an effect which is treated in detail in Ref. 6. Resulting variations of the index were consistently found to be a few parts in 10^4, in excellent agreement with a theoretical analysis of this effect.[6]

To check these results and establish the validity of this method of index-profiling, we prepared polished slabs of the same fiber samples and measured their profiles by the already established techniques of interference microscopy.[2] These measurements utilized the same automatic video analysis system with appropriate changes in the scanning and index evaluation procedures tailored to the slab geometry.[9] The experimental reproducibility of the profile for the slab samples is limited mainly by noise on the video signal. Variations in the index

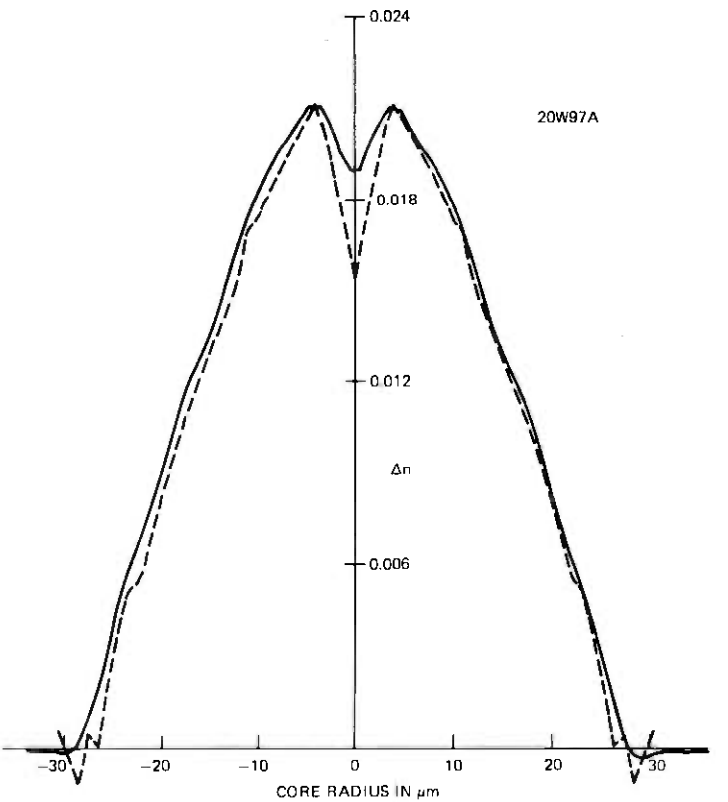

Fig. 10—Comparison of whole-fiber profile (broken line) with slab profile (solid line).

amount to a few parts in 10^5. This is about an order of magnitude better than the whole-fiber method which, as mentioned, is inherently limited by error build-up. This level of accuracy, however, reflects only the repeatability of the measurement and the absolute error depends upon a precise knowledge of the sample's thickness and its degree of flatness.[10]

For comparison with the whole-fiber results, the α fit to the slab profiles were made over the same region. Results obtained by the slab method are shown in Table I across the rows labeled "Slab." The agreement is seen to be very good, with the average difference of the maximum Δn values and the α values being about 4 percent and the average difference of the core radii being about 2 percent. Generally, the absolute values of Δn and core radii for the slabs are slightly larger than the whole fiber results. These discrepancies, however, are understandable because they are within the experimental precision of the

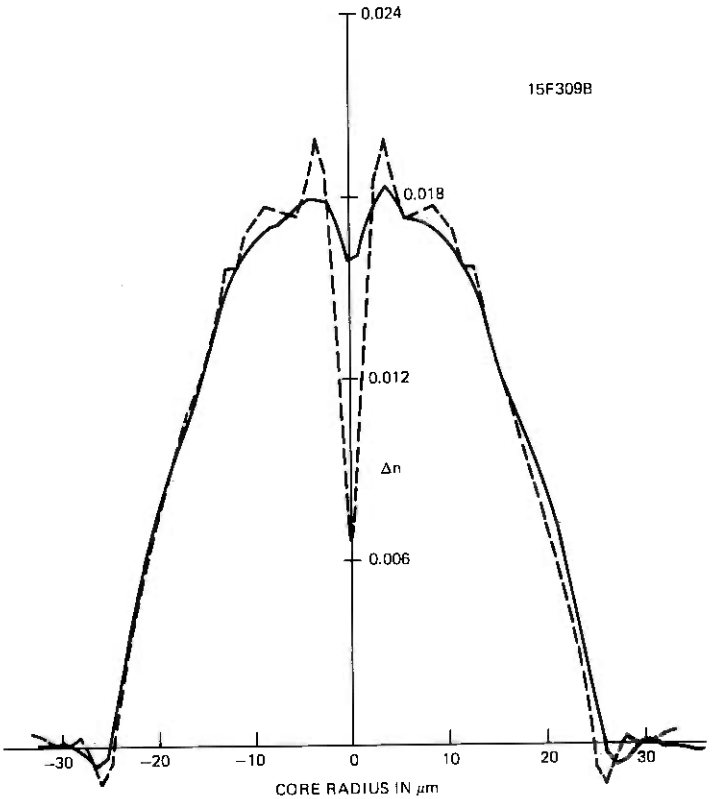

Fig. 11—Same as Fig. 10, but for a second fiber. The discrepancy of the radii on the right can be due to a slightly elliptical core which would be detected by the slab technique but not by the whole-fiber method since the latter assumes circular symmetry.

thickness measurements for the slabs (about 5 percent), which will affect the Δn level, and the error introduced by the lack of a perfect index match to the cladding of the whole fibers, which tends to reduce their observed radii (if the matching oil has a slightly higher index than the cladding). There is also the complication of focussing effects due to the boron layer, which can act differently for both cases, changing the apparent radius. In addition, the whole fiber analysis assumes circular symmetry, whereas the slab results are distinct for each side of the core. Thus, lack of circular core will not be apparent in the whole fiber results.

Besides the good agreement of the fitted data, the details of the index profiles themselves are in excellent correspondence. Generally, distinctive features of the profiles are present in both cases, as can be seen in the three typical profiles shown in Figs. 10 to 12. A tendency of the whole-fiber technique is to display more clearly the layers in the

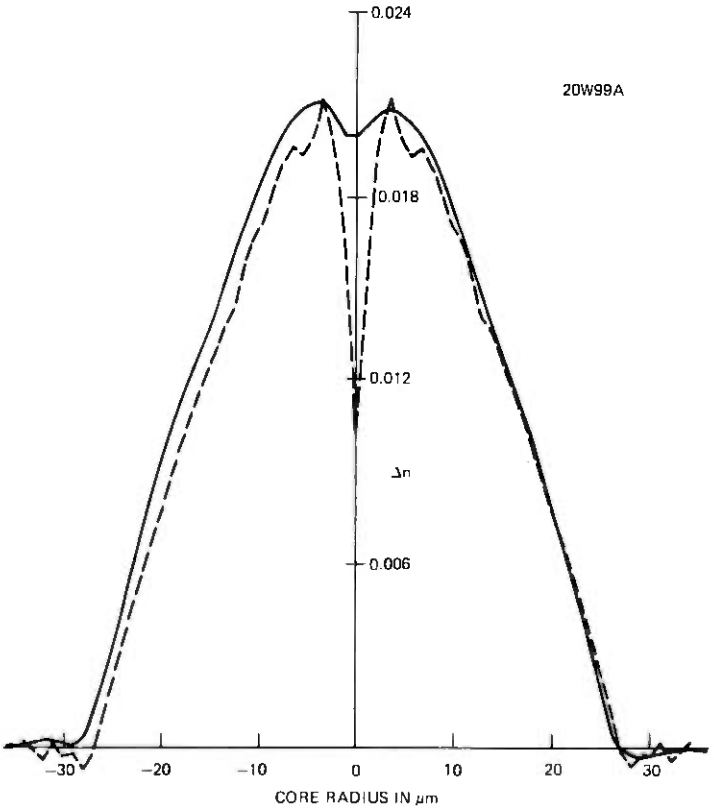

Fig. 12—Same as Fig. 10, but for a third fiber. The whole-fiber method tends to emphasize structural details, as explained in the text.

fiber core which exist especially near the axis. This is due to the fact that the whole-fiber method tends to magnify any fluctuations, and consequently also systematic ones, near the core center. The central index depression is also resolved to a greater degree by the whole-fiber method since this region, in the slab case, possesses a large index gradient which cannot be resolved by the interference fringe passing through it. The depth of the depression, as displayed by the whole-fiber profile, depends on how closely a vertical scanning line comes to the axis of the fiber, accounting for the variations that are observed in this region of the profiles.

The whole-fiber method shows itself to be a viable technique to measure index profiles, although with somewhat less inherent attainable precision than the slab method. Its main advantage of not requiring sample preparation and thus providing information within minutes should make it a very valuable diagnostic tool. Profile information can now be rapidly provided to allow adjustments in fiber-preform fabrication parameters to attain more ideal index distributions. Fibers can now also readily be evaluated, rated, and selected nondestructively for specific applications, depending upon the quality of their profiles, almost immediately upon production. In addition, the method also has the capability of providing information on core and cladding diameter values.

REFERENCES

1. C. A. Burrus and R. D. Standley, "Viewing Refractive-Index Profiles and Small-Scale Inhomogeneities in Glass Optical Fibers: Some Techniques," Appl. Opt., *13* (1974), p. 2365.
2. H. M. Presby, W. Mammel, and R. M. Derosier, "Refractive Index Profiling of Graded Index Optical Fibers," Rev. Sci. Instr., *47* (1976), p. 348.
3. H. M. Presby and I. P. Kaminow, "Binary Silica Optical Fibers: Refractive Index and Profile Dispersion Measurements," Appl. Opt., *15* (1976), p. 3029.
4. M. E. Marhic, P. S. Ho, and M. Epstein, "Nondestructive Refractive-Index Profile Measurement of Clad Optical Fibers," Appl. Phys. Lett., *26* (1975), p. 574.
5. M. J. Saunders and W. B. Gardner, "Nondestructive Interferometric Measurement of the Delta and Alpha of Clad Optical Fiber," Appl. Opt., *16* (1977), p. 2368.
6. H. M. Presby, D. Marcuse, L. Boggs, and H. W. Astle, "Rapid Automatic Index Profiling of Whole Fiber Samples: Part II," B.S.T.J., this issue, pp. 883–902.
7. H. M. Presby, "Axial Refractive Index Depression in Preforms and Fibers," Fiber and Integrated Optics, *2*, No. 2.
8. H. M. Presby and H. W. Astle, "Optical Fiber Index Profiling by Video Analysis of Interference Fringes," Rev. Sci. Instr., *49* (1978), p. 339.
9. H. M. Presby, D. Marcuse, and H. W. Astle, "Automatic Refractive Index Profiling of Optical Fibers," Appl. Opt., *17* (1978), p. 2209.
10. J. Stone and R. M. Derosier, "Elimination of Errors due to Sample Polishing in Refractive Index Profile Measurements by Interferometry," Rev. Sci. Instr., *47* (1976), p. 885.
11. B. C. Wonsiewicz, W. G. French, P. D. Lazay, and J. R. Simpson, "Automatic Analysis of Interferograms: Optical Waveguide Refractive Index Profiles," Appl. Opt., *15* (1976), p. 1048.

THE BELL SYSTEM TECHNICAL JOURNAL
Vol. 58, No. 4, April 1979
Printed in U.S.A.

Rapid Automatic Index Profiling of Whole-Fiber Samples: Part II

By H. M. PRESBY, D. MARCUSE, H. W. ASTLE, and L. M. BOGGS

(Manuscript received May 1, 1978)

Automatic, nondestructive methods have been developed for measuring and analyzing the refractive index distribution of a fiber that is immersed in index-matching oil and illuminated transversely to its axis in a single-pass interference microscope. The output field of the microscope is automatically processed with a video-digitized, computer-controlled system, and the profile is determined by the solution of an integral equation that can handle arbitrary variations in the index distribution. The resulting profiles are reproducible to approximately 1 percent and can be determined within a few minutes after fiber fabrication. Details of a rapid video scanning procedure and of error estimates involved in solving the integral equation are presented along with representative profiles.

I. INTRODUCTION

One of the most important parameters in determining the usefulness of graded-index multimode optical fibers in high-capacity communication systems is their refractive index profile. The closer the profile conforms to the required optimum distribution, the greater the resulting bandwidth of the fiber. As demand for high-capacity fibers increases and as fabrication facilities are optimized to produce them dependably, it becomes very important to have reliable, accurate, and fast methods to measure the fiber's refractive index distribution. These methods would greatly aid in tailoring more ideal profiles and would form the basis of a fiber evaluation and sorting scheme in which fibers are selected for specific applications, depending upon the quality of their profiles, almost immediately upon production.

One of the most sensitive means of measuring the index profile is by interference microscopy utilizing cut and polished fiber-slab samples.[1,2] While this technique allows very precise measurements,[3,4] it requires

a high precision, time-consuming procedure of preparing the thin (on the order of 50 μm) and extremely flat samples. This can be alleviated somewhat by simultaneously processing many samples and utilizing an automatic analysis scheme to save time in the evaluation;[5,6] however, it would still be preferable to avoid any sample preparation.

A technique requiring no sample preparation based on interferometry has been proposed in which a sample of the whole fiber is immersed in index-matching oil and illuminated perpendicular to its axis.[7] The refractive index profile is subsequently obtained from the fringe shifts by mathematical methods which were shown to operate for fibers whose profiles are a quadratic function of the radius of the core. This method has also been extended[8] to a more general class of profile shapes describable by a parameter α which appears in the expression describing the index distribution $n(r)$,

$$n(r) = n_0[1 - 2\Delta(r/a)^\alpha]^{1/2},$$

where r is the distance from the center of the core, a is the core radius, and $\Delta n \equiv n_o - n_a$. Assuming that α is constant, this treatment showed that Δn and α could be determined to better than ± 10 percent. The assumption of constant α, however, is a severe restriction not met by most currently fabricated fibers and the resulting accuracy of ± 10 percent is also not sufficient for many applications. In addition, these methods cannot accommodate arbitrary perturbations of the profile which commonly exist in the form of barrier layers at the core-cladding interface and an index depression along the axis of the fiber.

These limitations have been overcome with a method of analysis in which profiles with arbitrary shapes can be handled.[9] In that analysis, the fiber core is modeled as having many layers, with each layer having a constant index of refraction. The profile is then built up in a stepwise manner using the index value from each preceding section as the starting point for the next. The resulting accuracy is on the order of a few percent.

That analysis, however, is based on having a certain minimum width for each layer and breaks down if smaller intervals are utilized. While this is not a serious limitation in practice, it may present problems if very rapid and narrow variations occur in the profile. We have therefore developed a new analysis scheme not having this potential drawback in which the profile is obtained by the solution of an integral equation which can handle small regions. However, this new method is still restricted to index profiles of rotational symmetry. We have also fully automated the measurement and analysis procedure so that its inherent rapid nature can be fully exploited. We call our nondestructive measuring procedure the "whole-fiber method."

This paper consists of two basic sections. In the first, the details of the solution of the integral equation and error estimates are treated.

In the second, the automated system is described and various profiles are presented, discussed, and compared with those obtained by other methods.

II. SOLUTION OF THE INTEGRAL EQUATION AND ERROR ESTIMATE

In the whole-fiber method, the ray traverses the fiber core at right angles to its axis.[8] The phase shift of each ray is an integral over the product of the length element of the ray path ds times the relative refractive index (relative with respect to the cladding index n_c). Ignoring ray bending in the core, we may express the relative phase shift according to Fig. 1 as

$$P(r) = \frac{4\pi}{\lambda} \int_r^\infty [n(\rho) - n_c] \frac{\rho d\rho}{\sqrt{\rho^2 - r^2}}. \tag{1}$$

The upper limit of the integral actually need only be $\rho = a$ but, because $n(\rho) = n_c$ for $\rho > a$, we may as well use the limit ∞. To obtain the relation between the fringe shift $S(r)$ and the relative phase shift P, we observe that the ratio of fringe shift to fringe spacing D must be equal to the ratio of the relative phase shift to 2π,

$$\frac{S(r)}{D} = \frac{P(r)}{2\pi}. \tag{2}$$

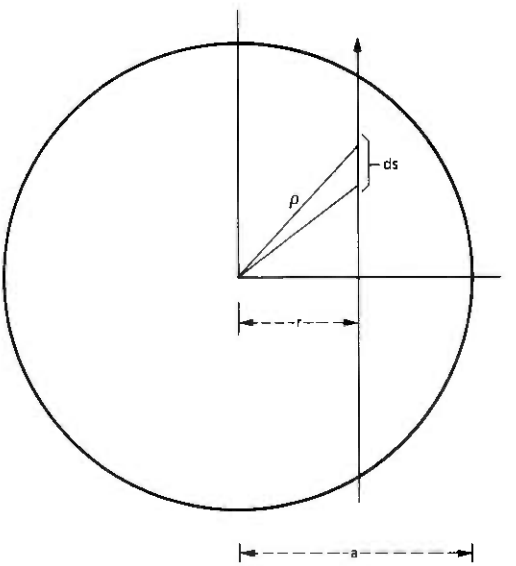

Fig. 1—Outline of fiber core and variables appearing in eq. (1).

Equations (1) and (2) thus lead to the following integral equation for $n(\rho) - n_c$:

$$\int_r^\infty [n(\rho) - n_c] \frac{\rho d\rho}{\sqrt{\rho^2 - r^2}} = \frac{\lambda}{2D} S(r). \tag{3}$$

We show in the appendix that the solution of this integral equation may be expressed as

$$\Delta n(r) = n(r) - n_c = -\frac{\lambda}{\pi D} \int_r^\infty \frac{dS(\rho)}{d\rho} \frac{d\rho}{\sqrt{\rho^2 - r^2}}. \tag{4}$$

This explicit solution of the integral equation (3) shows that the refractive index difference at any point r in the fiber core can be obtained from a knowledge of the fringe shift function $S(r)$ by differentiation and integration. Since the fringe shift is known only at certain discrete points, numerical techniques [see eq. (14)] for approximating the derivative as well as the integral must be used.* The accuracy of the resulting refractive index distribution depends on the accuracy of the measurement of $S(r)$, on the density of points at which $S(r)$ is being measured, and on the sophistication of the methods used for numerical evaluation.

The explicit solution (4) of the integral equation (3) is useful not only for obtaining numerical solutions for the refractive index profile but also for calculating estimates of the error of Δn that is introduced by the fact that the measured values of the fringe shift $S(r)$ are only known to a limited precision. We use the subscript o to indicate the index difference Δn_o that would be obtained if the fringe shift S_o and its derivative were known precisely. The variance of the refractive index difference is thus, according to (4),

$$\langle (\Delta n - \Delta n_o)^2 \rangle$$

$$= \left(\frac{\lambda}{\pi D}\right)^2 \int_r^\infty d\rho \int_r^\infty d\rho' \frac{\langle [\dot{S}(\rho) - \dot{S}_o(\rho)][\dot{S}(\rho') - \dot{S}_o(\rho')] \rangle}{\sqrt{(\rho^2 - r^2)(\rho'^2 - r^2)}}. \tag{5}$$

The derivative of S is indicated by the notation $\dot{S}$ and the symbol $\langle\ \rangle$ designates an ensemble average. The numerator under the integral sign in (5) is the autocorrelation function of the derivative of the fringe shift S. For simplicity, we assume that this function is of the following form:

* At and near $\rho = r$, an analytical approximation of (4) is used, based on a fourth-order polynomial expansion of $S(\rho)$.

$$R_d = <[\dot{S}(\rho) - \dot{S}_o(\rho)][\dot{S}(\rho') - \dot{S}_o(\rho')]>$$

$$= \begin{cases} (\Delta\dot{S})^2 & \text{for} \quad |\rho - \rho'| < B \\ 0 & \quad\quad\; |\rho - \rho'| > B. \end{cases} \tag{6}$$

The autocorrelation function is assumed to have a constant value, equal to the variance of the function $\dot{S}$, over a narrow region outside of which it vanishes. The interval B assumes the physical meaning of a correlation length. We consider B as a very short distance, much shorter than any of the transverse dimensions of the fiber. This assumption allows us to work out the following approximation for (5).

$$<(\Delta n - \Delta n_o)^2> = \left(\frac{\lambda}{\pi D}\right)^2 (\Delta\dot{S})^2 \frac{B}{r} \ln\left(\frac{2r}{B}\right). \tag{7}$$

Approximation (7) is valid only for $r \gg B$; however, if we try to evaluate (5) with the special function (6) directly at $r = 0$ we find an infinite result. This failure indicates that it is not permissible to use (6) for arbitrarily small values of ρ because the derivative of S, and hence its variance, must vanish at $\rho = 0$ because of the symmetry of the structure. Assuming $(\Delta\dot{S})^2$ to be constant is thus not permissible for arbitrarily small values of ρ.

The variance $(\Delta\dot{S})^2$ of the derivative of the fringe shift function S is not easy to visualize intuitively. For this reason, we must relate it to the variance $(\Delta S)^2$ of the fringe shift function itself. The autocorrelation function (6) for $\dot{S}$ and the autocorrelation function for S

$$R(u) = <[S(\rho) - S_o(\rho)][S(\rho + u) - S_o(\rho + u)]> \tag{8}$$

are related by the well-known equation[11]

$$R_d = -\frac{d^2R}{du^2}. \tag{9}$$

If we exclude the point $|u| = B$, and keep in mind that $R(u) = R(-u)$ is required, we conclude that if R_d has the form (6) R must have the functional form

$$R(u) = \begin{cases} (\Delta S)^2 \dfrac{B^2 - u^2}{B^2} & \text{for} \quad |u| < B \\ 0 & \text{for} \quad |u| > B. \end{cases} \tag{10}$$

Equations (6), (9), and (10) lead to the following relation between the variance $(\Delta\dot{S})^2$ of the derivative of the fringe shift function and the variance $(\Delta S)^2$ of the fringe shift function itself:

$$(\Delta\dot{S})^2 = \frac{2(\Delta S)^2}{B^2}. \tag{11}$$

Substituting (11) into the square root of (7) finally yields the following expression for the rms deviation of the refractive index difference:

$$\delta[\Delta n(r)] = \frac{\sqrt{2}\,\lambda\Delta S}{\pi D}\left[\frac{\ln\dfrac{2r}{B}}{rB}\right]^{1/2}, \tag{12}$$

with the definition

$$\delta(\Delta n) = [<(\Delta n - \Delta n_o)^2>]^{1/2}. \tag{13}$$

It remains to obtain an estimate for the correlation length B. We assume that the measured values of the fringe shift S at equidistantly spaced measuring points r_i are used to define a Lagrange interpolation polynomial

$$F = \sum_{i=1}^{n+1} \prod_{\substack{j=1 \\ \neq i}}^{n+1} \left(\frac{r - r_j}{r_i - r_j}\right) S_i, \tag{14}$$

where we used the abbreviation

$$S_i = S(r_i). \tag{15}$$

An interpolation polynomial of this type with $n = 4$ is actually used to evaluate the derivative $\dot{S}$ and the integral in (4). We assume that the differences of the measured values S_i and the true values $S_o(r_i)$ are mutually uncorrelated,

$$<(\Delta S_i)(\Delta S_j)> = (\Delta S_i)^2\delta_{ij}, \tag{16}$$

where, by definition,

$$\Delta S_i = S_i - S_o(r_i). \tag{17}$$

We use $n + 1$ adjacent points r_i to define F according to (14) and extend this function outside this range by defining a new function with the help of the next set of $n + 1$ adjacent points, etc. Using

$$R_F(u) = <\Delta F(r)\Delta F(r + u)>, \tag{18}$$

where ΔF is defined in analogy with (17),

$$\Delta F = F(r) - F_o(r), \tag{19}$$

we have computed the function (18) numerically by using (14) and (16). Figures 2 through 5 show the results of these computations for a few points $r = 1$, 1.5, 2, and 2.5 for a fourth-order polynomial approximation using points $r_1 = 1$ through $r_5 = 5$ and extend this function by corresponding polynomials outside of this range. The endpoints of one range are simultaneously also endpoints of the polynomial expansions in adjacent ranges. It is apparent that the autocorrelation function is neither stationary nor symmetric because it depends on the choice of

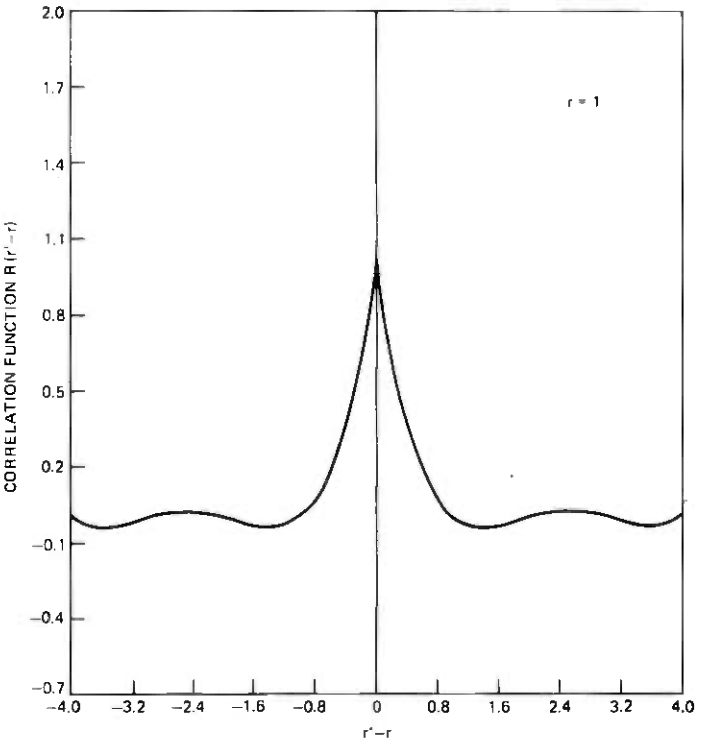

Fig. 2—Correlation function $R(r' - r)$ associated with a fourth-order interpolation polynomial if the functional values at the five points used to define the interpolation polynomial are mutually uncorrelated. The distance between adjacent interpolation points is used as the unit of length. In this figure, the autocorrelation function is evaluated with $r = 1$ being the end point of adjacent interpolation intervals. Adjacent intervals (of 5 points each) are approximated by similar interpolation polynomials. Note that, for this choice of r, the function assumes a symmetrical appearance.

r in (18). On the other hand, we may use this approach to gain an order-of-magnitude estimate of the correlation length B. Figure 6 shows an average of the autocorrelation functions averaged over r. This function is very nearly of the form $(\sin x)/x$ and, in its central portion, is a reasonable order-of-magnitude approximation of the correlation function (10). It is clear from this averaged autocorrelation function that the correlation length B is on the order of the length of the interval used for defining the individual interpolation function,

$$B = n\Delta r, \tag{20}$$

where Δr indicates the distance between adjacent sampling points

$$\Delta r = r_{i+1} - r_i. \tag{21}$$

Even though our error analysis can claim to give no more than an order-of-magnitude estimate, (12) and (20) show that the error due to

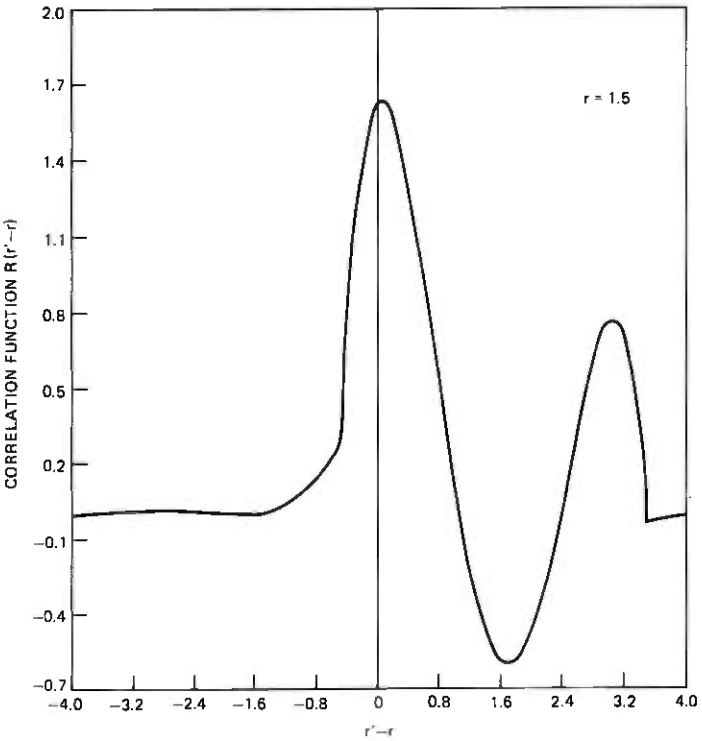

Fig. 3—Similar to Fig. 2 with $r = 1.5$. The autocorrelation function is now not symmetrical around the point $r' - r = 0$.

the limited accuracy of the measurements of the fringe shift $S(r)$ increases as r decreases and also that the error of the refractive index determination increases as the length of the interval Δr between adjacent sampling points decreases. This latter error can be decreased by using an interpolation polynomial of higher order. All these trends have been clearly observed in our experimental results.

To gain insight into the numerical values of the rms deviation $\delta(\Delta n)$, let us make the following assumptions. The distance between adjacent scan lines of the vidicon corresponds to 0.2 μm of the vertical direction along the fiber core. Because of an averaging procedure using 10 adjacent scan lines for finding the center of each fringe, we may assume $\Delta S = 0.2/10 = 0.02$ μm. The distance between adjacent sampling points in horizontal direction is typically $\Delta r = 1$ μm. We set $n = 4$ because of our use of a fourth-order interpolation polynomial. The fringe spacing is typically $D = 6$ μm. If we use $\lambda = 1$ μm and use a value halfway between core center and core boundary, $r = 15$ μm, we find, from (12),

$$\delta(\Delta n) = 3 \times 10^{-4}. \tag{22}$$

This amount of rms deviation is in excellent agreement with the

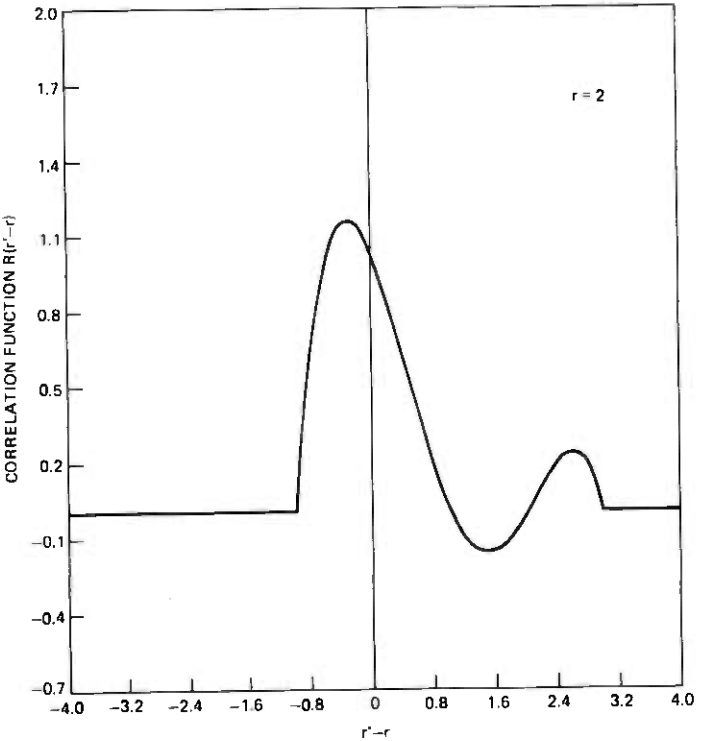

Fig. 4—Similar to Figs. 2 and 3 with $r = 2$.

observed values. However, it is important to remind the reader that this is the error caused by the random uncertainty in the fringe position that is inherent in the measuring process. It is not the absolute error relative to the (unknown) precise value of Δn. Our derivation of the error estimate (12) is limited to the random component of the uncertainty of the fringe shift S and does not include systematic errors arising from distortions in the imaging process of the microscope or the vidicon and furthermore does not include the systematic error arising from the process of using a finite number of discrete points for evaluating the derivative $\dot{S}$ and the integral in (4). Only the additional error caused by the uncertainty about the actual values of $S(r_i)$ at the sampling points is responsible for the rms deviation of Δn expressed by (12). Systematic errors existing in the system have been investigated, however, and were found to be at least one order of magnitude less than this value.

III. AUTOMATIC PROCESSING AND ANALYSIS SYSTEM

The experimental arrangement to automatically measure and analyze the profiles of whole fibers is shown in Fig. 7. The use of this

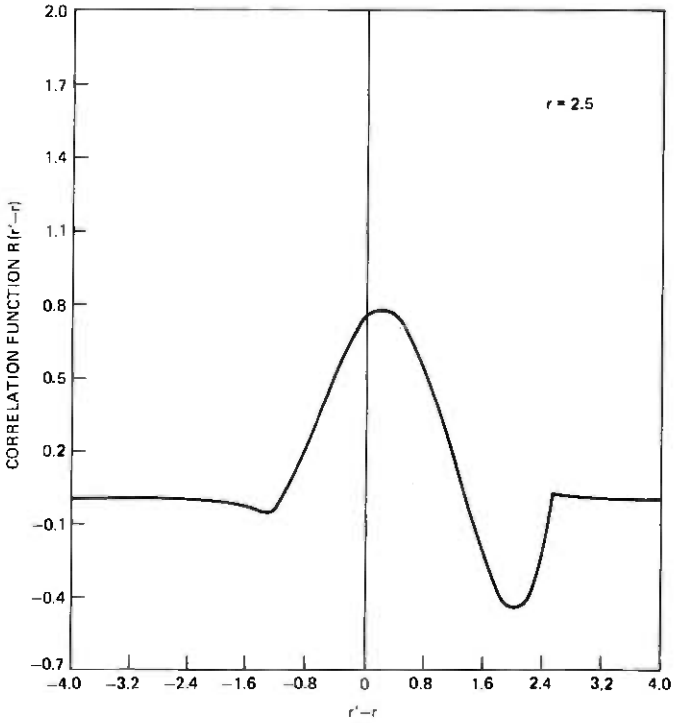

Fig. 5—Similar to Figs. 2 and 3 with $r = 2.5$.

system has been briefly described elsewhere.[9] Here, we discuss the full details of its operation.

The basis of the system is a Leitz dual-beam, single-pass transmission interference microscope which is generally used to perform precise refractive index profiling of optical fibers by examining polished slab samples.[1-6] For the whole-fiber measurements, a short length of fiber (~1 cm) is inserted into index-matching oil in the sample arm of the microscope and a similar thickness of oil is placed in the reference beam. An excellent match to the cladding could be achieved at an observation wavelength $\lambda = 0.9$ μm with matching oil of index $n_D = 1.457 \pm 0.0005$ with no temperature control.

The output field of the microscope is detected with an infrared-enhanced, silicon-target vidicon, and the video signal is sent to a video digitizer that has the capability of addressing discrete picture elements in the television frame and digitally encoding the intensity at each element. The digitizer resolves 480 picture elements along the Y axis and 512 elements on the X axis. The X- and Y-position data inputs are provided by the 16-bit duplex input/output (I/O) interfaces of a

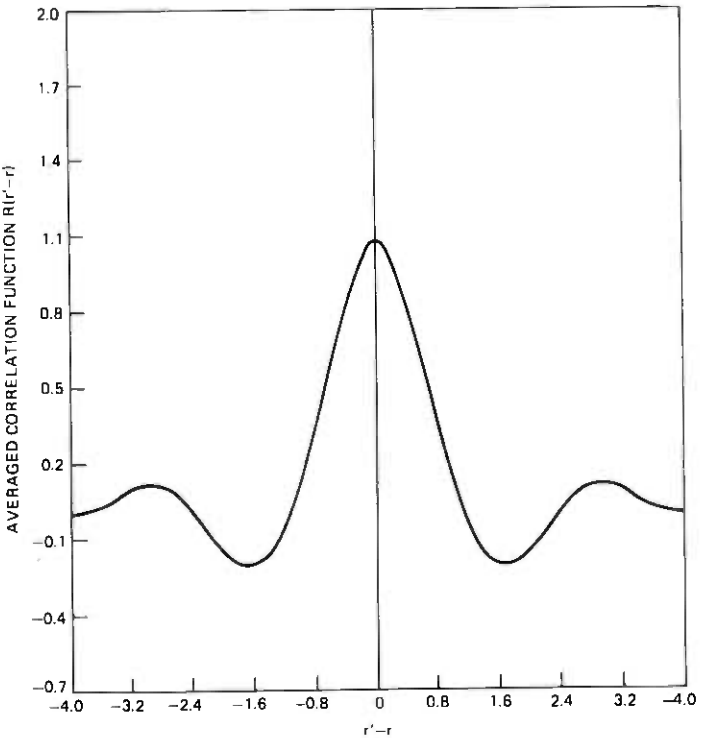

Fig. 6—Averaged autocorrelation function. The average is taken over r in the interval $1 \leq r \leq 5$.

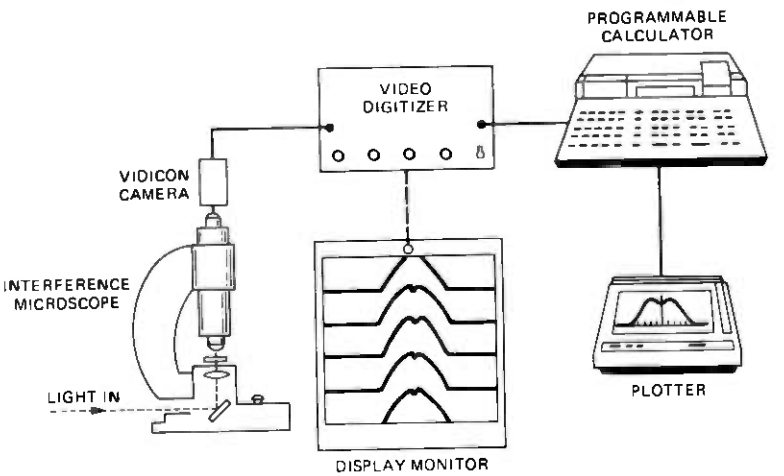

Fig. 7—Experimental arrangement to perform automatic index profiling of whole fibers.

Hewlett Packard 9825A computer with the least significant bit of the Y address serving as the field selector.

The digitizer normally operates by deriving horizontal (line) and vertical (field) timing from the video input signal and uses these timing signals to keep track of the position of the video signal relative to the TV raster at any instant. This location is compared with the selected X, Y sample point and, when coincidence is achieved, the video at that point is digitally encoded to 8 bits or 256 gray levels and sent to the computer which then issues new X, Y coordinates and the procedure is repeated. We have found, however, that the transition of the computer between issuing new data (writing-mode) and receiving the digitized information (reading-mode) is sufficiently long (~3 ms) that it does not allow for the digitization of all Y values for a given X coordinate (one column) within one field, 1/60 s. To do this requires an execution time of 50 μs or less. In fact, only one point per field can be processed, and digitizing a single column typically takes about 3 s. This is not normally a serious limitation since only on the order of 50 columns (requiring 2½ minutes) are needed to measure the profile with good resolution. However, if it is desired to obtain maximum sensitivity by averaging over many scans to reduce video noise levels, this limitation becomes prohibitive.

The computer, on the other hand, is capable of reading 400,000 words of data per second and if it could be freed of the need to supply consecutive Y addresses, digitization of a column could be accomplished in 1/60 s (for each field), saving a factor of almost 200 in time.

This has been achieved with the addition of the interface board shown schematically in Fig. 8, which essentially contains an 8-bit programmable counter and support logic gates. At the start of each columnar digitization, the computer loads the counter with the logic value of the number of points desired and issues the initial X value. These readings are then taken, and a stop pulse is issued. An enable pulse whose length is related to the number of data points is also generated by the circuitry to supply handshaking (timing) for the system and to allow the region being processed to be observed on a display monitor.

A photograph of the display showing a typical graded-index fiber observed at a wavelength of $\lambda = 0.9$ μm is seen in Fig. 9. Location of the point being encoded is indicated by a dot cursor and the gray scale value for all Y elements along a sample line at the selected X position is displayed as a waveform at the side of the monitor screen. The two vertical lines bounding the waveform display indicate the black and white reference levels which are encoded as 255 and 0, respectively.

The sequence of events for determining the fringe shift as a function of radius, $S(r)$, from which the profile is computed, shall be described with reference to Fig. 9. It is first necessary to choose a desired fringe.

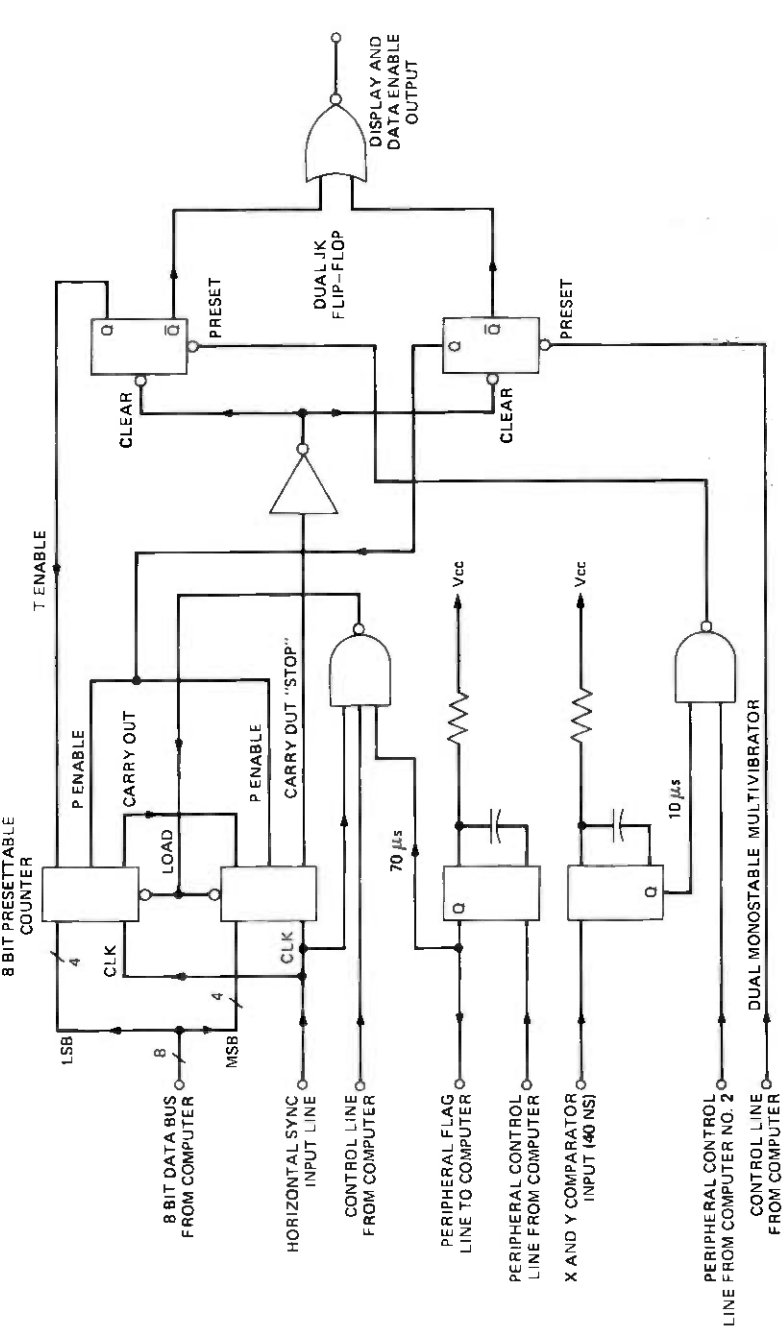

Fig. 8—Video-digitizer interface board to allow data accumulation for each field within one frame time.

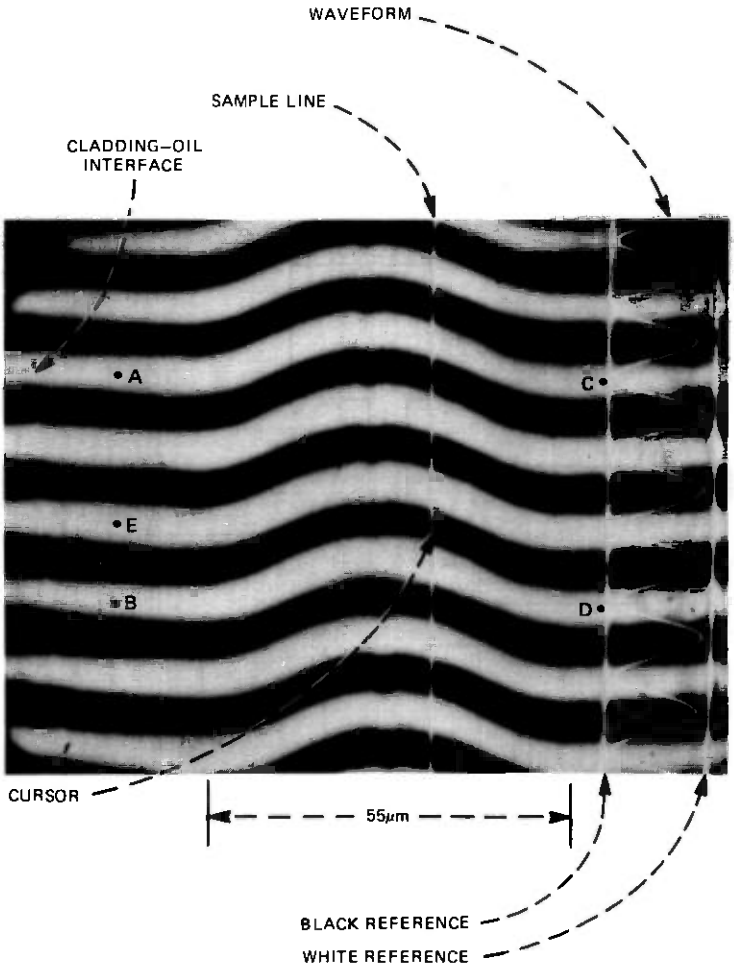

Fig. 9—Display of video monitor showing transversely illuminated whole fiber at a wavelength of 0.9 μm.

This generally is not critical since any fringe should give the same index distribution assuming that the profile is constant along the fiber and the sample is relatively clean and free of surface imperfections. Once selected, the fringe is located by a procedure of fringe counting. For example, starting from point A and proceeding along a line AB, let the desired fringe number be 3. Thus all elements along line AB defined by a fixed X value are digitized. The computer then counts the fringes to find the third one. In this procedure, a fringe is defined by following the digitized data and noting transitions in gray-scale values by more than some fixed number. Twenty data points in the vicinity of the fringe maxima are chosen, and a parabolic fit to them is formed.

The maximum of the curve thus determined is taken as the center of the fringe. The computer also determines at this time the uniform spacing, D, of the fringes in the cladding by locating the center of each fringe and averaging over the number of fringes.

The X position value is then changed and the same determination is made for the right-hand side of the cladding along line CD. A straight line is fitted by the computer to pass through the centers of the third fringe at these right- and left-hand sides. This line serves as the reference level from which fringe displacements are made and also compensates for possible misalignment of the fringes to the scanning line axis.

Next, the X position is automatically set to point E which is about midway between fringe 3 and 4, and scanning proceeds from E to B. X is then incremented for each such columnar encoding and the Y address is automatically corrected to track the fringe by picking midway initial X values as was done for point E.

To enable the calculation of the radius, the XY coordinates of the fiber's axis are located as part of an initial set-up procedure. This is readily achievable due to the index depression which exists along the axis[10] and causes a perceptible dip in the fringes. The initial set-up procedure also includes entering into the computer the coordinates of points A, B, and C, the wavelength of observation, the desired X increment, and the desired fringe number. The computer then takes over and at the end of the encoding process calculates Δn as a function of radius for each half of the core, averages both halves, and plots the resulting index profile along with coordinates and labeling on an XY plotter.

A best-fit power-law (α) curve to the index profile may be determined after the coordinates of the limits over which the fit is to be made are entered. In addition to the α parameter, this fitting procedure also determines the core radius, the shift of the center of the core, the maximum index difference between core and cladding, and a fitting error to provide a measure of how well the α curve approximates the measured profile. These values are then printed out and the best-fit α curve is drawn on the plotter.

Four examples of measured profiles for various GeO_2-doped fibers demonstrating the general applicability of this method are shown in Figs. 10 to 13.

Figures 10 and 11 show typical and reasonably smooth profiles (solid line) which are fit with relatively good α curves (broken lines), the fitting errors being on the order of 1 percent. Perturbations in the profile, mainly in the form of the index depression along the axis and variations in deposition layers close to the center, are clearly resolved. It is important to emphasize that this method assumes circular symmetry for the fiber core and thus variations in core geometry, if

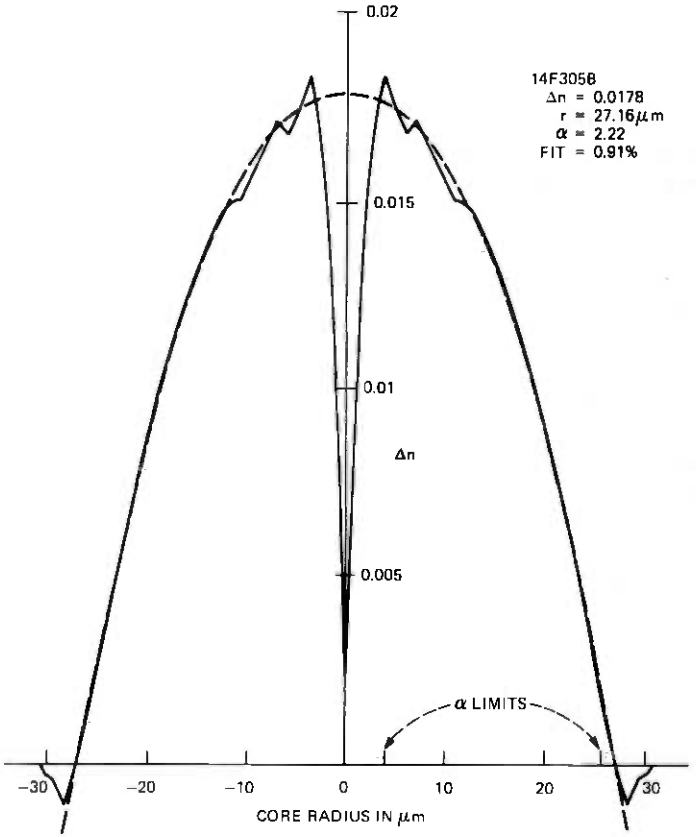

Fig. 10—Profile of typical GeO_2-doped fiber (solid curve) and best-fit α curve (broken curve).

existing, would not be detected. The variations in the plotted profile also represent averages over both sides of the core.

Figure 12 shows the profile of a fiber with strong index variations in the vicinity of the axis, and Fig. 13 shows a fiber with a very large boron barrier layer at the core-cladding interface. These unique features are clearly detectable and well resolved, thus demonstrating the applicability of this technique to even these extreme cases.

We have compared profiles obtained using the circular index analysis technique of Ref. 8, in which the profile is built up piecewise, with the integral equation approach used here. The agreement was excellent with the profiles being essentially identical.

The profiles have also been compared with those obtained by preparing polished slabs of the same fiber samples. The comparison results, presented in detail in Ref. 8, show very good agreement with the average difference of the maximum Δn values and the α values being about 4 percent.

The experimental accuracy of the measured profiles and the effects of index mismatching were investigated by measurements made on unclad fiber (uniform-index) samples under various matched and unmatched conditions. Variations of the index were consistently found to be within about 2 parts in 10^4, in excellent agreement with the theoretical analysis of the previous section. For unclad fibers with intentional index mismatch, we obtained step index profiles with the height of the step corresponding to the degree of mismatch. When a good match is visually observed on the monitor, as evidenced by a straight fringe parallel to the scanning line axis, the error in the profile due to mismatch was found to be on the same order as that due to the index variations (a few parts in 10^4); thus, no attempt at more precise matching was made.

In conclusion, the techniques described to measure the refractive index profiles of optical fibers rapidly and automatically should prove

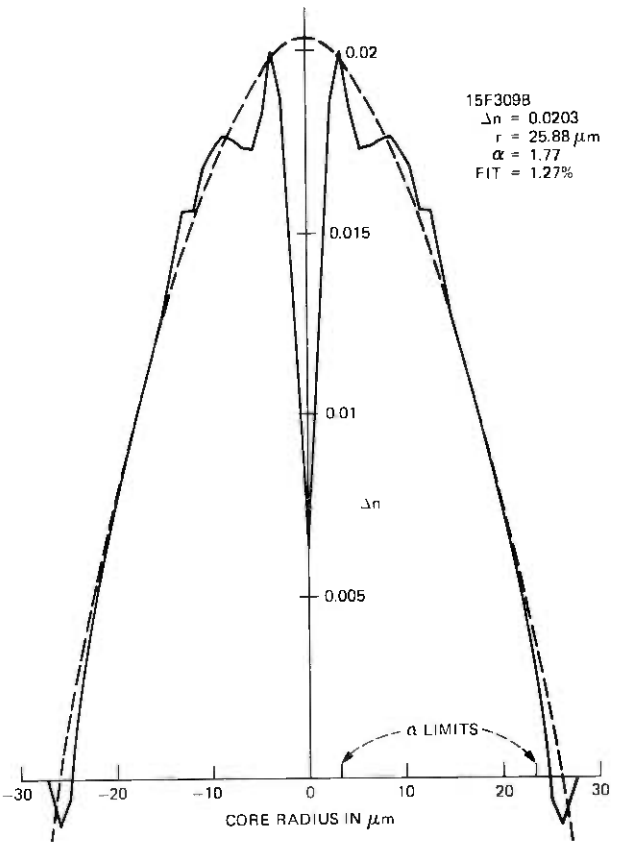

Fig. 11—Profile of GeO_2-doped fiber (solid curve) and best-fit α curve (broken curve) showing somewhat greater variations than fiber of Fig. 10.

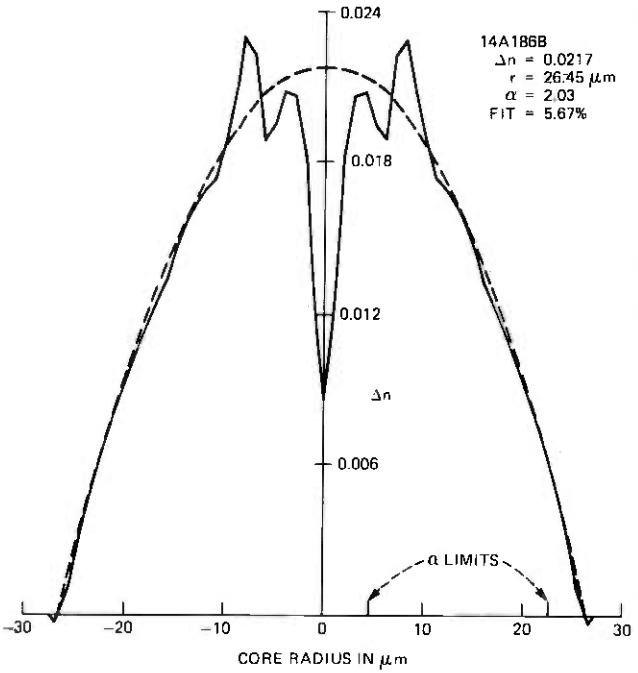

Fig. 12—Profile of GeO_2-doped fiber (solid curve) and best-fit α curve (broken curve) showing strong central index perturbations.

valuable not only in reducing the time required for these measurements but also in forming the basis of an evaluation scheme in which fibers can be rated and selected for specific applications, depending upon the quality of their profiles, almost immediately upon production.

APPENDIX

We sketch the solution of the integral equation (3), which we write in the form

$$\int_y^\infty \frac{xf(x)\,dx}{y\sqrt{(x^2-y^2)}} = g(y). \tag{23}$$

In our application, $f(x)$ is an even function of x; this allows us to express it in the form

$$f(x) = \int_o^\infty F(u)\cos(ux)\,du. \tag{24}$$

Substitution of (24) into (23) yields after integration

$$-\frac{\pi}{2}\int_0^\infty F(u)J_1(uy)\,du = \frac{1}{y}\,g(y), \tag{25}$$

where J_1 is the Bessel function of order one. This integral relation is the Hankel transform whose inversion is given by the formula

$$F(u) = -\frac{2}{\pi}\,u\int_0^\infty g(y)J_1(uy)\,dy. \tag{26}$$

Substitution in (24) yields

$$f(x) = -\frac{2}{\pi}\int_0^\infty g(y)\left\{\int_0^\infty u\cos(ux)J_1(uy)\,du\right\}dy. \tag{27}$$

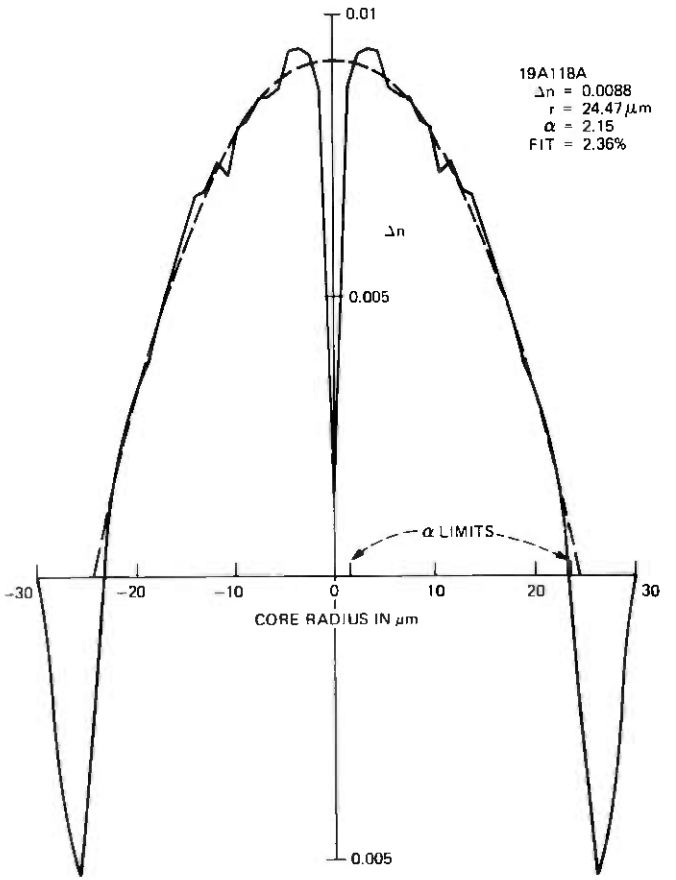

Fig. 13—Profile of GeO_2-doped fiber (solid curve) and best-fit α curve (broken curve) showing resolution of large boron barrier layer.

This expression can also be written in the form:

$$f(x) = \frac{2}{\pi} \int_o^\infty g(y) \left\{ \frac{d}{dy} \int_o^\infty \cos(ux) J_0(uy)\, du \right\} dy. \tag{28}$$

We perform a partial integration

$$f(x)$$

$$= -\frac{2}{\pi} \left\{ g(0) \int_o^\infty \cos(ux)\, du + \int_o^\infty \frac{dg}{dy} \int_o^\infty \cos(ux) J_0(uy)\, du\, dy \right\}, \tag{29}$$

where we used the fact that the fringe shift vanishes outside the fiber core so that $g(\infty) = 0$. The integral over the cosine function vanishes for $x \neq 0$. The integral over the product of the cosine and Bessel functions can be found in tables so that we finally obtain

$$f(x) = -\frac{2}{\pi} \int_x^\infty \frac{dg}{dy} \frac{dy}{\sqrt{y^2 - x^2}}. \tag{30}$$

The integral transform pair (23) and (30) corresponds to the transform pair (3) and (4).

REFERENCES

1. C. A. Burrus and R. D. Standley, "Viewing Refractive-Index Profiles and Small-Scale Inhomogeneities in Glass Optical Fibers: Some Techniques," Appl. Opt., *13* (1974), p. 2365.
2. H. M. Presby, W. Mammel, and R. M. Derosier, "Refractive Index Profiling of Graded Index Optical Fibers," Rev. Sci. Instrum., *47* (1976), p. 348.
3. H. M. Presby and I. P. Kaminow, "Binary Silica Optical Fibers: Refractive Index and Profile Dispersion Measurements," Appl. Opt., *15* (1976), p. 3029.
4. H. M. Presby and H. W. Astle, "Optical Fiber Index Profiling by Video Analysis of Interference Fringes," Rev. Sci. Instr., *49* (1978), p. 339.
5. H. M. Presby, D. Marcuse, and H. W. Astle, "Automatic Refractive Index Profiling of Optical Fibers," Appl. Opt., *17* (1978), p. 2209.
6. B. C. Wonsiewicz, W. G. French, P. O. Lazay, and J. R. Simpson, "Automatic Analysis of Interferograms: Optical Waveguide Refractive Index Profiles," Appl. Opt., *15* (1976), p. 1048.
7. M. E. Marhic, P. S. Ho, and M. Epstein, "Nondestructive Refractive-Index Profile Measurement of Clad Optical Fibers," Appl. Phys. Lett., *26* (1975), p. 574.
8. M. J. Saunders and W. B. Gardner, "Nondestructive Interferometric Measurement of the Delta and Alpha of Clad Optical Fibers," Appl. Opt., *16* (1977), p. 2368.
9. L. M. Boggs, H. M. Presby and D. Marcuse, "Rapid Automatic Index Profiling of Whole Fiber Samples: Part I," B.S.T.J., this issue, pp. 867–882.
10. H. M. Presby, "Axial Refractive Index Depression in Preforms and Fibers," Fiber and Integrated Optics, 2(No. 2).
11. A. M. Yaglom, *An Introduction to the Theory of Stationary Random Functions*, New York: Dover, 1962, p. 23.

THE BELL SYSTEM TECHNICAL JOURNAL
Vol. 58, No. 4, April 1979
Printed in U.S.A.

Acoustic Filters to Aid Digital Voice*

By J. L. FLANAGAN

(Manuscript received September 19, 1978)

Digital conversion of speech requires that the signal be band-limited. The band limitation customarily is accomplished by electrical filtering. Typically, the cost of electrical filtering is a noticeable fraction of the total cost of voice digitization. We propose here that a large part, if not all, of the requisite filtering can be economically accomplished through acoustic design of the transducer housing (both at transmitter and receiver). We derive a design technique for voice-band acoustic filters, and we compute and construct several prototype filters. We make free-space acoustic measurements on the prototypes, used in combination with electret microphones. Finally, we demonstrate that the acoustic filters can approximate the band-limit specifications for the D-channel bank.

I. DIGITAL CONVERSION OF ACOUSTIC SIGNALS

The well-known sampling theorem prescribes that a signal can be exactly recovered from its time-discrete samples provided the samples are taken at least as frequently as twice the rate of the highest frequency component present in the signal. Band limitation of signals is therefore fundamental to distortion-free digital representation. The same band limitation is necessary to recover the continuous signal from its time-discrete samples. High quality analog-to-digital (A/D) and digital-to-analog (D/A) conversions consequently depend upon band limitation sufficient to suppress spectral aliasing.

Electrical filters typically are used to provide the requisite band limitation. Traditionally, these have been analog implementations, but new advances in integrated circuitry permit implementation through high-rate sampling, digital filtering, and decimation. Still, at the initial and final analog levels, the signal must be analog band-limited, and

* An abridged report of this work was presented to the 96th meeting of the Acoustical Society of America, J. Acoust. Soc. Am., *64* (November 1978), p. S55.

the total band limitation must be accomplished sufficiently well to suppress aliasing.

To illustrate a typical need for band-limiting, recall that in T-carrier digitization of voice signals the signal bandwidth is limited to less than 4 kHz and the sampling rate is 8 kHz. In terms of this requirement, most of our telephone transmitters (microphones) are too good. Figure 1 shows approximate frequency responses for the Western Electric T-1 carbon button and the EL-2 electret.[1,2] These microphones have high-frequency responses that extend much above 4 kHz, and the rate of attenuation above this point is typically shallow, about 12 dB/oct. Overt low-pass filtering, to approximately the sixth order, is necessary to restrict the transduced signal to a bandwidth suitable for sampling at 8 kHz. This band-limiting is typically done by electrical filtering.

As the cost of integrated digital converters (A/D and D/A) continues to diminish, the cost of electrical filtering, especially analog, becomes a significant part of the expense of digital conversion.[1] This issue is particularly important in systems where digitization must be performed on a dedicated per-channel basis. Typical instances include digital mobile radio telephone and digital subscriber loop systems, where voice digitization is accomplished at, or close to, the station set. In these cases, there is considerable incentive to reduce the cost of signal filtering and digitization. In other cases, where group digitization and multiplexing at a central location are done, the per-channel costs are less dominant. Also, if digitization is performed at a central location following an analog transmission of significant distance, additional filtering may be needed to control accumulated electrical noise.

II. ACOUSTIC BAND-LIMITING FILTERS

One possibility for gaining cost advantages is to make the acoustic transducer do some, or preferably all, the signal filtering—both for sampling (at the transmitter) and desampling (at the receiver). To

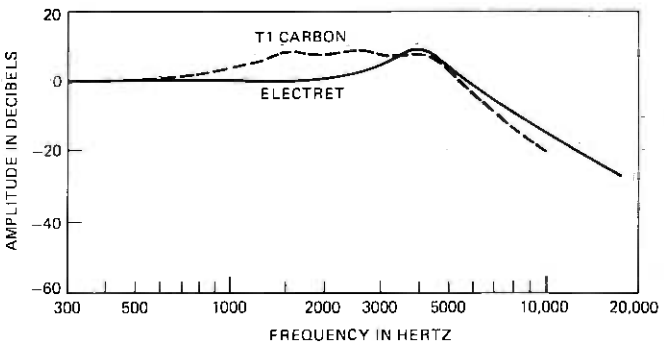

Fig. 1—Approximate frequency responses for the T1 carbon and EL-2 electret microphones.

incorporate this filtering as part of the internal mechanics of a microphone or earphone is not so attractive because it reduces the versatility of these transducers for a variety of applications in voice communications. But to install the broadband transducer in an acoustic housing that could implement the band filtering and that might easily be injection-molded (say, as part of the transmitter cap in the handset) or stamped out (as part of the transducer case) is attractive, both functionally and economically.

This report, therefore, sets forth a design technique for producing simple acoustic filters for voice transmission. The acoustic filters can be appliquéd onto typical telephone transducers and can provide low-pass band-limiting which closely approximates the D-channel bank requirements for voice digitization.

In this report we discuss transmitter (microphone) filters only, but similar principles apply for desampling filters at the receiver (earphone or loudspeaker).

III. SOME ACOUSTIC THEORY RELEVANT TO FILTER DESIGN

It is convenient to focus our discussion on acoustic analyses that can be formulated primarily in terms of one-dimensional sound propagation. That is, to keep the discussion simple, we will not make detailed treatment of cross-modes.* With this in mind, recall that the spatial and temporal variations of sound pressure, $p(x, t)$, and volume velocity, $U(x, t)$, for lossless, one-dimensional sound propagation in a rigid, uniform conduit of cross-sectional area A are described by

$$\frac{\partial p}{\partial x} = -\frac{\rho}{A}\frac{\partial U}{\partial t},$$

$$\frac{\partial p}{\partial t} = -\frac{\rho c^2}{A}\frac{\partial U}{\partial x}, \tag{1}$$

where ρ is the density of the medium (air in our case), and c is the sound velocity.† Eliminating either dependent variable produces the customary wave equation

$$\frac{\partial^2 \xi}{\partial x^2} = \frac{1}{c^2} = \frac{1}{c^2}\frac{\partial^2 \xi}{\partial t^2}, \tag{2}$$

* We shall see shortly that we cannot always escape this complexity.

† Typically,

$$\rho = 1.21 \times 10^{-3}\ \text{gm/cm}^3$$

$$c = 3.40 \times 10^{4}\ \text{cm/s}.$$

Further, the shape of the cross section A is unimportant for the lossless case.

which is satisfied both for $\xi = p$ and $\xi = U$.

Sinusoidal time dependence is represented by $\xi(x, t) = \xi(x)e^{j\omega t}$, where ω is the radian frequency. The spatial dependence is then described by the total derivatives

$$\frac{dp}{dx} = -\left(j\omega \frac{\rho}{A}\right)U = -z\,U,$$

$$\frac{dU}{dx} = -\left(j\omega \frac{A}{\rho c^2}\right)p = -y\,p,$$

and

$$\frac{d^2\xi}{dx^2} = -\left(\frac{\omega^2}{c^2}\right)\xi = zy\,\xi. \tag{3}$$

It is not accidental that these look like equations for an electrical transmission line, where p is analogous to voltage and U analogous to current. Though we have written down the conditions for no loss, z and y generally are complex quantities, and represent, respectively, the per-unit-length acoustic impedance and admittance of the rigid conduit, exactly analogous to the electrical line. The one-dimensional wave motion must be composed of progressive waves in $+x$ and $-x$ direction and must satisfy

$$\xi(x) = (\xi_+ e^{-\gamma x} + \xi_- e^{\gamma x}), \tag{4}$$

where $\gamma = \sqrt{zy} = (\alpha + j\beta)$ is the complex propagation constant, and ξ_+ and ξ_- are integration constants determined by boundary conditions. This leads immediately to the result we wish to make use of here.

For a length of conduit, l, eq. (4) permits relating the pressures and volume velocities at each end, namely,

$$p_2 = p_1 \cosh \gamma l - (U_1 Z_0)\sinh \gamma l$$

$$U_2 = U_1 \cosh \gamma l - (p_1/Z_0)\sinh \gamma l, \tag{5}$$

where the characteristic impedance $Z_0 = \sqrt{z/y}$. This is equivalent to the 4-pole network representation in Fig. 2b, where the series and shunt elements are, respectively,

$$z_a = Z_0 \tanh \gamma l/2$$

$$z_b = Z_0 \operatorname{csch} \gamma l. \tag{6}$$

This form will be convenient for the calculations we wish to make. Note one thing further about small values of the length dimension. The series expansions

$$\tanh x = x - \frac{x^3}{3} + \frac{2x^5}{15} \cdots$$

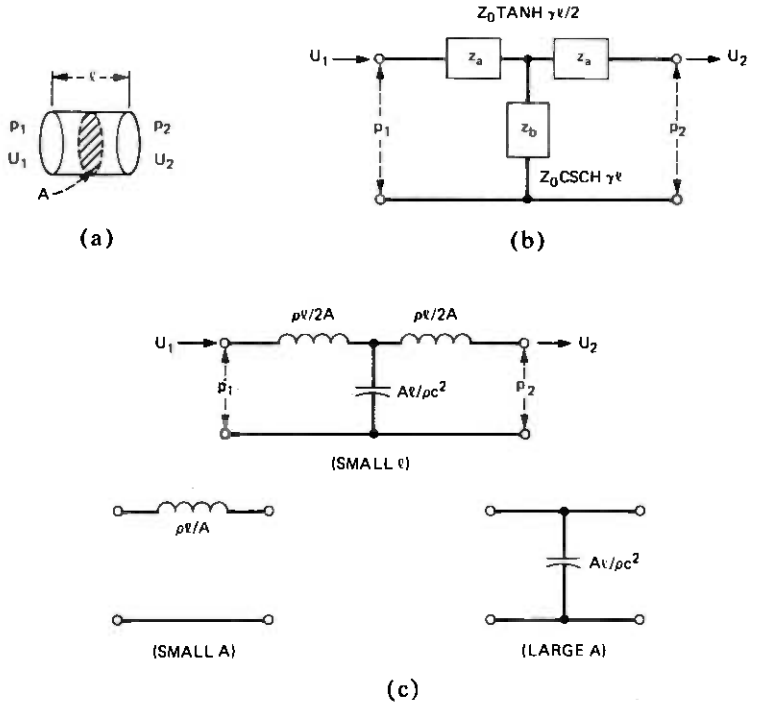

Fig. 2—Lumped constant representation of plane-wave propagation in a length l of right-circular conduit.

$$\sinh x = x + \frac{x^3}{3!} + \frac{x^5}{5!} \cdots \tag{7}$$

show that, for $\gamma l \ll 1$, the transcendental quantities can be approximated by lumped elements

$$z_a \cong (zl/2)$$

$$z_b \cong 1/(yl). \tag{8}$$

Except for radiation impedances, which typically are small, and for some small-dimension viscous effects, this is all we need to commence a filter design. We specify, without further explanation, appropriate values for the complex per-unit-length acoustic impedance and admittance, namely,

$$z = (R + j\omega L)$$

$$y = (G + j\omega C),$$

where

$$R = (S/A^2)\left(\frac{\omega\rho\mu}{2}\right)^{1/2}$$

$$L = \rho/A$$

$$G = S\left(\frac{\eta - 1}{\rho c^2}\right)\left(\frac{\lambda\omega}{2c_p\rho}\right)^{1/2}$$

$$C = A/\rho c^2, \tag{9}$$

and where S is the inner circumference of the conduit, μ the viscosity coefficient, λ the coefficient of heat conduction, η the adiabatic constant, and c_p the specific heat at constant pressure (all for the filling medium).[3,4] As the relations (9) suggest, the loss R is associated primarily with viscous loss and the conductance G is associated primarily with heat conduction loss, both at the conduit walls. Also, for the lossless case, the lumped approximation (8) gives

$$z_a = \frac{\rho l}{2A}$$

$$z_b = \frac{Al}{\rho c^2}, \tag{10}$$

as shown in Fig. 2c.

It is clear from the relations (6) and (8) that a simple, effective low-pass filter might be fabricated from a sequence of constrictions and reservoirs, as represented in Fig. 3a. Here the cross-sectional area is alternately small and large. To a first approximation, for dimensions small compared with a wavelength, the relations (10) show this structure to be roughly equivalent to the inductance-capacitance (LC) ladder network depicted in Fig. 3b. The design of automobile exhaust mufflers is a simple application of this fundamental notion.

The structure of Fig. 3a can be made more compact by shrinking the length of the small-area inertive (inductive) sections. In the limit $l_L \to 0$, and the inductor becomes a thin perforated baffle, as shown in Fig. 3c. In this case the inertance of the air in the aperture is conditioned primarily by the radiation reactance of the air load on A_L. Also, the resistive component of this radiation impedance, and viscous effects at small dimensions, dominate the loss characteristics. To examine this behavior, we need to look at the radiation impedance for a circular piston in a baffle.

A piston of radius, a, in a plane baffle, radiating into free space, has a radiation impedance approximated by

$$z_p = \frac{\rho c}{\pi a^2}\left[\frac{(ka)^2}{2} + j\frac{8(ka)}{3\pi}\right], \qquad ka \ll 1, \tag{11}$$

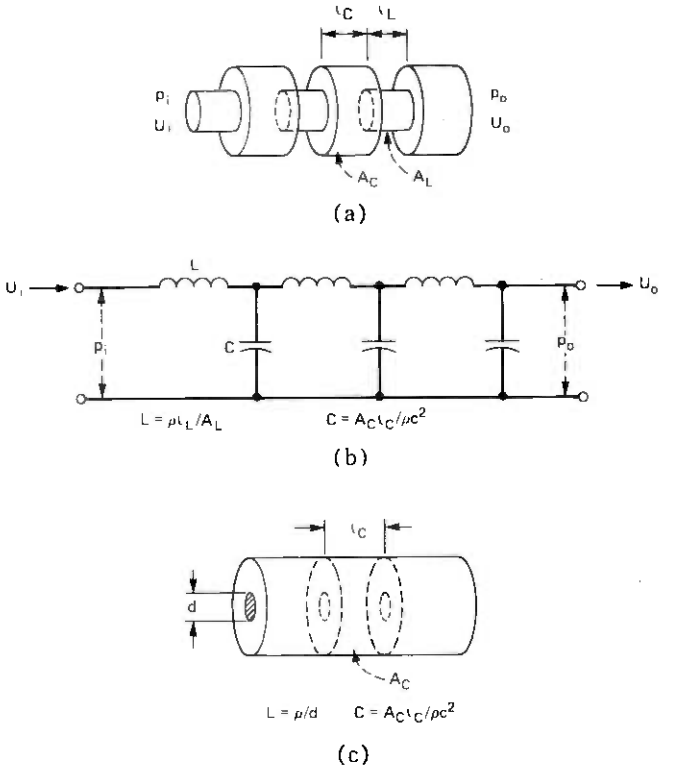

Fig. 3—Acoustic filter composed of alternate constrictions and reservoirs.

where $k = \omega/c$. One sees that the air load on one side of the piston is equivalent to an inertance of

$$\frac{L_a}{2} = \frac{8\rho}{3\pi^2 a} = 0.27\ \rho/a. \tag{12}$$

And for two sides radiating (as the perforation in a thin baffle would do into the adjacent cavities), the reactive load is equivalent to an inertance of

$$L_a = 0.54\ \rho/a.^* \tag{13}$$

This approximation to the inertance of a thin circular constriction is traditionally represented in the literature as

$$L_a \cong \rho/2a = \rho/d.^\dagger \tag{14}$$

---

* Note this implies an equivalent length of the thin constriction $\rho\ell_e/A = 0.54\ \rho/a$, or $\ell_e = 1.7a$.

† For a vanishingly thin plane baffle of infinite extent.

The viscous loss associated with the aperture can be crudely approximated by the per-unit-length resistance R, given in (9), multiplied by the thickness h of the baffle. A somewhat better empirical approximation to this loss is given by Morse and Ingard[3] as

$$R_a = \frac{1}{4\pi a^2}\sqrt{2\rho\omega\mu}\,\ln\left(\frac{2a}{h}\right). \tag{15}$$

One sees that this loss is relatively small for most dimensions of interest (for example, for $a = 7$ mm and $h = 1$ mm, $R_a < 0.1$ cgs acoustic ohms). Because of this, the damping usually desired in a filter design must be obtained from added loss, such as silk screen or cloth (which typically has a resistance on the order of 3 to 6 cgs ohms for an area of 1 cm^2).

Let us summarize, then, the several relations that subsequently will be useful for designing some acoustic filters.

Lumped inertance of a circular aperture of radius a:	$L_a = \rho/2a$
Distributed T-section impedances for a length l of uniform conduit of cross-sectional area A:	$z_a = Z_0 \tanh \gamma l/2$ $z_b = Z_0 \operatorname{csch} \gamma l$
Lumped inertance and compliance for a length l of uniform conduit of cross-sectional area A:	$L_a = \rho l/A$ (small A) $C_a = Al/\rho c^2$ (large A).

(16)

These few simple facts, together with estimates of acoustic loss, permit us to proceed with some filter designs. We should, however, keep clearly in mind the distributed nature of the physical system and the expected behavior at small wavelengths. A brief characterization of distributed aspects is worthwhile here and will be useful later.

3.1 Small wavelength effects— cross modes

Specific applications sometimes place constraints on transducer size and may dictate dimensions that can be comparable to a wavelength at the higher frequencies of interest. [Note that the audible frequency spectrum spans about 10 octaves, with wavelengths (in air) of about 1700 cm down to about 2 cm.] One-dimensional wave propagation and lumped-constant approximations to acoustic parameters must, therefore, be used prudently, and with a realization that they do not adequately describe behavior at frequencies where wavelengths are comparable to device dimensions.

For small-amplitude linear wave behavior, the wave equation (2) should properly be written

$$\nabla^2\xi = \frac{1}{c^2}\frac{\partial^2\xi}{\partial t^2}, \tag{17}$$

where the ∇^2 operator is taken appropriate to the geometry. Our purpose here is not to give a tutorial on solutions of wave equations, but we need to recall two results that we will need in the subsequent discussion.

3.2 Rectangular geometry

For a rigid-wall enclosure of rectangular geometry, the (unforced) sound pressure $p(x, y, z, t)$ inside the enclosure must satisfy

$$\frac{\partial^2 p}{\partial x^2} + \frac{\partial^2 p}{\partial y^2} + \frac{\partial^2 p}{\partial z^2} = \frac{1}{c^2}\frac{\partial^2 p}{\partial t^2}. \tag{18}$$

For rectangular dimensions l_x, l_y, l_z, and with origin taken at a corner, the solution (to within a multiplicative constant) is

$$p(x, y, z, t) = \cos\left(\omega_x \frac{x}{c}\right) \cos\left(\omega_y \frac{y}{c}\right) \cos\left(\omega_z \frac{z}{c}\right) e^{j\omega t},$$

where

$$\omega = \sqrt{\omega_x^2 + \omega_y^2 + \omega_z^2} \tag{19}$$

and

$$\omega_i = \frac{c}{l_i} n_i \pi, \qquad n_i = 0, 1, 2, \cdots$$

$$i = x, y, z.$$

These conditions reflect the boundary constraint that a standing wave of pressure must have an antinode at the walls of the enclosure (correspondingly, the particle velocity normal to the walls must be zero). The eigenfrequencies (normal modes of vibration) are, therefore,

$$f = \frac{\omega}{2\pi} = \frac{c}{2}\left[\left(\frac{n_x}{l_x}\right)^2 + \left(\frac{n_y}{l_y}\right)^2 + \left(\frac{n_z}{l_z}\right)^2\right]^{1/2}. \tag{20}$$

Traditionally, the modes of the enclosure are designated by the indices (n_x, n_y, n_z).

3.3 Cylindrical geometry

In the same vein, the unforced sound pressure within a cylindrical enclosure must satisfy

$$\frac{1}{r}\frac{\partial}{\partial r}\left(r\frac{\partial p}{\partial r}\right) + \frac{1}{r^2}\frac{\partial^2 p}{\partial \phi^2} + \frac{\partial^2 p}{\partial z^2} = \frac{1}{c^2}\frac{\partial^2 p}{\partial t^2}. \tag{21}$$

For cylindrical dimensions of radius a and length l, the pressure solution (to within a multiplicative constant) is

$$p(r, \phi, z, t) = \cos(m\phi)\cos\left(\frac{\omega_z z}{c}\right) J_m\left(\frac{\omega_r r}{c}\right) e^{j\omega t},$$

where the characteristic values are

$$\omega_z = \left(\frac{\pi n_z c}{l}\right), \qquad n_z = 0, 1, 2, \cdots$$

and

$$\omega_r = \left(\frac{\pi \alpha_{mn} c}{a}\right), \tag{22}$$

where α_{mn} is the nth root of $(d/d\alpha)[J_m(\pi\alpha)] = 0$. The characteristic radian frequency is

$$\omega = \left(\omega_z^2 + \omega_r^2\right)^{1/2},$$

and the eigenfrequencies are

$$f = \frac{c}{2}\left[\left(\frac{n_z}{l}\right)^2 + \left(\frac{\alpha_{mn}}{a}\right)^2\right]^{1/2}. \tag{23}$$

Again, the normal modes of the enclosure are traditionally designated by the indices (n_z, m, n). The normal frequency descriptions of (20) and (23) will be useful to us shortly.

IV. DESIGNS FOR ACOUSTIC LOW-PASS FILTERS

If one examines the responses of typical telephone transducers (as in Fig. 1) against the requirements for voice digitization at 8-kHz sampling, the amount of low-pass band-limiting required suggests a filter of about sixth order. (The electrical filters customarily used are of this order). Our present interest, then, is to achieve this amount of band-limiting with the simplest possible acoustic structure—one that requires minimal fabrication effort and expense and has no particularly critical mechanical tolerances. One such structure is the ladder network that we alluded to earlier. Let us first do the network design, then convert this design into corresponding acoustic parameters, and finally convert these data into a real acoustic filter that can be applied to an existing telephone transducer.

4.1 Sixth-order uniform ladder network

To keep the analysis simple, let us assume that the acoustic radiation load at the input (incident surface) of the filter is small by comparison to the impedance level, and that the acoustic load on the output (typically, the microphone diaphragm) is relatively high. We, therefore, are interested in the high impedance (open-circuit) response of the

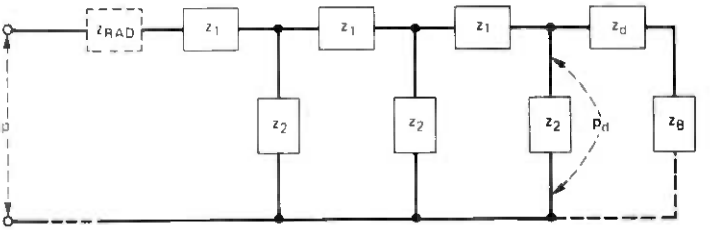

Fig. 4—Lumped network representation for a microphone filter.

filter network to a given input sound pressure, as shown in Fig. 4. The incident sound pressure is p_i and the sound pressure at the microphone diaphragm is p_d. The impedance of the microphone diaphragm and back cavity ($z_d + z_B$) is large compared to the impedance level of the filter elements.

Writing the loop equations for this uniform ladder shows that the frequency response of the transmission function (ratio of Fourier transforms of p_i and p_d) is

$$(p_d/p_i) = \frac{z_2^3}{D},$$

where the system determinant is

$$D = \begin{vmatrix} (z_1 + z_2) & -z_2 & 0 \\ -z_2 & (z_1 + 2z_2) & -z_2 \\ 0 & -z_2 & (z_1 + 2z_2) \end{vmatrix}. \tag{24}$$

Algebraic manipulation gives

$$p_d/p_i = \frac{1}{(x^3 + 5x^2 + 6x + 1)},$$

where

$$x = (z_1/z_2).^* \tag{25}$$

We estimate the three real roots of the denominator of (25) as

$$r_1 = -0.20$$

$$r_2 = -1.57$$

$$r_3 = -3.25. \tag{26}$$

And we see that this form of network exhibits only poles in its transfer function. If the serial element z_1 were essentially a lossy (resistive) lumped inertance (as would be the case for a relatively small constrict-

* Note this characteristic equation is sixth-degree in frequency, ω.

ing tube or an aperture) and the shunt element z_2 essentially a lossy (conductive) lumped compliance, then

$$(z_1/z_2) \cong (R + sL)(G + sC), \tag{27}$$

and the complex frequencies, s, for which singularities exist in the transfer function are

$$s_i = (-\alpha \pm j\beta_i),$$

where

$$\alpha = \frac{1}{2}\left(\frac{R}{L} + \frac{G}{C}\right)$$

and

$$\beta_i^2 = (\beta_{0i}^2 - \alpha^2) = \left(\frac{RG - r_i}{LC} - \alpha^2\right), \qquad i = 1, 2, 3. \tag{28}$$

That is, the poles occur in three sets of complex conjugates, all with the same damping.*

4.1.1 Calculation of acoustic parameters—uniform ladder

Given these results, together with a prescribed transducer, how do we formulate the acoustical structure?

First we wish to choose the singularities of the filter transfer function so that, when taken in combination with the specified transducer, the combined response meets a particular criterion. We will be guided here roughly by the typical T1-carbon button and the EL-2 electret responses, shown in Fig. 1, and the D-channel bank band-limit specifications. This typically will result in a low-pass filter that attenuates early in frequency to compensate for the characteristic rise in the T1 and EL-2 responses at around 3 to 4 kHz. It is convenient to choose the singularities on the basis of the lumped constant relations (28), but we will remain alert to the distributed nature of the problem so as not to be misled by this simplification.

In accordance with these criteria then, we select values as follows. For relatively low loss ($RG \ll r_i$),

$$\beta_{0i} \cong \left(\frac{r_i}{LC}\right)^{1/2} \text{ radians/sec}$$

and

$$f_{0i} \cong \frac{1}{2\pi}\left(\frac{r_i}{LC}\right)^{1/2} \text{ hertz.} \tag{29}$$

* Provided the loss factors R, G are frequency independent.

We choose the product, $LC = 6.44 \times 10^{-9}$ to yield

$$\beta_{01} = 5{,}912 \text{ sec}^{-1}; \qquad f_{01} \cong 887 \text{ Hz}$$
$$\beta_{02} = 15{,}708 \text{ sec}^{-1}; \qquad f_{02} \cong 2{,}487 \text{ Hz}$$
$$\beta_{03} = 22{,}481 \text{ sec}^{-1}; \qquad f_{03} \cong 3{,}578 \text{ Hz}, \tag{30}$$

and a damping corresponding to

$$\alpha \cong 2330 \text{ sec}^{-1}.* \tag{31}$$

Recall that the quality factor Q for a simple resonance is $Q = (\beta/2\alpha) = f/\Delta f_{-3dB}$. The choices therefore correspond to Q's of

$$Q_1 \cong 1.3$$
$$Q_2 \cong 3.4$$
$$Q_3 \cong 4.8. \tag{32}$$

These values are chosen to produce a filter which, when used in combination with a T1 carbon button or a WE EL-2 electret, will approximate the D-channel bank band limits.

4.1.2 Acoustic filter design— T1 uniform ladder

The next matter is how to convert the choice of α and β_{0i}'s into a physical acoustic structure. We are interested in the T1-transmitter size and the EL-2 size as existing telephone transducers. Let us consider the T1 size first. We will make this design for an experimental electret microphone having the same size as the T1-transmitter but intended to be a higher-quality replacement for the carbon button.

Some constraints then are: simplicity of fabrication; the diameter of the circular mike, namely, 46 mm; a maximum length of the filter that will allow it to fit into the conventional telephone handset; and an interest in keeping acoustic impedance levels low enough that stray losses do not dominate the intended losses. And, oh yes, watch out for shortwave effects.

A straightforward design that meets these constraints is shown in Fig. 5. The values are arrived at through the following sequence. We have already selected the product $LC = 6.44 \times 10^{-9}$ to set favorable pole positions. Now, as a convenient value, choose

$$C = 4.0 \times 10^{-6} \text{ acoustic farads},$$

which implies

$$L = 1.61 \times 10^{-3} \text{ acoustic henries}.$$

* These choices are the results of several trial calculations for the characteristics desired for the prescribed transducers.

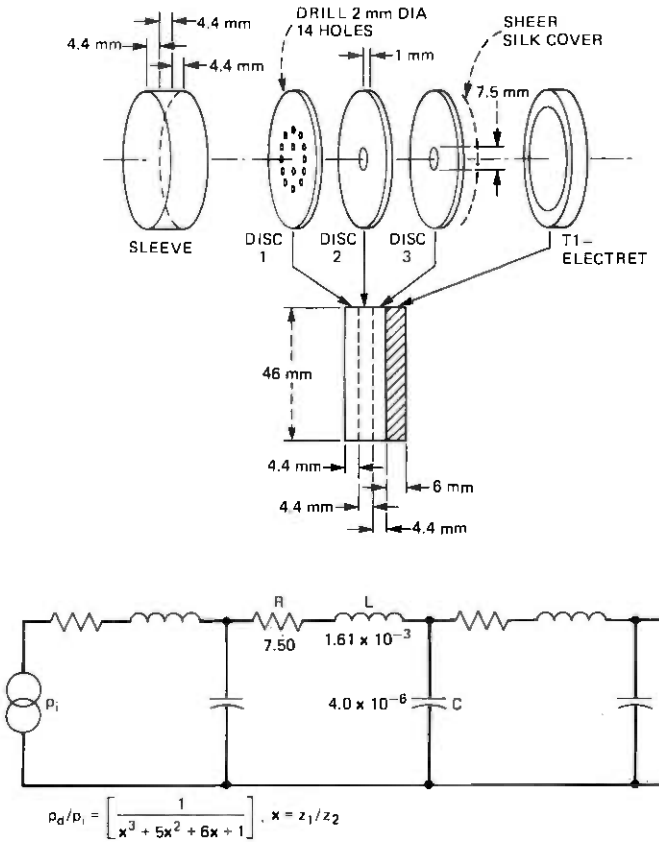

Fig. 5—Physical design of a uniform ladder acoustic filter for a T1-size electret microphone.

The choice $\alpha = 2330$, together with the intent that most loss will be supplied by R leads to

$$R = 7.5 \text{ acoustic ohms.}$$

From the lumped compliance relations (16), and the diameter of the transducer, we calculate the length of each cavity to be

$$C = \frac{\pi(4.6)^2}{4} l/\rho c^2 = 4.0 \times 10^{-6}$$

or

$$l = 0.34 \text{ cm.}$$

Similarly, from the lumped inertance relation (14), we calculate the diameter of the thin aperture to be

$$d = \rho/L = \frac{1.21 \times 10^{-3}}{1.61 \times 10^{-3}} = 0.75 \text{ cm.}$$

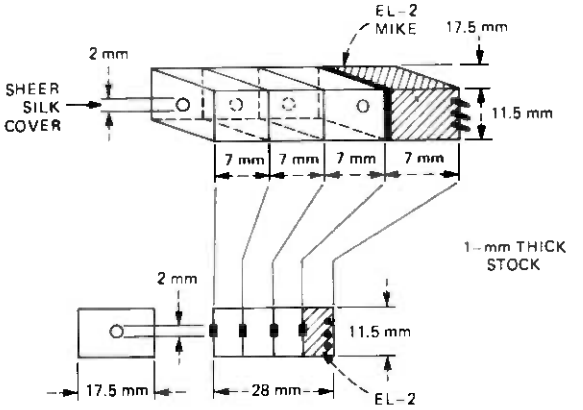

Fig. 6—Physical design of a uniform ladder acoustic filter for a WE model EL-2 electret microphone.

This aperture has an area of 0.44 cm^2. To diminish symmetry and combat distributed effects, and to pick up additional damping, we have in this instance chosen to implement the cover-plate inertance as a group of 14 parallel holes having an open area equivalent to the single perforation.* The damping of the perforations is much less than is needed, so sheer silk cloth (128 × 124 fibers/inch) was used to implement lumped R's. This screen is estimated to give about 3–5 cgs ohms for 1 cm^2 area.

Also, right off, we are on guard about the large diameter of this structure—which we chose to be the easiest fit to the T1 microphone size.

Using the same fundamental design, we have two other interests. One is in placing the singularities of the filter transfer function a bit higher, so as to make the filter a bit more appropriate for a flat response transducer (rather than for the slightly rising characteristics shown in Fig. 1). Another is to apply the design to the smaller EL-2 electret, and to other microphones as well.

4.1.3 T1-9mm bore

To examine the first interest, we increased the pole frequencies by reducing the inertance values. (Note that the mechanical precision for establishing d is the same as for establishing the value of L.) We scaled the pole values up by approximately 10 percent by reducing the L

* This choice is consistent with approximating the lumped inertance as $\rho l/A$, but is not consistent with ρ/d. Several factors enter the consideration. The effective length of the aperture is more nearly $l_e = (l + 1.7a)$, and for the small holes l and a are comparable in size. Additionally, viscous effects increase the apparent inertance, as does the mutual reactance among an array of ports.

values by about 17 percent, by enlarging the openings between cavities to a 0.9-cm diameter. The damping values were maintained the same.

4.1.4 EL-2 uniform ladder

A filter design suitable for use with the EL-2 electret was also made from the uniform ladder analysis. This is easily done by noting the EL-2 dimensions, and scaling the acoustic impedance levels accordingly. Our choice for this is shown in Fig. 6, where the values represent an impedance level scaling of ×4 upwards, namely,

$$L = 6.44 \times 10^{-3}$$

$$C = 1.0 \times 10^{-6}$$

$$R = 30.$$

In this case, the 2-mm aperture is used for each inertance.

4.1.5 Primo uniform ladder

The same type of impedance scaling (upward ×8) leads to a similar design for the round (1-cm diameter) Primo electret microphone, as shown in Fig. 7.

4.2 Tapered ladder designs

Another approach which allows much greater flexibility in design, but which is more complicated to fabricate, is a tapered ladder design. In this case, the acoustic impedance of the filter network can be elevated in going from input to transducer diaphragm, allowing a wide range of choices for element sizes. In particular, increasing the impedance level permits smaller dimensions of the filter elements, and hence a greater freedom from cross modes and short wavelength effects. Further, if the impedance taper is substantial, each ladder section is not greatly loaded by the following one, and the singularities of the transfer function can be identified with each section of the ladder making for very simple calculation of the response. The poles can, of

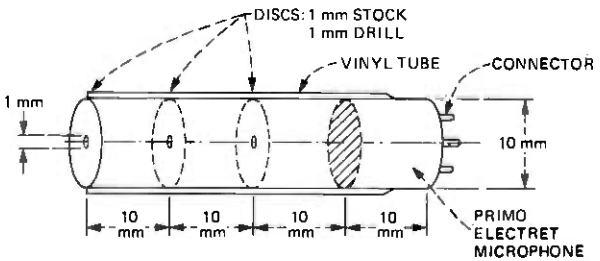

Fig. 7—Physical design of a uniform ladder acoustic filter for a Primo (Japanese manufacture) electret microphone.

course, be distributed to best advantage for a given application—which, in some instances, might be a tight cluster of poles near the band edge.*

4.3 Tapered ladder with side branch

The tapered design and the relative impedance isolation of the ladder sections permit an easy introduction of side-branch resonators. The side branch can be used to "plant" a zero of transmission in the transfer function in an advantageous way. Typically, this might be used to steepen the rate of cut-off at the band edge. This feature, of course, is obtained at the expense of the asymptotic rate of cut-off and out-of-band rejection (because the net order of the filter is effectively reduced).

A tapered design for the T1 telephone transmitter with a side branch designed to approach the D-channel bank limits is shown in Fig. 8. In this instance, the impedance level of the prototype ladder filter ascends by about a factor of 2 with each section, and the poles have all been pushed toward the 2- to 4-kHz range. The side branch modification is made to place a zero of transmission at 4 kHz, to steepen the rate of cut of the filter as 4 kHz is approached. The damping is chosen to provide pole Q's of approximately 1.5 to 2.0 and a Q for the zero (anti-resonance) of about 10.0.

V. COMPUTED RESPONSES FOR THE ACOUSTIC FILTER DESIGNS

To explore the expected behavior of these filter designs, we wrote Fortran programs to calculate and plot the frequency-vs-amplitude and frequency-vs-phase responses. The programs also provided comparisons between the responses using a lumped-constant formulation and one using the distributed one-dimensional parameters of (16). In the latter, the cavities were represented by T-sections of trigonometric elements. Lumped inertances were retained for the apertures.†

5.1 Computed responses— uniform ladder

The log-amplitude, phase, and linear-amplitude responses vs frequency for the T1-uniform ladder network of Fig. 5 are shown in Figs. 9a to 9c. These responses are calculated for distributed one-dimensional parameters. As previously mentioned, the choice of net-

---

* Note, too, that other possibilities exist for implementing more complex filters. For example, the low-pass structure can be converted into a bandpass structure by introducing an aperture, or communicating air path, between the inside volume of the large cavities and the outside air. In effect, this places an inertance in parallel with each shunt compliance of the ladder network.

† The radiation impedance is taken (for computational tractability) as that for a circular piston in an infinite baffle. When the radiation impedance is overtly represented, the value of the aperture inertance at the filter face is reduced by one-half.

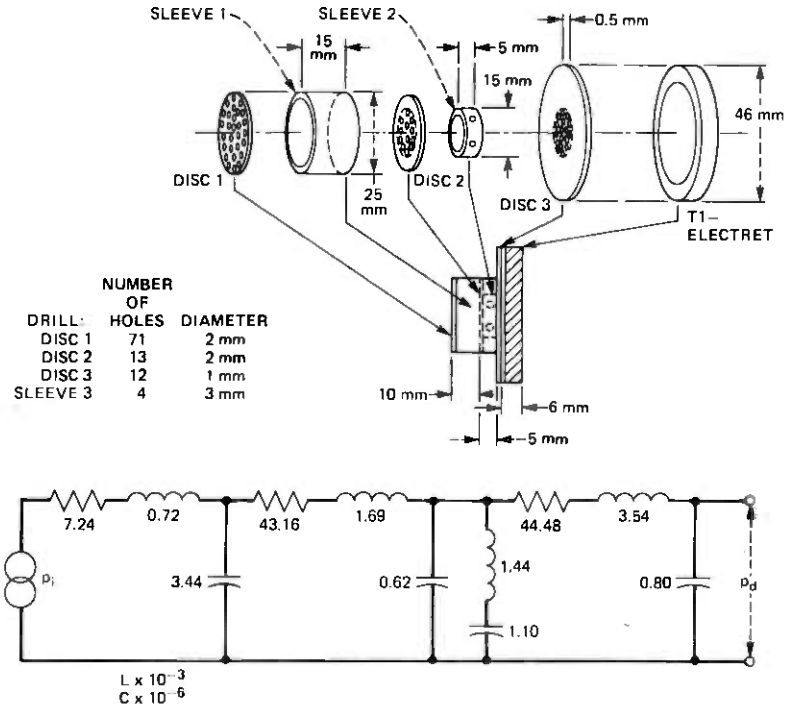

Fig. 8—Physical design of a tapered-ladder acoustic filter for a T1-size electret microphone.

work values anticipates the combined response of the filter applied to a microphone with enhanced high-frequency response.

Computation of the response using lumped and one-dimensional distributed formulations showed relatively small differences, suggesting that the arguments made about lumped approximations (for the dimensions of interest) were reasonable. The amplitude response calculated from lumped elements is shown dashed in Fig. 9c. This difference was the greatest encountered, because the T1 microphone was the largest-size transducer considered.

Note that none of the programmed (one-dimensional) wave calculations account for short wavelength cross-mode effects, which we would expect to see at frequencies around 10 kHz.

The calculated lumped-constant response of the uniform ladder design for the EL-2 electret is sensibly the same as for the T1 microphone. The designs differ only by an impedance scaling of 4. The one-dimensional distributed behaviors differ only in small detail (and only at the higher frequencies) in that, because of its smaller dimensions, the EL-2 uniform ladder is better represented by the lumped elements used for the design (i.e., distributed parameter effects are not as great in the smaller EL-2).

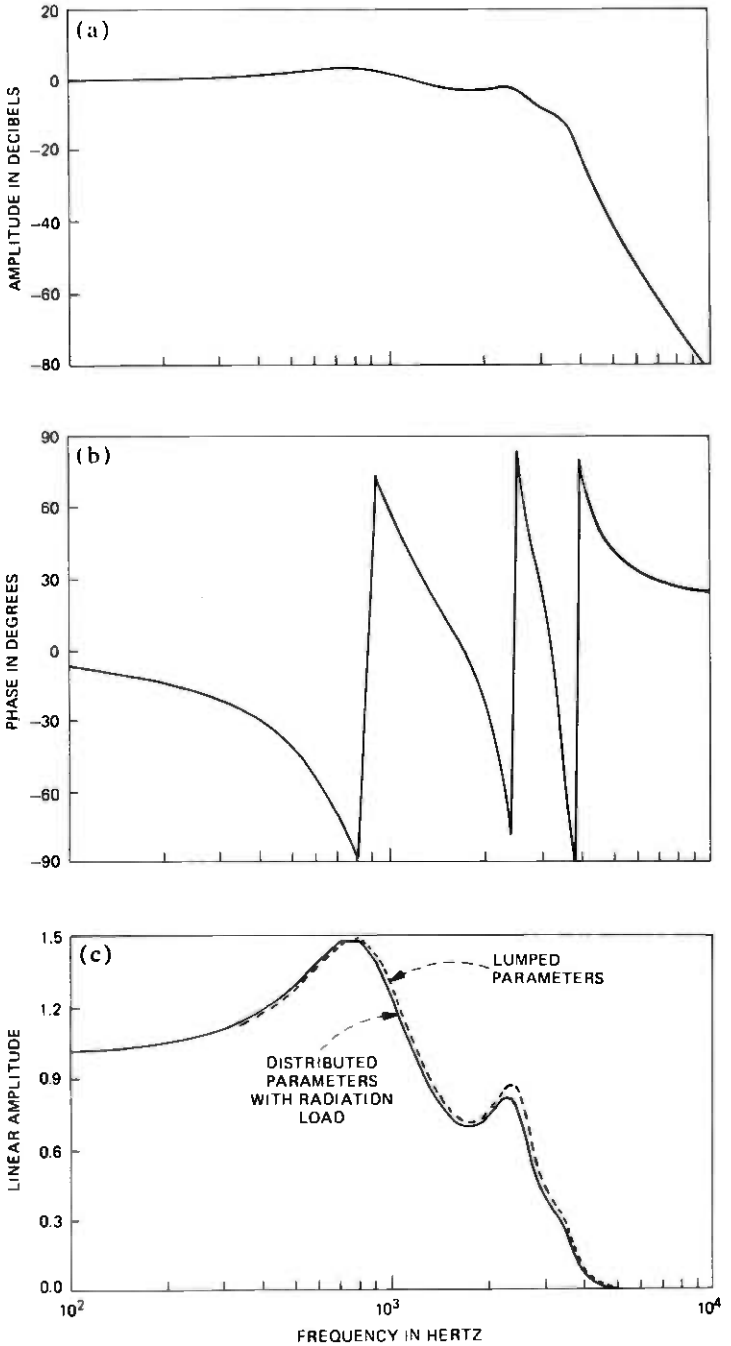

Fig. 9—Computed responses for uniform-ladder acoustic filter of Fig. 5. (a) Log amplitude response. (b) Phase response. (c) Linear amplitude response.

A calculation of the uniform ladder response with lumped parameters and small damping, specifically R's = 0.1 cgs ohms, places the poles of the transfer function in clear evidence, as shown in Fig. 10a. The same computation with distributed parameters, radiation impedance, and small damping gives nearly the same result, shown in Fig. 10b.

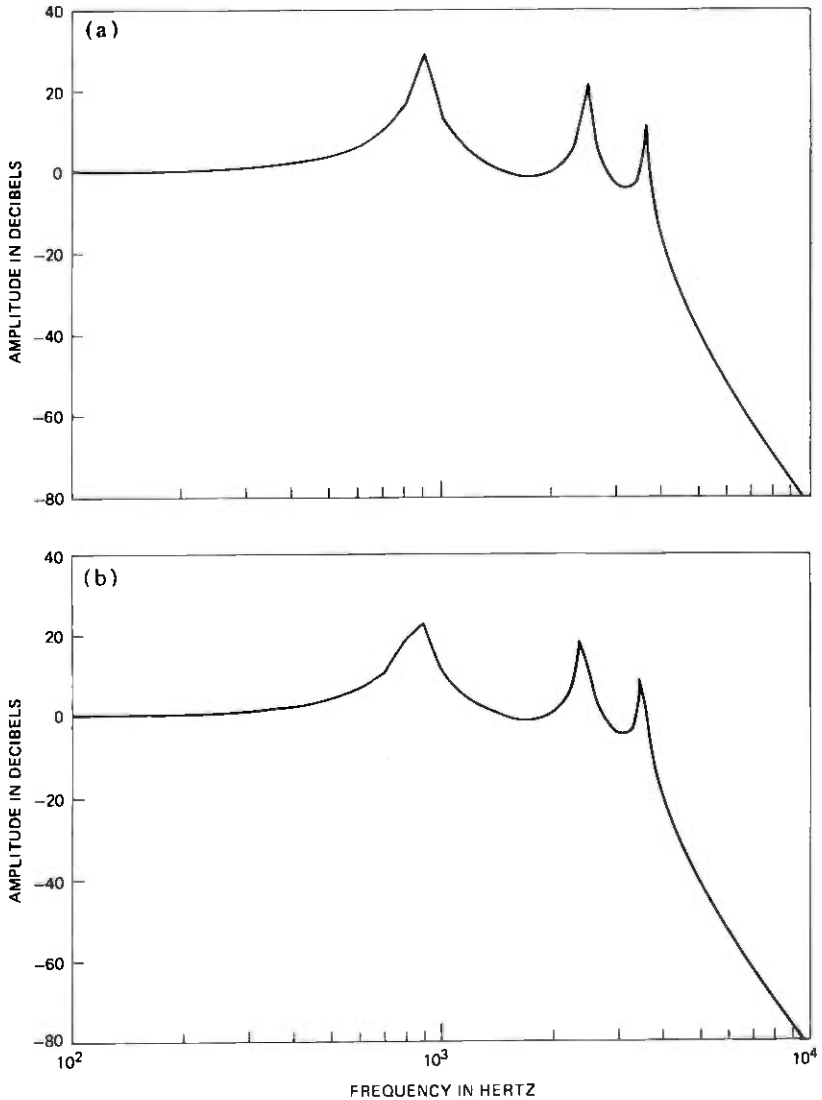

Fig. 10—Computed amplitude-frequency response for filter of Fig. 5 with low damping (R's = 0.1 ohm). (a) Lumped parameters. (b) Distributed parameters.

In general, the poles fall approximately as designed.

A side interest in fabrication is the effect of distribution of damping in the filter. A calculation for $R1 = 7.5$ cgs ohms and $R2 = R3 = 0$ is shown in Fig. 11a. The effect is to reduce the damping of all modes. The response of Figure 11c is obtained if $R1$ and $R3$ are interchanged, i.e., for $R1 = R2 = 0$, and $R3 = 7.5$ ohms. If the damping is placed only in the center rung of the ladder ($R1 = R3 = 0$, $R2 = 7.5$ ohms), the result is the response of Fig. 11b, where the second mode appears relatively underdamped

5.2 Computed responses— tapered ladder with side branch

The calculated amplitude and phase responses for the tapered ladder filter shown in Fig. 8 are given in Figs. 12a and 12b.* The effect of the side-branch zero placed at 4 kHz is readily apparent.

As an ancillary point, in hindsight, this design can be improved somewhat by reducing the size of the second rung shunt compliance ($C2P$) in the network from its original value of 0.62×10^{-6}. This can be done by a smaller inner sleeve in the filter. A reduction to the value $C2P = 0.05 \times 10^{-6}$ acoustic farads gives the improved response of Figs. 13a and 13b.

As another side point, the tapered ladder without the transmission zero also yields an effective all-pole filter. The response of the filter of Fig. 8 with the shunt resistance and inductance set to zero (i.e., $R2P = XL2P = 0$) gives the response of Figs. 14a and 14b.

A calculation of this response with lumped constants and low damping (R's = 0.5) shows that the transmission poles have been pushed somewhat higher in frequency than for the uniform ladder (Fig. 15).

VI. FABRICATION OF PROTOTYPE MODELS

The model-shop machinist constructed physical filters from the drawings of Figs. 5 through 8. The models were made from brass because of the ease in machining, but, in practical application, the filters would be molded in plastic or stamped from sheet metal as part of the telephone set fabrication.

Also, for ease in making modifications for measurement, the housings of these first models were made so that assembly and disassembly could be rapidly done. This poses some dangers in that the fittings must be airtight to perform properly acoustically. Considerable care is therefore required in the experimental measurements.

The filter models as produced by the machinist are shown in Fig. 16.

* Calculated from lumped parameters.

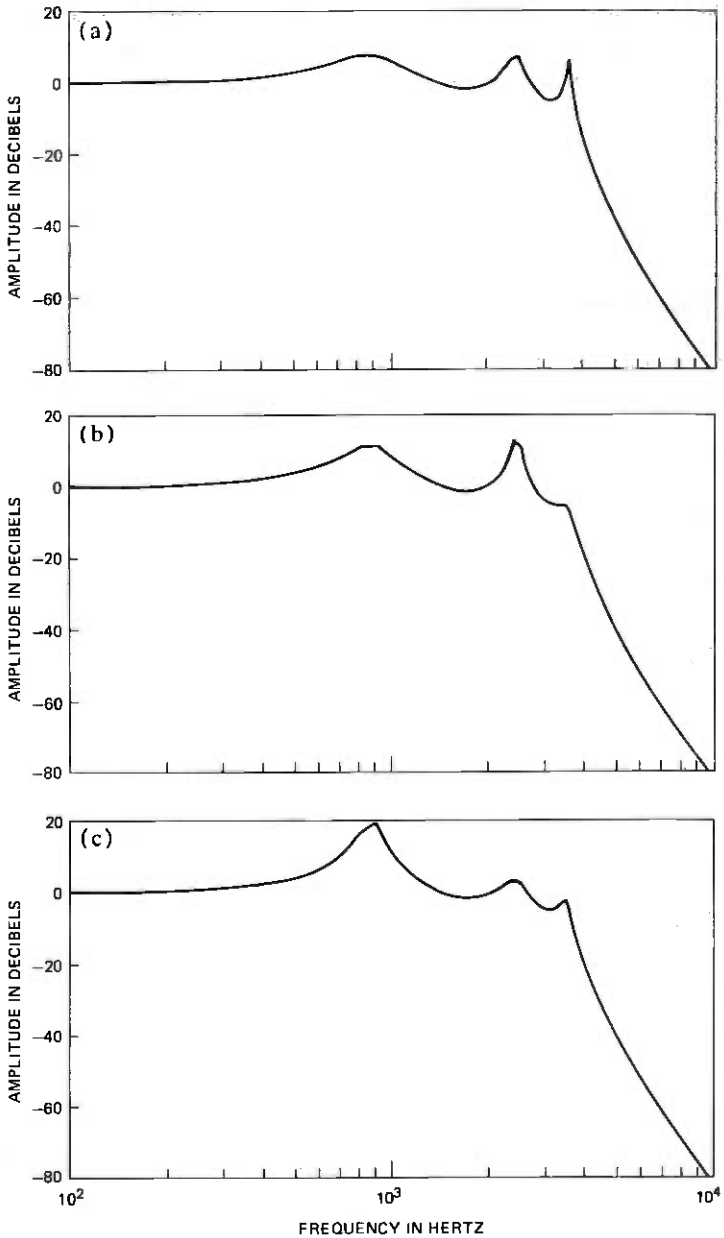

Fig. 11—Effects of location of damping (a) $R1 = 7.5\ \Omega$, $R2 = R3 = 0$. (b) $R2 = 7.5\ \Omega$, $R1 = R3 = 0$. (c) $R1 = R2 = 0$, $R3 = 7.5$.

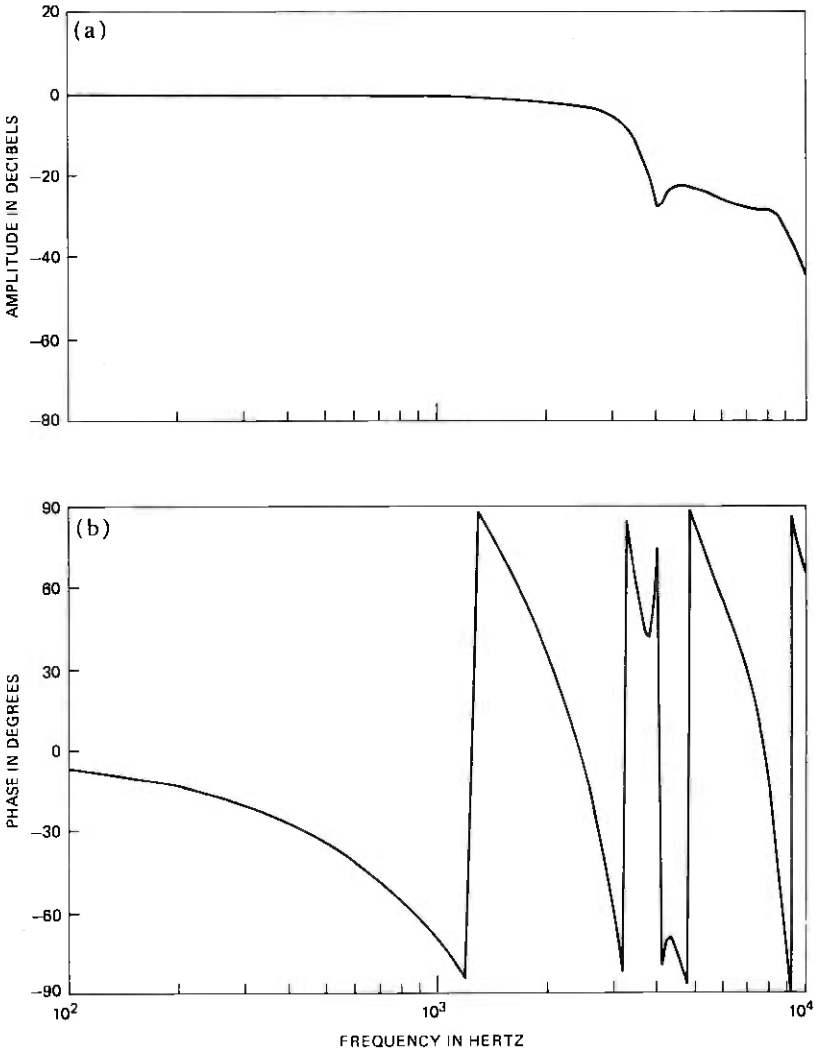

Fig. 12—Computed responses for tapered-ladder acoustic filter of Fig. 8. (a) Log amplitude response. (b) Phase response.

VII. EXPERIMENTAL MEASUREMENTS

The acoustic responses of the filter models shown in Fig. 16 were measured in the Murray Hill anechoic chamber. The experimental set-up is shown in Fig. 17.

Each experimental filter and microphone was set adjacent to a calibrated condenser microphone (B&K ½ inch). Both microphones received sound at normal incidence from an 8-inch loudspeaker source

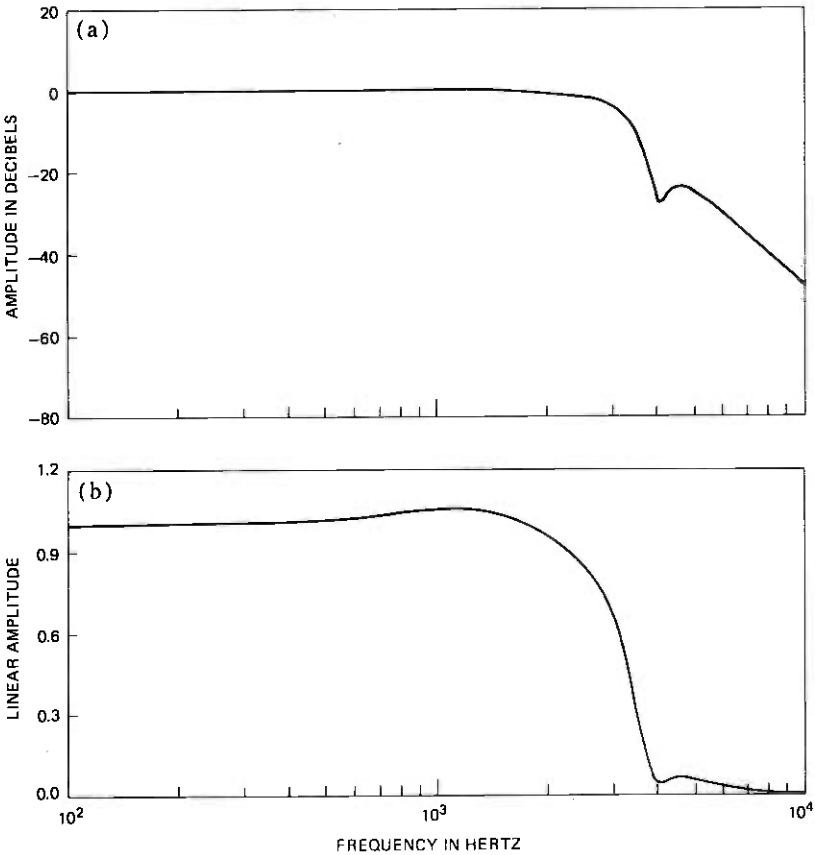

Fig. 13—Response of Fig. 12 modified by reduction in second cavity size (C2P = 0.05 × 10^{-6}). (a) Log amplitude response. (b) Linear amplitude response.

2 meters away. The loudspeaker received sine-wave signals of variable frequency from a precision oscillator. Most responses were measured by maintaining a fixed sound pressure of 1 microbar at the experimental microphone. This provided a signal-to-background-noise ratio usually greater than 40 dB. In several instances, high-pass electrical filtering was used on the microphone output to eliminate ventilation noise and 60-cycle pick-up and to increase the signal-to-noise ratio to greater than 50 dB. Normally, this filtering was not used, so as not to add the electrical filter response to the microphone and acoustic filter.

7.1 Measured responses— T1 uniform ladder

The uniform ladder filter for the T1 telephone transmitter shown in Fig. 5 was fitted to an experimental electret microphone, and its response was measured with no acoustic resistances in place. This

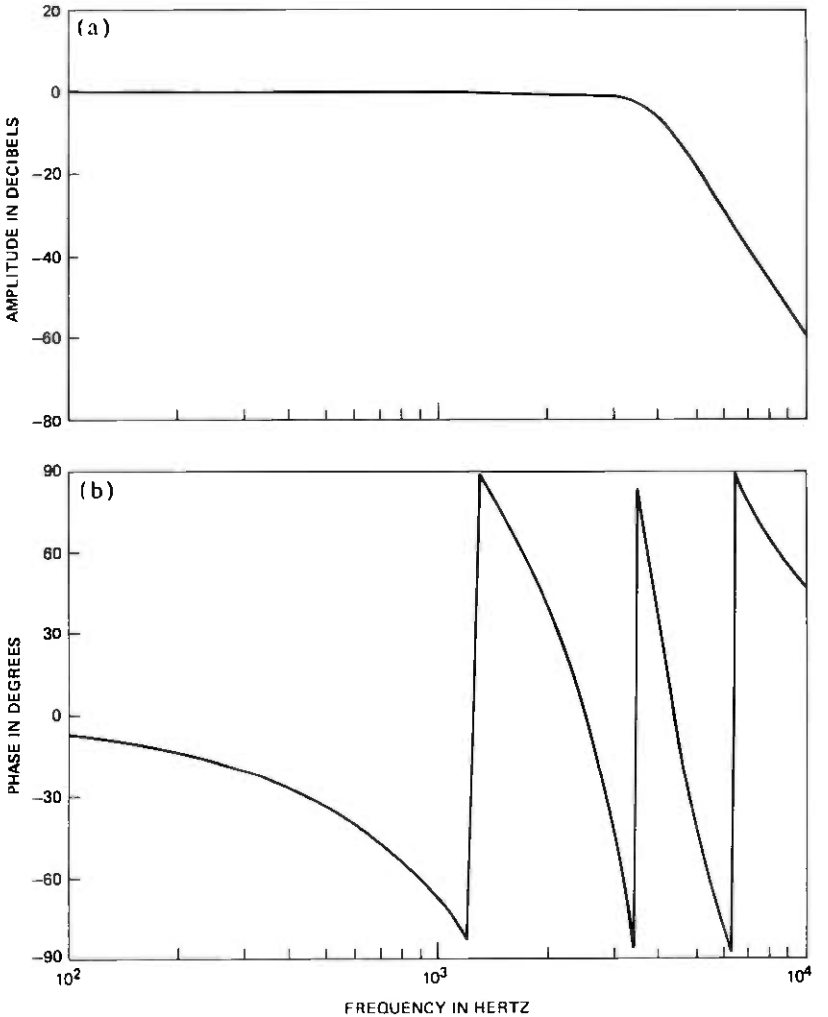

Fig. 14—Response of Fig. 12 modified by elimination of the side branch. (a) Log amplitude response. (b) Phase response.

measurement is shown in Fig. 18. The response of the microphone alone was also measured, and the difference between these curves gives the response of the acoustic filter, as shown in Fig. 19. The three mode frequencies predicted by the lumped constant design are prominent in the response.* They appear nearly where expected, but the higher two resonances are measured about 10 percent lower than where expected from lumped-constant arguments. One possible reason

* Along with a very large cross-mode response at about 10,000 Hz, to be addressed directly.

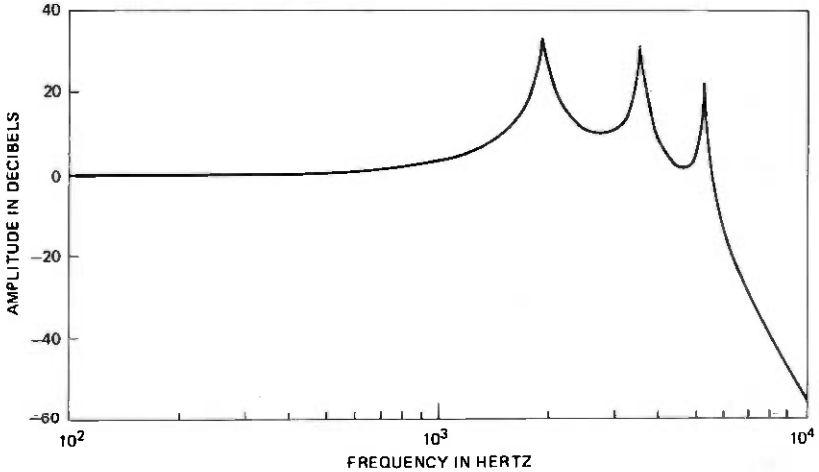

Fig. 15—Response of Fig. 14 with low damping (R's = 0.5 Ω).

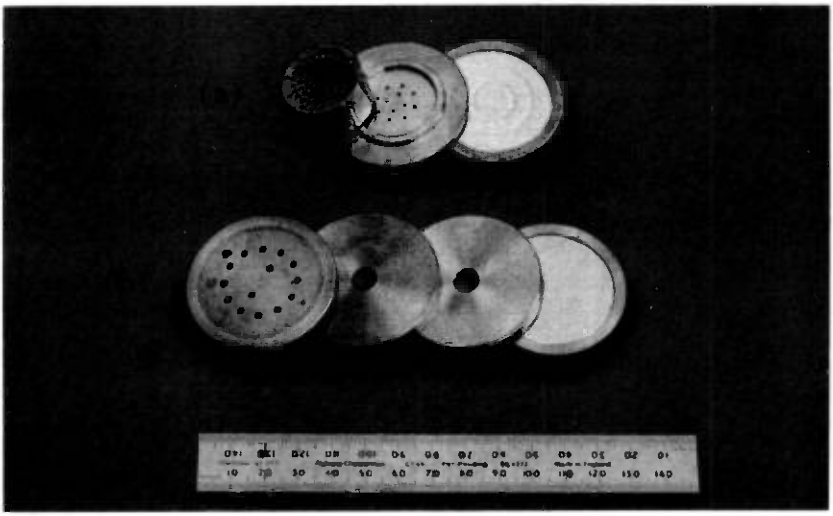

Fig. 16—Prototype acoustic filters machined in the model shop. (a) T1 tapered ladder. (b) T1 uniform ladder. (*continued on page 929*)

is that the simple relation $L_a = \rho/2a$ yields a larger value than desired. (This is supported by the "end effect" radiation reactance point of view that leads to $L_a = 0.54\ \rho/a$, which says that an aperture of radius a gives an inductance 8 percent greater than the traditional $\rho/2a$ value*).

Note also, in the response without damping, the tremendous high-

* Viscous behavior in the apertures also contributes to the apparent inertance.

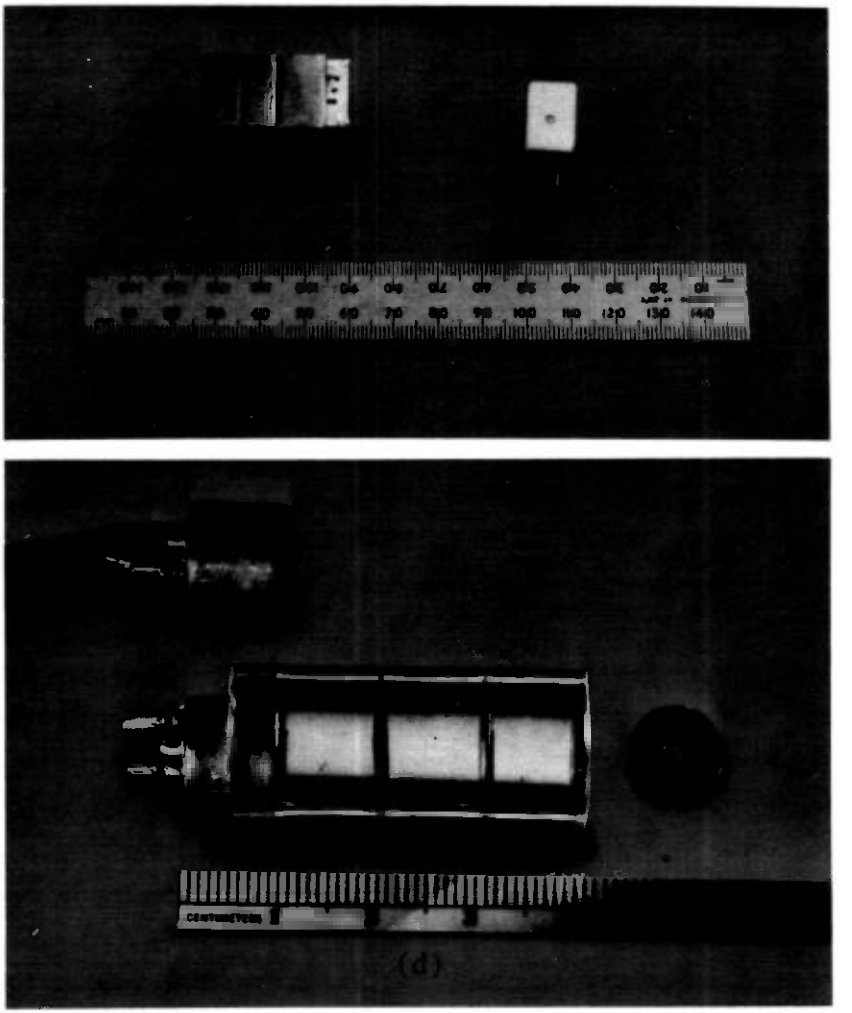

Fig. 16 (*continued*)—(c) EL-2 uniform ladder. (d) Primo uniform ladder.

frequency peak at about 10 kHz. Recall from Fig. 5 that the diameter of the circular microphone and acoustic filter is 46 mm. (In the inner chamber, this is reduced by the thickness of the walls to approximately 44 mm.) The overall length of the communicating chambers of the acoustic filter is [(3.4 mm × 3) + 2 mm] = 12.2 mm. Considering the whole structure as a cylindrical enclosure, we can use eq. (23) to calculate the expected normal modes. We need additionally only the roots of

$$\frac{d}{d\alpha} J_m(\pi\alpha) = 0.$$

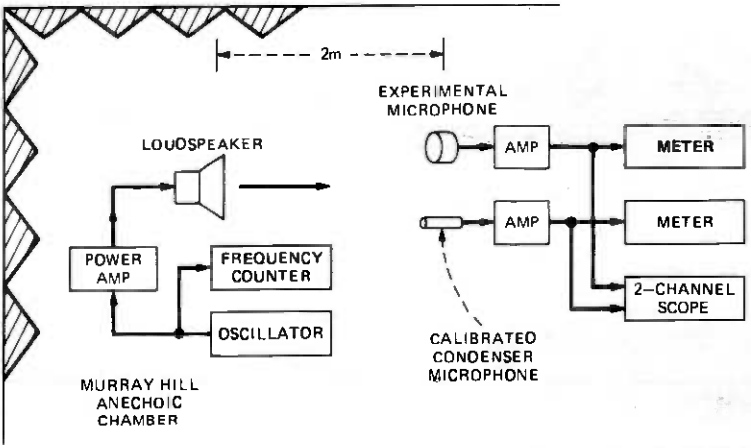

Fig. 17—Arrangement of laboratory equipment for experimental measurements in the anechoic chamber.

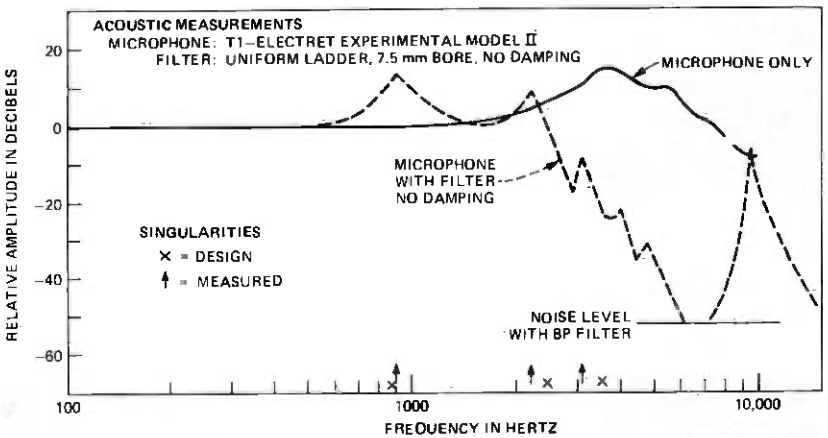

Fig. 18—Measured response of the T1-uniform ladder filter with no damping and its electret microphone.

The first few values of α_{mn} are shown in Table I. Equation (23) therefore gives the eigenfrequencies in Table II. Because the cavities really communicate only through the apertures, the length dimension mode for $l = 12.2$ mm is not readily excited. Even if it were, it is relatively high in frequency—largely well out of the speech frequency range.* If the effective length dimension is taken perhaps more realistically as equal to a single cavity thickness, then the first z-direction mode is put at 50 kHz.

* The nature of the speech signal spectrum, which typically diminishes at −6 to −12 dB per octave at high frequencies, also helps to de-emphasize the effects of high frequency modes.

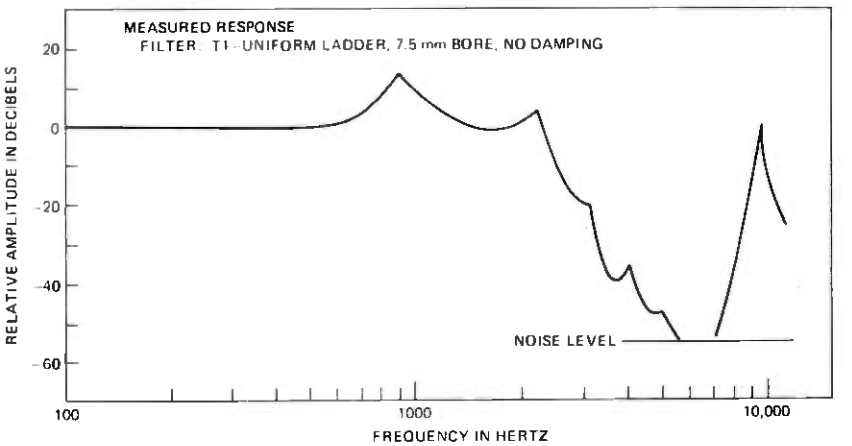

Fig. 19—Measured response of the T1-uniform ladder filter, 7.5-mm bore, no damping.

Table I

m/n	0	1	2
0	0	1.22	2.33
1	0.59	1.70	2.71
2	0.97	2.13	3.17

Table II

Mode number			Frequency (hertz)*
n_z	m	n	$f = (f_z^2 + f_r^2)^{1/2}$
0	0	0	0
1	0	0	13,934
0	1	0	4,361
0	0	1	9,017
1	1	0	14,601
1	0	1	16,597
0	1	1	12,565
1	1	1	18,763

* For 46-mm diameter.

The lowest indicated mode is the (0, 1, 0) mode at 4331 Hz. Recall that the (n_z, m, n) convention is such that the m, nth wave has m plane nodal surfaces extending radially from the axis, and n cylindrical nodes concentric with the axis. The m-waves correspond to standing pressure waves in the ϕ-direction and the n-waves correspond to radial standing waves of pressure in the r-direction. The geometry of the filter is such that the m-waves might be expected to be difficult to excite. If the (0, 1, 0) mode is excited, it is relatively weak and possibly shows up as a slight peak in the response near 4000 Hz.† The first radial mode (0, 0, 1), however, is a different story, and the center

† A similar argument might be given for the 0, 2, 0 mode at 7,170 Hz.

aperture seems favorable for exciting this mode strongly in one or more of the cavities. This mode appears to account for the truly sizeable high frequency response between 9 and 10 kHz. In realizing a useful filter of dimensions this large, therefore, considerable attention needs to be given this mode. Other modes seem well out of the speech frequency range.

In damping this particularly undesirable (0, 0, 1) mode for this filter

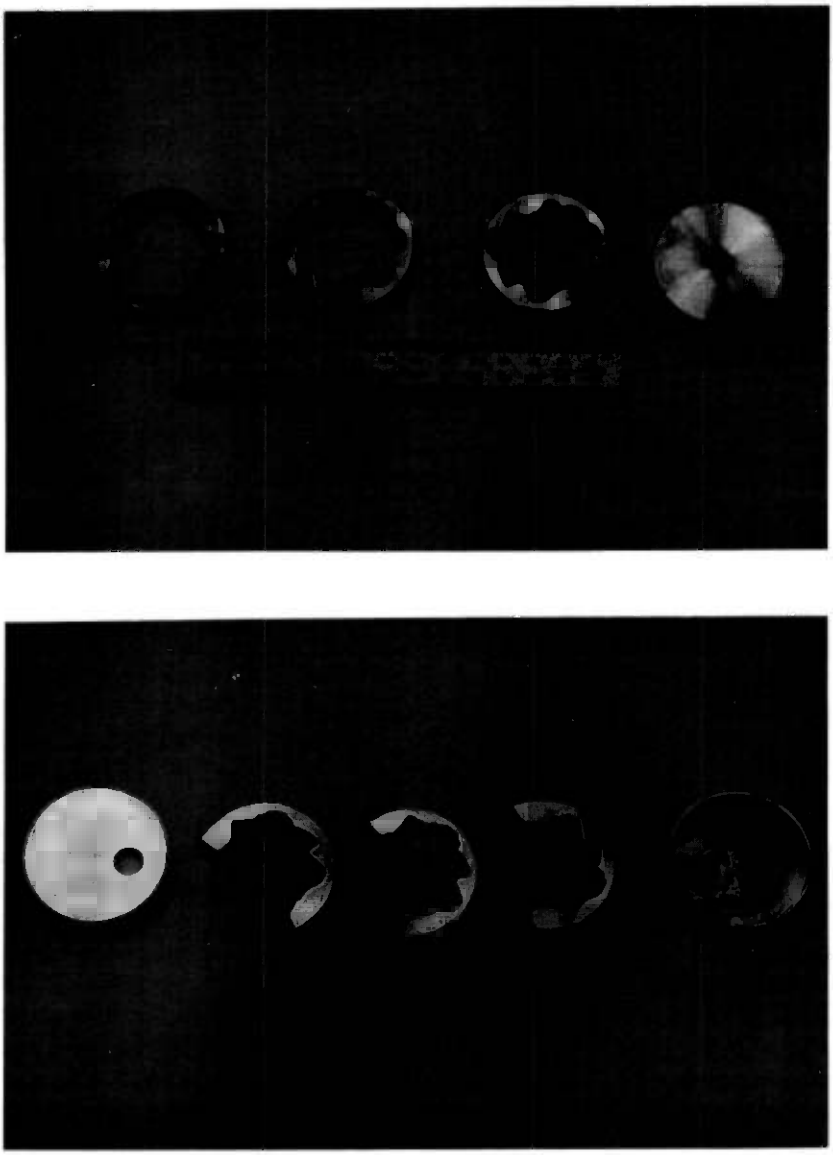

Fig. 20—Brass rings (cavity inserts) cut with irregular radii.

size, we recall the mode energy is most effectively absorbed by sound absorptive material placed near pressure maxima, and that reduction of the radial symmetry would suppress its excitation.

As a very simple expedient to reduce radial symmetry, we can introduce an irregular inner surface into the cavities by means of some brass rings cut with a random radius. A set of such rings is shown in Fig. 20a. The symmetry can be even more affected by using only the ⅔ arc rings of Fig. 20b. The random radius is selected to look "rough" at wavelengths corresponding to about 10 kHz. The volume displacement of the rings is small enough that the cavity volume, and hence the acoustic capacity, is not changed much from the original design value. We can also include the prescribed silk-screen resistors in the

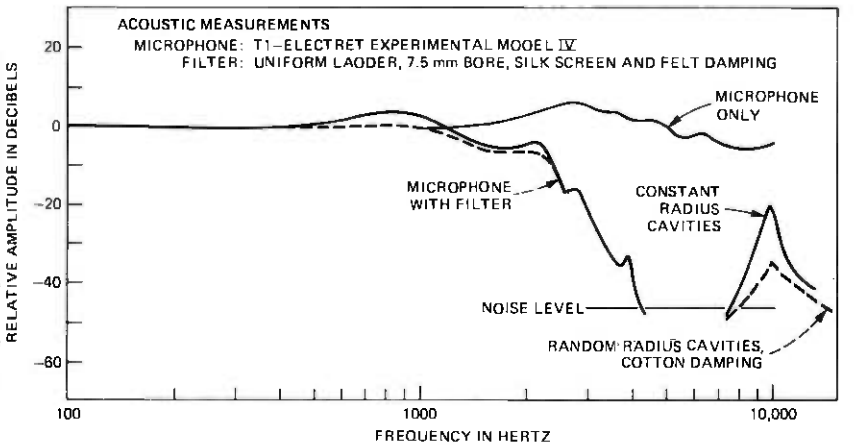

Fig. 21—Measured response of the T1-uniform ladder filter 7.5-mm bore, with damping and its electret microphone.

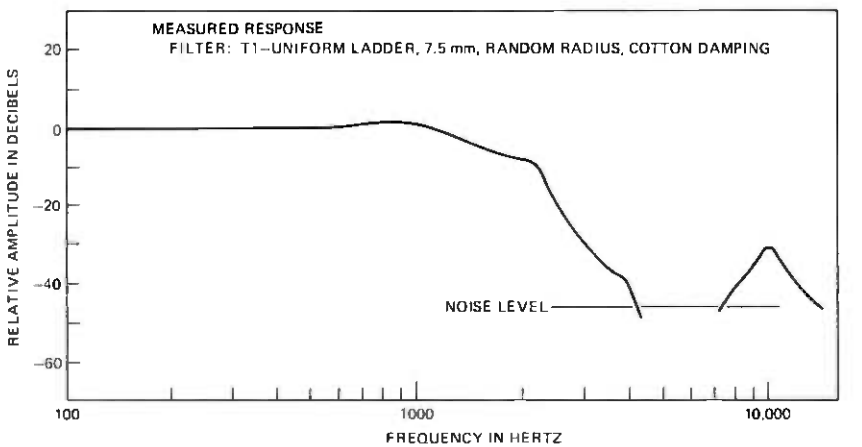

Fig. 22—Measured response of the T1-uniform filter, 7.5-mm bore, with mode suppression.

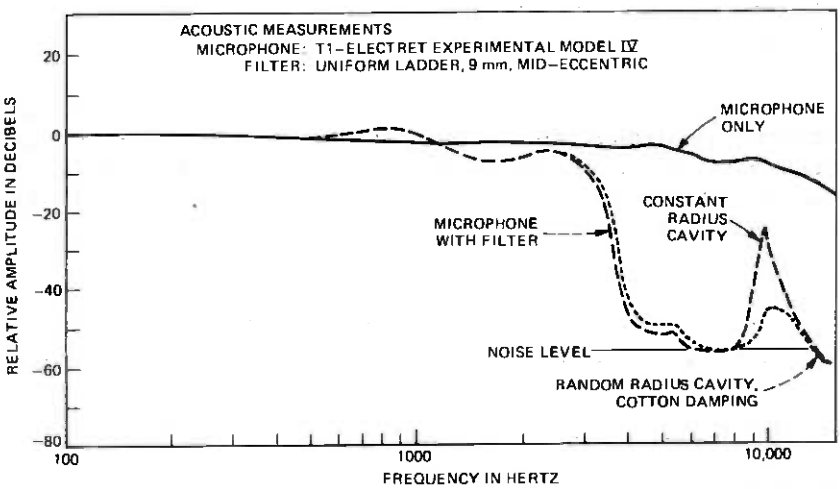

Fig. 23—Measured response of the T1-uniform ladder, 9-mm bore, and its microphone.

apertures, as well as a small amount of absorbent cotton in the cavity and cotton felt strips around the periphery. When this is done, the response of the radial mode is brought more under control, as shown by Figs. 21 and 22. This situation can be improved a bit more, even keeping the large T1 dimensions.*

The underestimate of the inertances, as discussed previously, together with the design objective that uses a microphone response rising at the high frequencies, gives us a filter that cuts off at fairly low frequencies. A 20-percent increase in the bore radius of the apertures should give an inertance reduction of 17 percent and an increase in pole frequencies of 10 percent. In addition, we can reduce the possibility for (0, 0, 1) mode excitation by placing at least one of the apertures (the center one here) off center (as shown in Fig. 20). The response of this T1-size uniform ladder is given in Figs. 23 and 24, where one sees the out-of-band rejection is successfully held at −40 dB.

7.2 Measured responses— tapered ladder with side branch

The filter design of Fig. 8 has some dimensions that are smaller (and hence less susceptible to distributed effects), but the final cavity is left with the 44-mm inner diameter.

The measured response of this filter is shown in Figs. 25 and 26.†

* A number of other possibilities exist for controlling cross-mode behavior. Their effectiveness and sophistication depend upon the willingness to complicate the physical construction of the filter. All depend upon minimizing symmetry and reducing dimensions of the acoustic elements. Straightforward approaches include enclosures having nonparallel, asymmetric, incommensurate walls, and internal partitioning to implement the overall filter as a number of smaller-sized filters in parallel. Several preliminary implementations of these notions yield significant suppression of cross modes.

† Differences among microphone-only responses are conditioned largely by differences in clamping tension for repeated installations in the experimental holder.

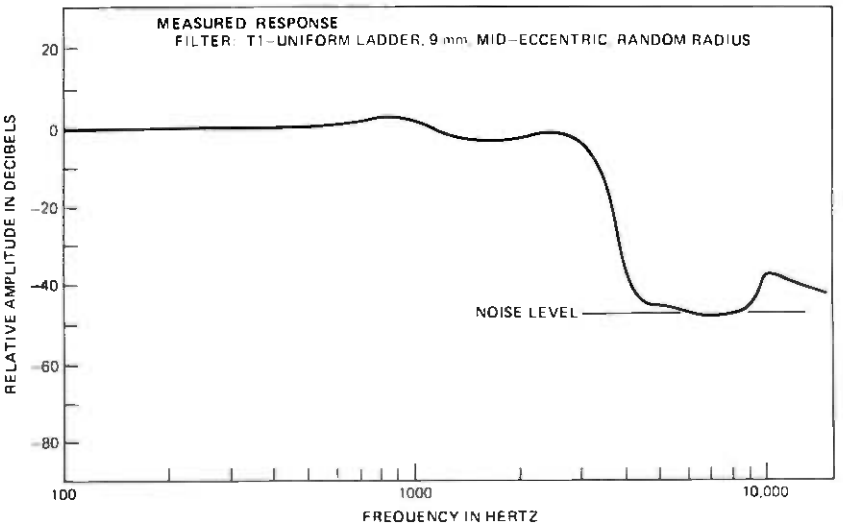

Fig. 24—Filter response only for Fig. 23.

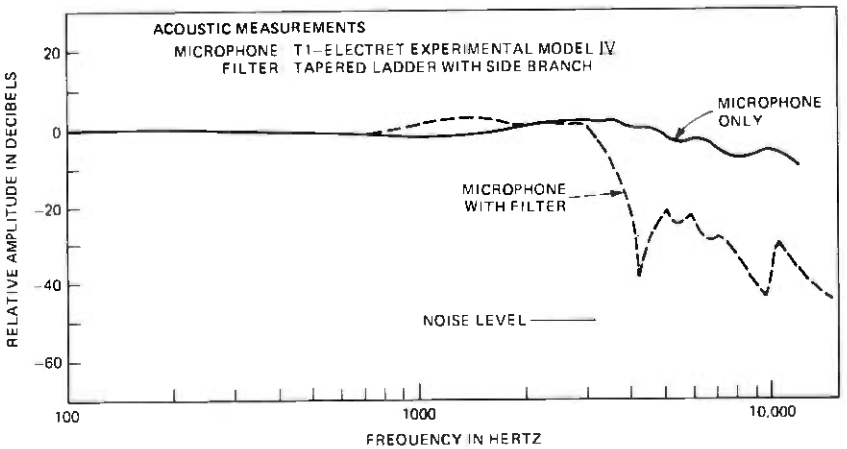

Fig. 25—Measured response of tapered ladder filter and its microphone.

The transmission zero, provided by the side branch resonator, falls approximately at the design frequency, 4000 Hz. The "recovery" in response following the zero is predicted from the lumped constant theory, but the relatively modest peak in response near 10,000 Hz is with high probability the (0, 0, 1) mode of the inner cavity.

7.3 Measured responses— EL-2 uniform ladder

Because of the smaller dimensions of the EL-2 electret microphone, short wavelength effects are substantially less bothersome, although they are not altogether absent. We implemented this filter only with the prescribed silk-screen damping in the inertive apertures. No additional cavity damping was included.

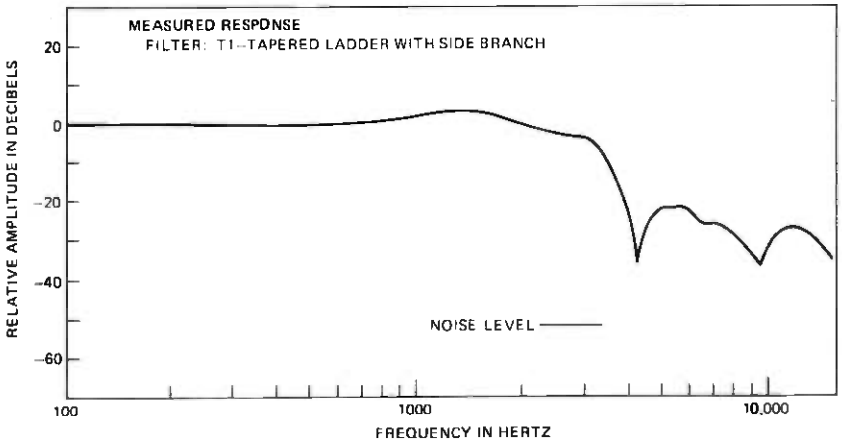

Fig. 26—Response of tapered ladder filter only.

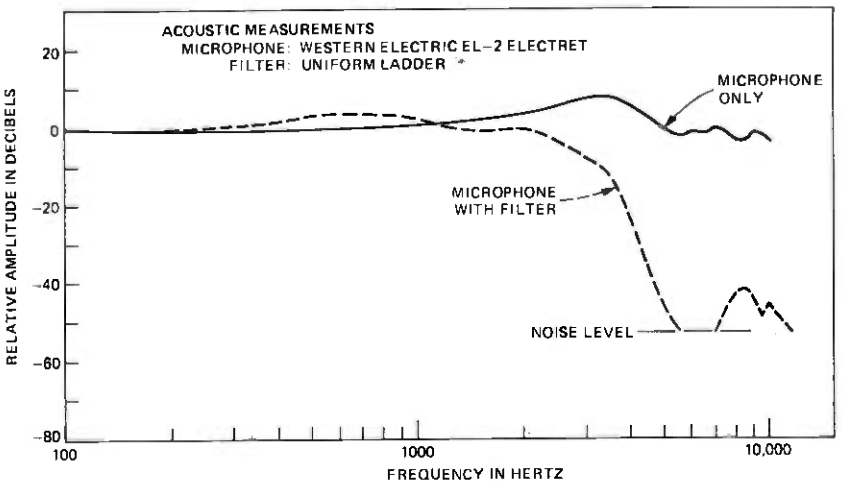

Fig. 27—Measured response of EL-2 uniform ladder and its microphone.

The EL-2 responses are shown in Figs. 27 and 28. From eq. (20), the expected mode structure can be estimated. If the length (z-dimension) of the total cavity is taken as $(3 \times 7) = 21$ mm,* together with the width and height 17.5 and 11.5 mm, respectively, the rectangular modes from eq. (20) are as shown in Table III.† The eigenfrequencies are, as previously indicated, $f = [(f_x)^2 + (f_y)^2 + (f_z)^2]^{1/2}$. The total length ($z$-direction) mode (0, 0, 1) and the first x-direction mode (1, 0, 0) appear to have correlates in the measured response. Even so, and

* This length is, of course, partitioned by the apertures.
† If l is taken only as the individual cavity length, the (0, 0, 1) mode is 24, 286 Hz.

Table III

Mode number	Frequency (hertz)		
n	f_x	f_y	f_z
0	0	0	0
1	9,714	14,783	8,095
2	19,428	29,566	48,571

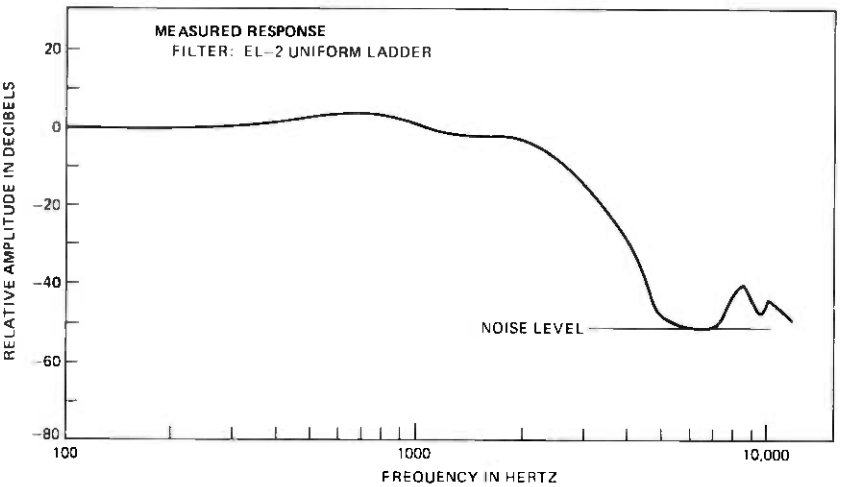

Fig. 28—Response of EL-2 uniform ladder only.

with only the serial resistor (silk-screen) damping, the out-of-band rejection is held at −40 dB.

VIII. COMPARISON OF THEORETICAL AND MEASURED RESPONSES

The measured response for the uniform ladder is best exemplified by the El-2 and T1 designs. Measured responses compared to the computed response based only on one-dimensional sound propagation are shown in Figs. 29a and 29b.

The same comparison for the T1-size tapered ladder with side branch is shown in Fig. 30. To the extent that the one-dimensional design assumptions apply, the agreement appears satisfactory.

IX. COMPARISON OF MEASURED FILTER RESPONSES TO D-CHANNEL BANK SPECIFICATIONS

Specifications of D-channel banks band-limits for voice digitization (at least, as of October 1976)[1] are shown in Fig. 31. The tolerances are quite small—unrealistically so in terms of the variability in amplitude response of mass-produced telephone transmitters (and also in terms of the variability introduced by directional effects of the sound

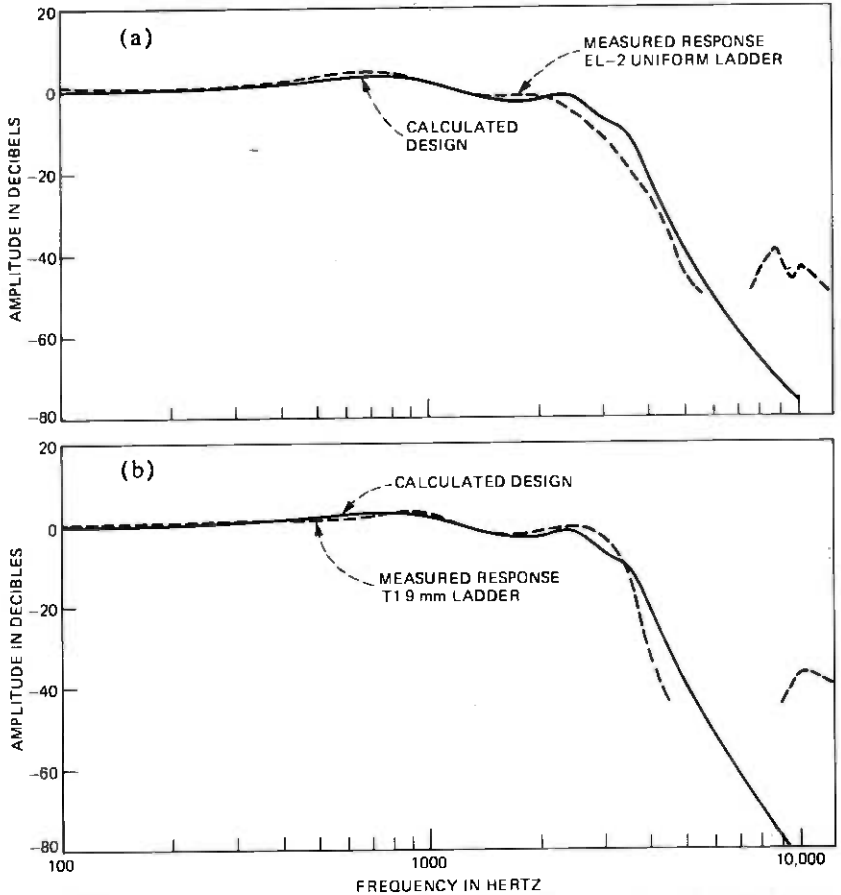

Fig. 29—Comparison between calculated design and measured response for (a) the EL-2 and (b) the T1 uniform ladder acoustic filter.

source).* Nevertheless, we wish to see how closely we can approximate this characteristic with acoustic filters only.

The response of the T1-size uniform ladder with 9-mm bore is shown in Fig. 32. This comparison is for the filter response only, and assumes that it is used with a flat (uniform) response microphone.

The T1-size tapered ladder filter response is shown in Fig. 33. This response does not satisfy the D-channel bank limits, but needs some additional amount of attenuation at the higher frequencies. For example, increasing the order of the filter by two (by adding one more resonator section) would give an out-of-band rejection satisfactory to the specifications.

* These tolerances are implied, at least in part, by transmission objectives for multiple tandeming of voice circuits.

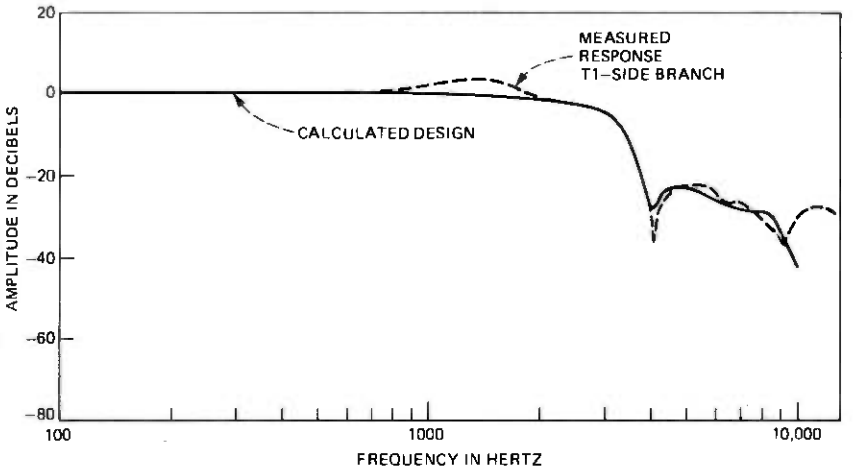

Fig. 30—Comparison between calculated design and measured response for the T1-tapered ladder filter.

The uniform ladder filter, used in combination with the Western Electric EL-2 electret microphone, does a passably good job of approximating the D-channel bank specification. This response is shown in Fig. 34. Some further adjustment of the design and of the damping might make the fit even closer.

X. CONCLUSION

This study has put forward the suggestion that a large part, or even all, of the band limitation required for digitization of acoustic signals can be accomplished by relatively simple acoustic filters. Moreover, the acoustic filters can be used as an appliqué to the signal transducer, both for transmission and reception. In a highly economical form, the filters can be implemented as part of the transducer housing—injection molded as part of the transmitter cap in a conventional telephone handset, or stamped as part of the transducer cover in other cases.

The study also establishes straightforward design theory for voice-band acoustic filters. Further, it shows how one-dimensional wave treatment and lumped characterization, if prudently applied, give computationally convenient guideposts for implementing the physical filters.

Finally, the design procedure is applied to electret microphones of the T1 size and the Western Electric model EL-2 size. The expected frequency responses of the designs are computed, and the physical filters are machined in the model shop. These prototypes are set up in the anechoic chamber, and their frequency behavior is measured. The results demonstrate that relatively simple acoustic structures can approximate the D-channel bank filter specifications for voice digiti-

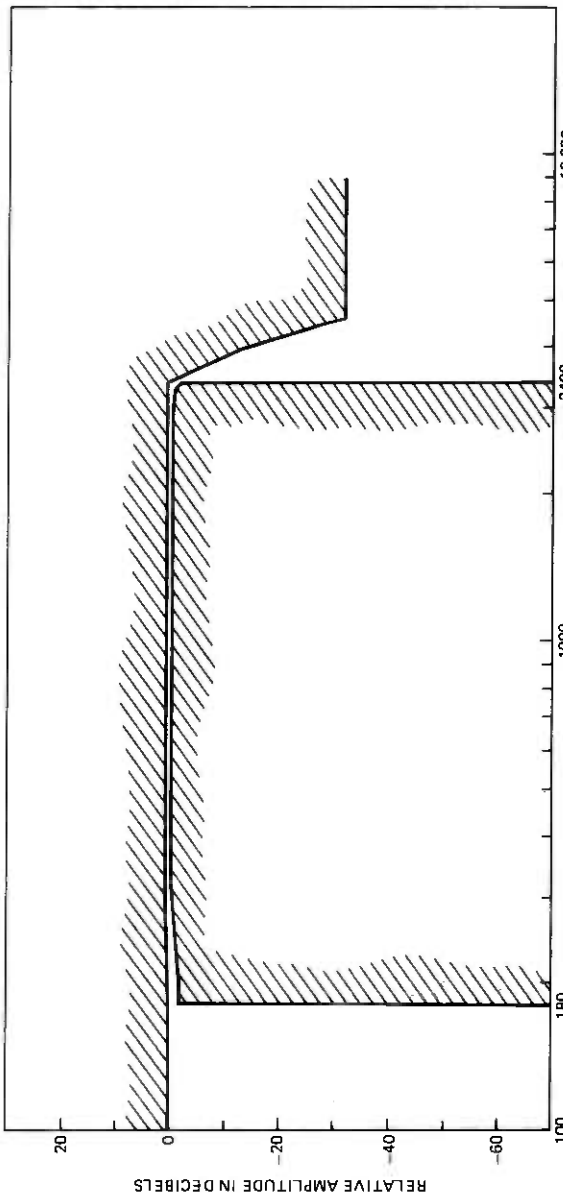

Fig. 31—Amplitude vs frequency response specification for D-channel bank band limitation [October 1976 (Ref. 1)].

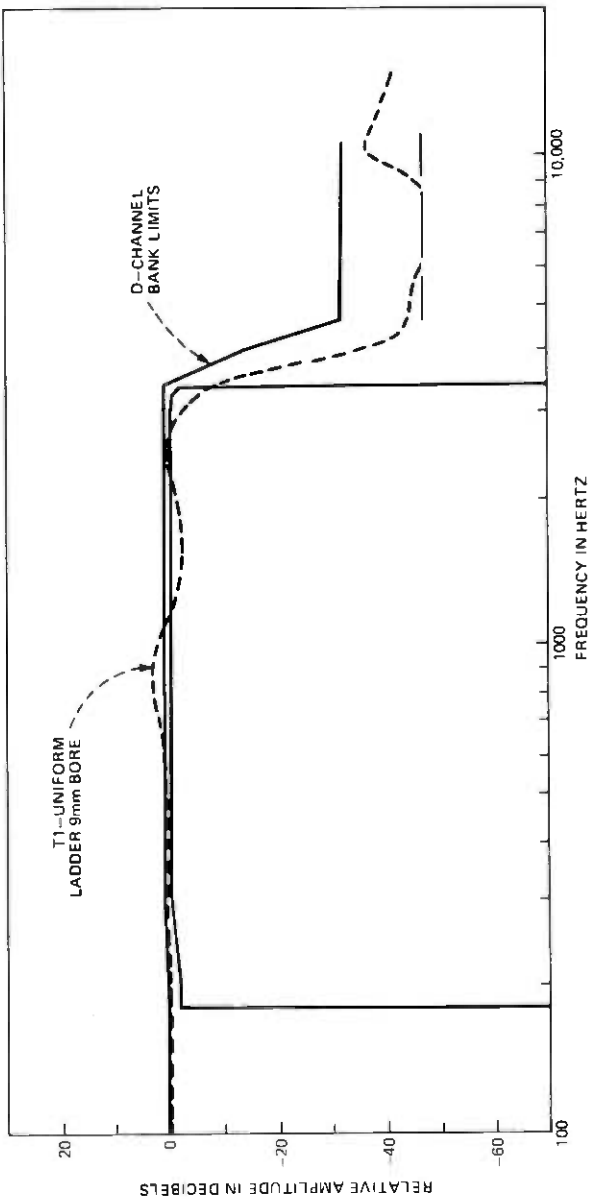

Fig. 32—Comparison of 9-mm uniform ladder response to D-bank specification.

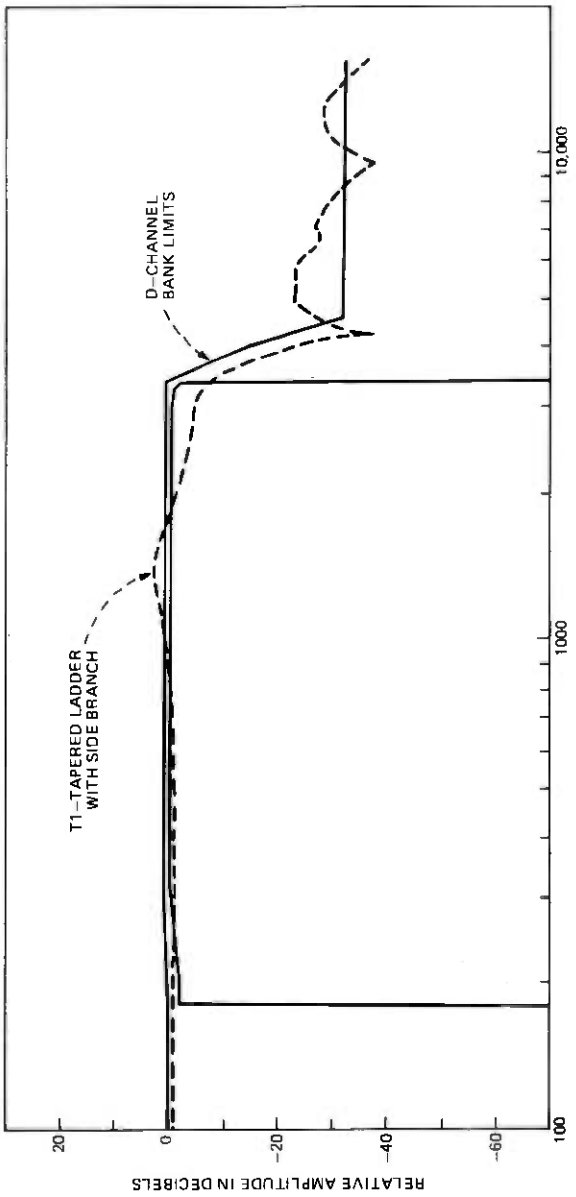

Fig. 33—Comparison of tapered ladder response to D-bank specification.

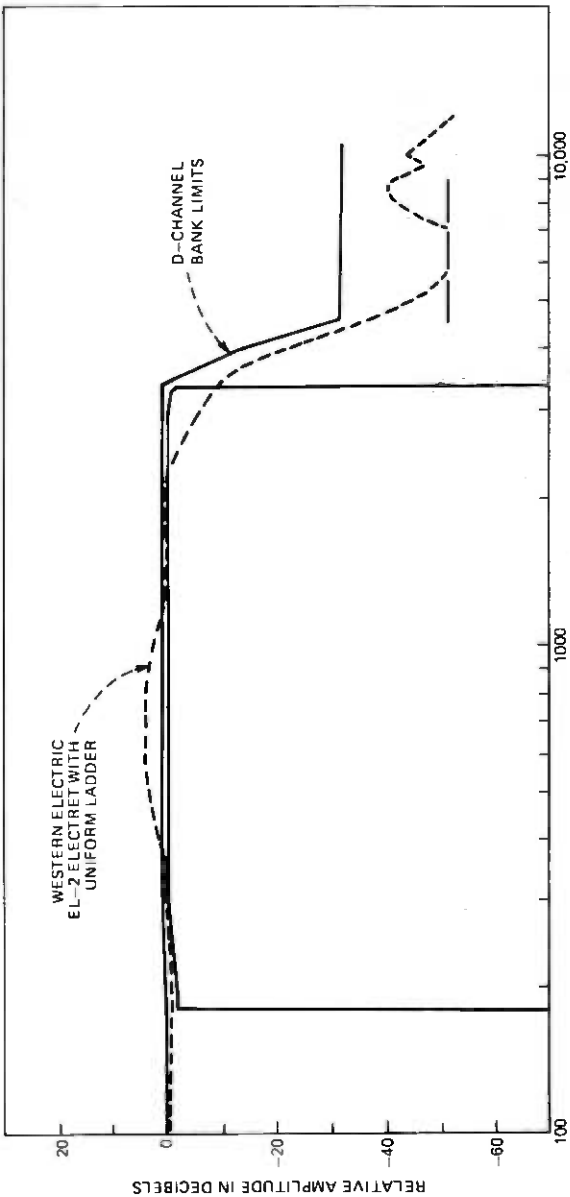

Fig. 34—Comparison of the EL-2 uniform ladder acoustic filter response to the D-channel bank filter specification.

Fig. 35—Office telephone (Mod. 2565HK) with experimental acoustic filter and electret microphone installed.

zation. Tolerances in physical dimensions are comfortable, and are virtually the same as in the elements of the electrical counterpart. Informal real-telephone testing of the prototypes lends additional confidence to the conclusions.*

Therefore, for the digitization of voice, and other acoustic signals as well, the use of band-limiting acoustic filters appears feasible and potentially attractive. The filters are simple, are highly linear, require no power, have no moving parts, and are inexpensive. They are only filled with air.

XI. ACKNOWLEDGMENTS

I thank J. West and R. Kubli of the Acoustics Research Department for giving me laboratory instruments to make the experimental measurements described in Section VII. I thank machinist Herman Stern for fabricating the several prototype filter models described in Section VI. And I thank my son James for helping me make the free-field measurements in the anechoic chamber.

REFERENCES

1. C. R. Baugh, unpublished work.
2. Unpublished experimental data, Bell Laboratories Branch Laboratory, Indianapolis.
3. P. M. Morse and U. Ingard, *Theoretical Acoustics*, New York: McGraw-Hill, 1968.
4. J. L. Flanagan, *Speech Analysis, Synthesis and Perception*, 2nd ed. New York: Springer Verlag, 1972.

* The author has used the 7.5-mm, T1-uniform filter in his office telephone for the past several months. The filter and an experimental T1-size electret transmitter are shown in Fig. 35.

THE BELL SYSTEM TECHNICAL JOURNAL
Vol. 58, No. 4, April 1979
Printed in U.S.A.

Effect of Temperature on Transmission in Lightguides

By L. G. COHEN and J. W. FLEMING

(Manuscript received November 21, 1978)

Temperature effects on refractive index have been studied by monitoring pulse propagation delays in fiber-optic lightguides for temperatures between −40 and 67°C. Loss and dispersion properties did not change significantly from their room temperature values.

I. INTRODUCTION

Lightguides may be used for transmission in a variety of environments. The temperature of these environments may vary as a function of time. It is anticipated that optical waveguides will have an operating temperature range specification similar to that of cables currently being employed for telephony, which is −40 to +85°C. Variation within this temperature range causes changes in the optical properties of materials comprising the lightguide.

To maximize the signal-carrying capacity of lightguides, the refractive-index profile of multimode lightguides is carefully engineered to a specific shape. This is done to minimize mode dispersion. The refractive-index difference between core and cladding of a single-mode fiber must be controlled to provide a fiber which supports only the fundamental mode.

It is known that refractive-index dispersion is a function of temperature. In glasses such as those from which optical waveguides are currently being fabricated, two opposing factors regulate the direction and magnitude of the refractive-index variation with temperature, δn. As the material temperature increases, the positive coefficient of thermal expansion in glasses causes a decrease in density which decreases the refractive index. However, with an increase in the temperature, the other factor, electron polarizability, is increased and the ultraviolet absorption bands are shifted to a longer wavelength. This contributes to an increase in refractive index.[1–3]

In silicate glasses, electron polarizability dominates, and δn is positive below the glass transition temperature. But the magnitude can vary by a factor of ten or more as a function of glass composition.[4] The range of δn is approximately $1 - 20 \times 10^{-6}$ per °C in silicate glasses.

The refractive-index difference between core and cladding in a multimode optical waveguide with an NA of 0.2 is about 1.5×10^{-2}. Conceivably, the refractive-index difference could be changed by 10 percent within the operating temperature range previously mentioned if the difference in δn between the core and cladding glasses was 15×10^{-6} per °C, a possible figure. In single mode lightguides, Δn is roughly 1×10^{-3}. The change in Δn with temperature in this case could be 100 percent of the manufactured value. Obviously, this could be serious if the deviation were negative.

Since the glass compositions comprising the core and cladding of most lightguides are similar (80 mole percent silica), it was not expected that δn would be significantly different. For silica, δn is roughly 10×10^{-6} per °C and varies slightly with wavelength. But there are additional considerations that complicate any calculation of refractive-index variations. For example, as the temperature is changed, the stresses between the different compositions comprising the fiber core and cladding also change. This effect could influence the electron polarizability and density variations. Such possibilities suggested direct examination of the variation with temperature of pulse propagation in multimode and single-mode fibers to discern the significance of the temperature effect at the anticipated transmission wavelength.

II. EXPERIMENTAL

The fiber specimens examined were representative single-mode and multimode (GRIN, graded index) fibers with borosilicate (B_2O_3-SiO_2) cores and claddings and multimode (GRIN) fibers with germania borosilicate (GeO_2-B_2O_3-SiO_2) cores and silica (SiO_2) claddings. All were considered representative of fibers currently being used or strongly considered for use in optical communications systems. To eliminate externally induced mode-mixing effects, the specimens were coiled loosely with 30- to 40-cm diameters on individual aluminum trays.

The fibers that were analyzed individually were placed in a "Blue M" environmental control chamber modified to provide ambient temperatures in the chamber from −50 to +85°C.

The two ends of each fiber were run from the chamber through two 0.6-cm ports and aligned with the shuttle pulse analysis system.[5] The temperatures on and above the fiber holding tray were monitored by five systematically placed copper-constantan thermocouples. After the fiber and thermocouples were in place, the chamber was either heated to about +70°C or cooled to about −40°C. From this temperature

extreme, the chamber was either monotonically cooled or heated respectively at about 1.5°C per min. The temperature of the chamber was held at −40°, 0°, +30°, and +70°C long enough for the temperature of the chamber to equilibrate and to allow a measurement of the pulse delay and shape to be made. The temperature gradient across the tray did not exceed 5°C at any temperature during measurement.

Figure 1 qualitatively illustrates refractive-index profiles corresponding to fiber specimens. Borosilicate fibers are fabricated with a uniform borosilicate (B_2O_3-SiO_2) cladding composition and a core in which the B_2O_3 dopant concentration decreases from its cladding concentration to a smaller percentage at the core center. The addition of B_2O_3 decreases the refractive-index of SiO_2 by $\Delta n \sim 0.008$ in the cladding. The maximum refractive index at the core center corresponds to pure silica as in Fig. 1a for multimode fibers (diameter ~50 μm) and Fig. 1b for small-core (diameter ~5 μm), single-mode fibers. In more common single mode fibers like Fig. 1c, the core diameter is approximately 10 μm and $\Delta n \sim 0.0015$. Germania borosilicate fibers are fabricated by

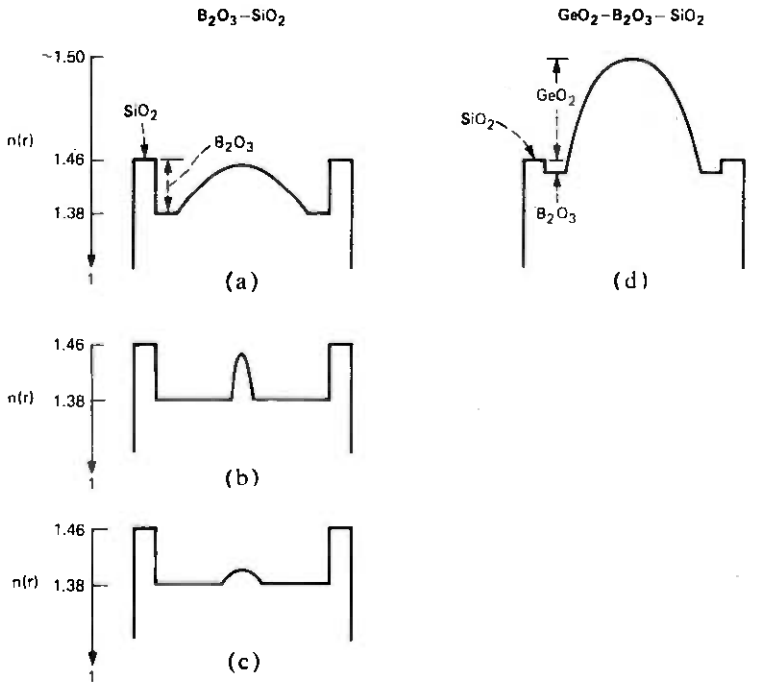

Fig. 1—Refractive-index profiles of fiber specimens. (a) B_2O_3-SiO_2 multimode GRIN (graded index) fiber with nearly pure silica core center, diameter ~50μm, $\Delta n \sim 0.008$. (b) B_2O_3-SiO_2 small core single mode fiber with nearly pure silica core center, diameter ~5μm, $\Delta n \sim 0.007$. (c) B_2O_3-SiO_2 large core single mode fiber with borosilicate core center, diameter, ~10μm, $\Delta n \sim 0.0015$. (d) GeO_2-B_2O_3-SiO_2 multimode GRIN fiber with germania borosilicate core center, diameter ~50 μm, $\Delta n \sim 0.014$.

depositing two borosilicate layers followed by a gradually increasing amount of GeO_2 towards the core center. Multimode fibers like Fig. 1a have 50-μm diameters and $\Delta n \sim 0.014$.

Refractive-index variations, δn, with environmental temperature, T, can be sensitively determined by monitoring the change in pulse propagation delay,

$$\frac{\delta \tau}{\delta T} = \frac{1}{c}\left[\frac{\delta n}{\delta T} L + n \frac{\delta L}{\delta T}\right],$$

through a fiber. The propagation delay change, $\delta\tau$, occurs because both refractive index, δn, and fiber length, δL, change with temperature. The fiber length change with temperature can be expressed as $\delta L/\delta T = \alpha L$, where $\alpha \approx 8 \times 10^{-7}$ per °C is the thermal expansion coefficient for the combined fiber core and cladding. Malitson's results[6] for bulk-fused silica specimens indicate that $\delta n/\delta T \approx 1 \times 10^{-5} \gg \alpha$. Therefore, propagation delay changes in doped fused silica fibers should be primarily due to the refractive-index variation with temperature expressed by $\delta\tau \approx \delta n L/c$. Figure 2 summarizes results for several fiber specimens by plotting $\delta\tau$ versus T. Borosilicate-clad fibers 1 and 2 had profiles like Figs. 1a and 1b with nearly pure silica core centers. Their material properties should correspond to pure silica. Transmission pulse delay changes were monitored to be $\delta\tau(S) \sim 36$ ps per Km per °C, which corresponds to a refractive-index change $\delta n(S)/\delta T \sim 1 \times 10^{-5}$ per °C. This is in good agreement with a value obtained on bulk-fused silica specimens by Malitson.[6] Borosilicate fiber 3 had a profile like Fig. 1c with a large, 14 mole percent B_2O_3 dopant concentration at the core center. Its material properties appear to be significantly different from those of pure silica curves and fiber 2 since $\delta\tau(BS) \sim 65$ ps per Km per °C corresponds to a refractive-index change $\delta n(S) \sim 1.8 \times 10^{-5}$ per °C. Germania borosilicate fibers 4, 5 had profiles like Fig. 1d with a 14 mole percent GeO_2 dopant concentration at the core center. Their thermal material properties are similar to those of pure silica since $\delta\tau(\text{GBS}) \sim 33$ ps per Km per °C, which correspond to $\delta n(\text{GBS}) \sim 0.91 \times 10^{-5}$ per °C.

Thermal effects on lightguide transmission properties can be estimated from refractive-index versus temperature properties deduced from Fig. 2. Pulse dispersion properties are related to the change of $\Delta n = [n(\text{core}) - n(\text{clad})]$ with temperature. Graded-index multimode borosilicate fibers have a nearly pure silica core center and a borosilicate cladding. Therefore, $\delta(\Delta n) = 0.8 \times 10^{-5}$ per °C can be estimated from delay differences between curves 3 and 1, 2. The maximum core-to-cladding refractive-index difference should be $\Delta n \sim 0.008 \pm 0.00032$ for a ±50°C variation about room temperature. This ±4-percent maximum variation means that refractive-index changes between succes-

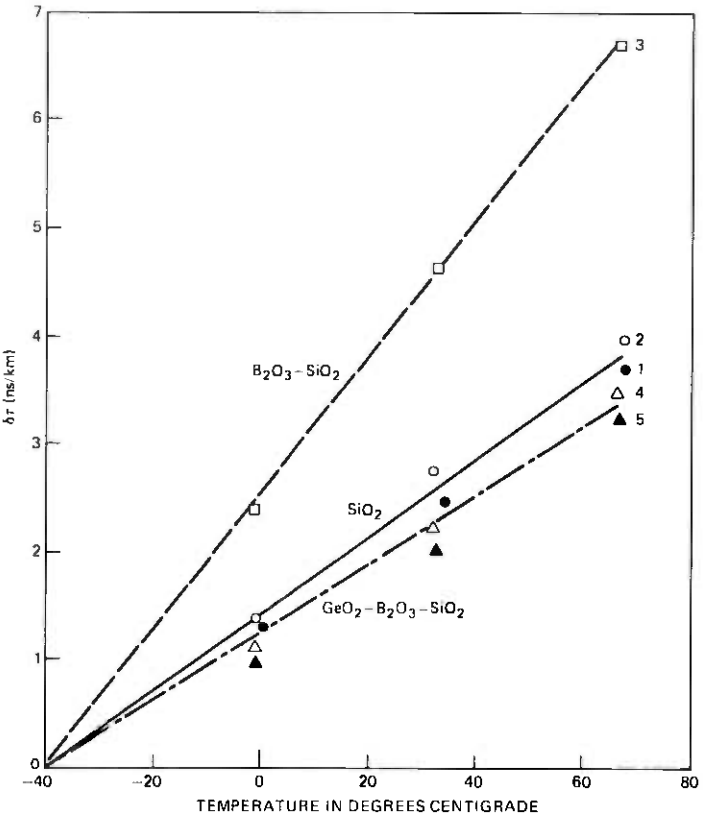

Fig. 2—Pulse propagation delay change, $\delta\tau$ vs environmental temperature, T. Fibers 1, 2, 3, and 4–5 have profiles corresponding to Figs. 1b, 1a, 1c, and 1d, respectively.

sively deposited core layers should not significantly affect the shape of the fiber's graded-index profile. The temperature dependence of Δn in a multimode germania borosilicate fiber, deduced from delay differences between curves 3 and 4, 5 in Fig. 2 are even less than for borosilicate clad fibers. Therefore, dispersion properties of multimode borosilicate and germania borosilicate fibers should not be significantly affected by environmental temperature changes.

Thermal effects on transmission properties of borosilicate single mode fibers can also be estimated from Fig. 2. Single mode fibers 2, 3 are characterized by a parameter $V = (\pi/\lambda)\sqrt{2n\Delta n} \sim 2.3$ at $\lambda = 0.908$ μm. Only one mode propagates as long as $V < 2.41$. Fiber 2 has a nearly pure silica core and a borosilicate cladding. Its V number variation with temperature is less than ±2 percent for a ±50°C variation about room temperature. This change is very small and should not signifi-

cantly affect attenuation or waveguide dispersion. The only cause for concern might be if the V number at the signal wavelength were within ±2 percent of the cut-off V number of the LP_{11} mode. In that case, the fiber could change from single-mode to two-mode operation. Single-mode fiber 3 has a $\Delta n \sim 0.0015$ index difference between its borosilicate core and cladding. Temperature-dependent material differences are insignificant between its core and cladding.

Deductions based on Fig. 2 were confirmed by measurements of pulse dispersion and attenuation as a function of temperature. The optical shuttle pulse technique was used to improve measurement precision by extending fiber specimen lengths by an order of magnitude.[5] Intermodal pulse dispersion changed by less than 0.04 ns per km for a temperature variation between −40°C and 67°C. This change is small both in an absolute sense and when compared to the total 0.2 ns per km dispersion observed in the borosilicate graded-index fibers and 0.38 ns per km dispersion observed in the germania borosilicate fibers. Attenuation in the single-mode fibers changed by less than 0.2 dB per km.

III. CONCLUSIONS

The temperature dependence of refractive-index in fiber optic lightguides has been studied within a −40°C to 67°C range. Pulse delay measurements indicate that the core center refractive-index changes by $\delta n(S) \sim 1 \times 10^{-5}$ per °C in fibers with nearly pure fused silica core centers, by $\delta n(BS) \sim 1.8 \times 10^{-5}$ per °C in fibers with borosilicate (B_2O_3-SiO_2) core centers, and by $\delta n(\text{GBS}) \sim 0.9 \times 10^{-5}$ per °C in fibers with germania borosilicate (GeO_2-B_2O_3-SiO_2) core centers. Core-to-cladding refractive-index differences change by a very small amount, $\delta(\Delta n) < \pm 0.00032$ for a ±50°C variation about room temperature. No significant changes in loss or pulse dispersion characteristics were observed after propagation through multikilometer fiber lengths. This implies that fiberguide system properties will not be significantly affected by environmental temperature effects on refractive index.

IV. ACKNOWLEDGMENTS

We are grateful to D. L. Bisbee, F. V. DiMarcello, W. G. French, and P. Kaiser for fabricating the fibers used in this study.

REFERENCES

1. R. B. Sosman, "The Properties of Silica," New York: Chemical Catalog Co. (Reinhold Publishing Corp.), 1927.
2. L. Prod'homme, "A New Approach to the Thermal Change in the Refractive Index of Glasses," Phys. and Chem. of Glasses, *1*, No. 4 (1960), pp. 119–22.
3. T. Baak, "Thermal Coefficient of Refractive Index of Optical Glasses," J. Opt. Soc. Amer., *59*, No. 7 (1969), pp. 851–7.

4. C. J. Parker and W. A. Papov, "Experimental Determination of the Effect of Temperature on Refractive Index and Optical Path Length of Glass," Appl. Opt., 10, No. 9 (1971), pp. 2137–43.
5. L. G. Cohen, F. V. DiMarcello, J. W. Fleming, W. G. French, J. R. Simpson, and E. Weiszmann, "Pulse Dispersion Properties of Fibers with Various Material Constituents," B.S.T.J., *57*, No. 5 (May–June 1978), pp. 1653–1662.
6. I. H. Malitson, "Interspecimen Comparison of the Refractive Index of Fused Silica," J. Opt. Soc. Amer., *55*, No. 10 (1965), pp. 1205–9.

Contributors to This Issue

Harry W. Astle, A.A.S., 1966, Hartford State Technical College, Bell Laboratories, 1966–1978. Mr. Astle first worked with optical gas lenses and was engaged in the fabrication and evaluation of optical fibers. He is currently with the Singer Company, Binghamton, N.Y.

David A. Berkley, B.E.E., 1961, Ph.D. (Applied Physics), 1966, Cornell University; Bell Laboratories, 1968—. Upon joining Bell Laboratories, Mr. Berkley initially worked in nonlinear speech signal processing and hearing research. He is presently supervisor of the Electroacoustics and Acoustic Signal Processing Group. He is currently conducting research in the areas of small room acoustics, reverberation reduction, echo control, conference telephony, and transducers. Member, Acoustical Society of America, AAAS, Eta Kappa Nu, Tau Beta Pi.

L. M. Boggs, B.S. (E.E), 1963, Clemson University; M.S. (E.E.), 1965, Georgia Institute of Technology; Lockheed-Georgia Company Research Center, 1963–1971; Western Electric, 1971—. Mr. Boggs has worked on the development of electronic and optical systems applicable to aircraft manufacture and operation. He has developed several measurement systems used in the manufacture of communication cable. Most recently, he has been responsible for the development of measurement equipment for characterizing lightguide cable products.

Leonard G. Cohen, B.E.E., 1962, City College of New York; Sc.M., 1964, and Ph.D. (Engineering), 1968, Brown University; Bell Laboratories, 1968—. At Brown University, Mr. Cohen was engaged in research on plasma dynamics. At Bell Laboratories, he has concentrated on optical fiber transmission studies. Member, Sigma Xi, Tau Beta Pi, Eta Kappa Nu; senior member, IEEE.

James L. Flanagan, B.S. (Electrical Engineering), 1948, Mississippi State University; S.M., 1950, and Sc.D., 1955, Massachu-

setts Institute of Technology; Bell Laboratories, 1957—. Mr. Flanagan has specialized in voice communications, digital techniques, and engineering acoustics. He is Head of the Acoustics Research Department. Fellow, IEEE; Fellow and currently President, Acoustical Society of America; Tau Beta Pi, Sigma Xi; Member, National Academy of Engineering.

James W. Fleming, B.S., 1970 and M.S. 1971 in Cer. E., University of Missouri at Rolla; Research Associate, University of Missouri, 1971–1972; Bell Laboratories, 1972—. Mr. Fleming has worked on the design and properties of PTCR thermistors and other polycrystalline materials for communication applications. Since 1973, he has been developing techniques for the preparation of high melting oxide glass compositions such as those used in lightguides and examining the properties of these glasses. He is currently involved in analysis of dispersion in optical materials and characterizing lightguide core composition profiles. Mr. Fleming is pursuing a Ph.D. in Cer. Sci. at Rutgers University and is a member of the American Ceramic Society.

Dietrich Marcuse, Dipl. Phys., 1954, Berlin Free University; D.E.E., 1962, Technische Hochschule, Karlsruhe, Germany, Siemens and Halske (Germany), 1954–1957; Bell Laboratories, 1957—. At Siemens and Halske, Mr. Marcuse was engaged in transmission research and studying coaxial cable and circular waveguide transmission. At Bell Laboratories, he has been engaged in studies of circular electric waveguides and work on gaseous masers. He spent one year (1966–1967) on leave of absence from Bell Laboratories at the University of Utah. He is presently working on the transmission aspect of a light communications system. Mr. Marcuse is the author of three books. Fellow, IEEE; fellow, Optical Society of America.

Gerry Miller, B.E.S., 1963, Ph.D., 1969, Johns Hopkins University; Bell Laboratories, 1969—. Mr. Miller is a member of the Interconnection Performance Planning Department and is currently involved in planning for operational compatibility at equipment-to-equipment interfaces. He has worked on the development of longitudinal balance and signal power requirements for voiceband terminal equipment. Member, Tau Beta Pi, Eta Kappa Nu, Sigma Xi.

F. W. Mounts, E.E., 1953, M.S., 1956, University of Cincinnati; Bell Laboratories, 1956—. Mr. Mounts has been concerned with research

in efficient methods of encoding pictorial information for digital television and graphics systems. Member, Eta Kappa Nu; Senior Member, IEEE.

Arun N. Netravali, B. Tech. (Honors), 1967, Indian Institute of Technology, Bombay, India; M.S., 1969, and Ph.D. (E.E.), 1970, Rice University; Optimal Data Corporation, 1970–1972; Bell Laboratories, 1972—. Mr. Netravali has worked on problems related to filtering, guidance, and control of the space shuttle. At Bell Laboratories, he has worked on various aspects of signal processing, and is presently Head of the Visual Communication Research Department. He is also an adjunct professor of Electrical Engineering at Rutgers University. Member, Tau Beta Pi, Sigma Xi; Senior Member, IEEE.

Herman M. Presby, B.A., 1962, and Ph.D., 1966, Yeshiva University; Research Scientist, Columbia University, 1966–1968; Assistant Professor Physics, Belfer Graduate School of Science, Yeshiva University, 1968–1972; Bell Laboratories, 1972—. Mr. Presby is engaged in the studies on the properties of optical fiber waveguides.

Lawrence R. Rabiner, S.B. and S.M., 1964, Ph.D. (electrical engineering), Massachusetts Institute of Technology; Bell Laboratories, 1962—. From 1962 through 1964, Mr. Rabiner participated in the cooperative plan in electrical engineering at Bell Laboratories. He worked on digital circuitry, military communications problems, and problems in binaural hearing. Presently, he is engaged in research on speech communications and digital signal processing techniques. He is coauthor of *Theory and Application of Digital Signal Processing* (Prentice-Hall, 1975) and *Digital Processing of Speech Signals* (Prentice-Hall, 1978). Former President, IEEE G-ASSP Ad Com; former Associate Editor, G-ASSP Transactions; former member, Technical Committee on Speech Communication of the Acoustical Society. Member, G-ASSP Technical Committee on Speech Communication, IEEE Proceedings Editorial Board, Eta Kappa Nu, Sigma Xi, Tau Beta Pi. Fellow, Acoustical Society of America and IEEE.

Carolyn E. Schmidt, B.S. (Mathematics), 1974, Lafayette College; Bell Laboratories, 1974—. Miss Schmidt is a member of the Acoustic Research Department and is currently involved in work on speech communications. Member, Phi Beta Kappa.

Thomas C. Spang, B.E., 1956, M.E., 1958, and D. Eng., 1961, Yale University; Bell Laboratories, 1960—. Mr. Spang has been responsible for systems engineering studies to establish recommendations for the public and private networks. Currently, he supervises a group concerned with registration and performance standards in the Interconnection Performance Planning Department.

Kenneth A. Walsh, A.A.S. (E.E.), Kent State University, Salem, Ohio, 1969; Bell Laboratories, 1969—. Mr. Walsh's work has been mainly concerned with the investigation of efficient digital coding techniques, using both hardware and software methods, with application to video and facsimile transmissions.

Papers by Bell Laboratories Authors

BIOLOGY

High Efficiency and Low Noise Power Conditioning Equipment for Millimeter Waveguide Repeaters. J. W. Osmun and H. Stocker, Institute of Environmental Sciences, Proceedings Inst. Environ. Sci., (April 1978), pp. 477–480.

COMPUTING

Derivation Protection in Data Base Systems. David Cohen and M. T. Liu, Information Technology, Proceedings of the 3rd Jerusalem Conference on Information Technology, (August 6, 1978), pp. 165–169.

Event Driven Protection to Enhance Data Sharing in Data Base Systems. David Cohen and M. T. Liu, Databases: Improving Usability and Responsiveness, Academic Press (August 2–4, 1978), pp. 411–431.

ELECTRICAL and ELECTRONIC ENGINEERING

Atmospheric Corrosion Testing of Connectors—A New Accelerated Test Concept. F. E. Bader, S. P. Sharma, and M. Feder, Proceedings Ninth International Conf. on Electric Contact Phenomena, (September 11, 1978), pp. 341–351.

Bonded Gold Fingers as a Low-Cost Alternative to Patterned Edgeboard Fingers for General PNB Use. V. L. Brown, Proceedings 1978, 28th Electronic Components Conference, (April 24, 1978), pp. 121–128.

The Chicago Developmental Cellular System. D. L. Huff and J. T. Kennedy, 28th IEEE Veh. Technol. Conf. Rec., Denver, Co., (March 22, 1978), pp. 66–72.

Cleaning Photomasks with Scrubbers and High-Pressure Water. W. H. Kroeck, R. F. Doll, and E. L. Stokes, Circuits Manufacturing, (June 1978), pp. 16–21.

Contact Finish Design Experiments: Contact Resistance of Gold Plated Copper and Nickel Substrates Exposed to Tarnishing Environments. G. J. Russ and R. J. Chesseri, Proc. Ninth Int. Elec. Contact Phenomen. 24th Ann. Holm Elec. Contacts, Conf., (September 1978), pp. 227–233.

Current Distribution Leveling Resulting from Auxiliary Bipolar Electrodes. W. Engelmaier, T. Kessler, and R. Aikire, J. Electrochem. Soc., *125* No. 2, (1978), pp. 209–216.

Detector and Receivers for Optical Fiber Applications. R. G. Smith, Proceedings of the International Symposium on Circuits and Systems, *1* (May 1978), pp. 20–24.

Determination of Flex Circuit Ductility and Fatigue Behavior. W. Engelmaier, NEPCON 1978 Proceedings, Anaheim, Cal., (1978), pp. 141–149.

Diffusion Effects of the Heat Treatment of Gold-Silver on Iron-Nickel Dry Sealed Reeds. C. A. Haque, Proc. Ninth Int. Elec. Contact Phenom. Conf., (September 15, 1978), pp. 605–609.

Dimensional Changes During Multilayer Board Processing. M. U. Rao, R. R. Holmes, and M. M. Doswell, Proc. First Print. Ckt. World Conv., London, England, (June 1978), *1*, pp. 1.19.1–1.19.10.

Encapsulation of Large Beam Leaded Devices. N. A. Soos and D. Jaffe, Proc. Electron. Compon. Conf., (April 1978), pp. 213–216.

Fatigue Failure of Encapsulated Gold-Beam Lead and TAB Devices. J. L. Dais and F. L. Howland, IEEE Trans. Compon. Hybrids, (June 1978), pp. 158–166.

A Field Study of the Electrical Performance of Separable Connectors. T. G. Grau, Proc. 28th Electron Compon. Conf., (April 1978), pp. 102–115.

The Four-Point Bend Test for Measuring the Ductility of Brittle Coating. C. C. Lo, J. Electrochem. Soc. *125* (March 1978), pp. 400–403.

Frequency Stability of Dielectric Resonator Oscillators. J. K. Plourde, 1978 Int. Microwave Symposium Digest, (June 1978) p. 480.

Functional Testing of Positive Photoresist for Manufacture of Film Integrated Circuits. H. N. Keller, Solid State Technol. *21* No. 6, (June 1978), pp. 45–53.

A 2W, 4GHz GaAs FET Amplifier for Radio-Relay Applications. W. E. Schroeder and J. W. Gewartowski, 1978 IEEE MTT-S International Microwave Symposium Digest, *78CH 1355-7 MTT*, (June 1978), pp. 279–282.

Investigation of Agitation Effects on Electroplated Copper in Multilayer Board Plated-Through Holes in a Forced-Flow Plating Cell. W. Engelmaier and T. Kessler, J. Electrochem. Soc., *125* (January 1978), pp. 36–43.

Mobile Telephone Control Unit Design Guidelines for the High Capacity Mobile Telecommunications System. J. T. Walker, 28th IEEE Veh. Technol. Conf. Rec., Denver, Co., (March 1978), pp. 56–64.

A New Ductility and Flexural Fatigue Test Method for Copper Foil and Flexible Printed Wiring. W. Engelmaier, Institute Interconnecting Packaging Electronic Circuits. *204* (1978), pp. 1–16.

Removal of Particulate Contamination from Hard Surface Photomasks by Various Cleaning Techniques. W. H. Kroeck, R. F. Doll, and E. L. Stokes, Kodak Microelectronics Seminar Proceedings, (May 1978), pp. 26–32.

A Stability RC Circuit Using High Nitrogen Doped Tantalum. O. J. Duff, G. J. Koerckel, R. A. Deluca, E. H. Mayer, and W. Worobey, Proc. 28th Compon. Conf., (April 1978), pp. 229–233.

Theoretical Derivatives of the Electrical Characteristic of a Junction Laser Operated in the Vicinity of Threshold. T. L. Paoli, IEEE J. Quantum Electron., *14* No. 1, (1978), pp. 62–68.

Thermocompression Bondability of Bare Copper Leads. N. T. Panousis, Proc. 28th Electron. Compon. Conf., (April 24, 1978), pp. 380–386.

MATERIALS SCIENCE

A Double-Aperture Method of Producing Variably-Shaped Writing Spots for Electron Lithography. M. G. R. Thomson, R. J. Collier, and D. R. Herriott, J. Vac. Sci. Technol., *15* No. 3, (January–February 1978), pp. 891–895.

Time Dependence of the Chemical Composition of the Surface Film on the Metastable Tin-Nickel Alloy Standard with X-Ray Photoelectron Spectroscopy. K. G. Tompkins, G. K. Wertheim and S. P. Sharma, J. Vac. Sci. Technol., *15* (January–February 1978), pp. 20–23.

PHYSICS

An Assigned-Slot Listen-Before-Transmission Protocol: Dynamic Channel Control Procedures and Random Slot Assignment. L. W. Hansen and M. Schwartz, IEEE Int. Commun. Conf. Rec., *1*, (June 1978) pp. 7.1.1–7.1.6.

Bending of a Nonlinear Rectangular Beam in Large Deflection. C. C. Lo and S. DasGupta, J. Appl. Mech., *45*, (March 1978), pp. 213–215.

Effects of Beam Displacement and Front Back Mistracking of Junction Lasers CN Lightwave Transmitter Output Stability. F. S. Chen and M. A. Karr, and P. W. Shumate, Appl. Opt. *17* No. 14, (July 15, 1978) pp. 2219–2223.

Interlaminar Thermoelastic Stresses in Layered Beams. P. B. Grimado, J. Therm. Analy., *1*, (July 1978), pp. 75–86.

Lightwave Fiber Tap. M. A. Karr, T. C. Rich, and M. Di Domenico, Applied Optics, *17* No. 14, (August 1, 1978), pp. 2215–2218.

On the Effect of a Partial Sink in Binary Diffusing in Thin Films. H. G. Tompkins, J. Appl. Phys., *49* No. 1, (January 1978), pp. 223–228.

Potential Problem Areas in Beta Backscatter Measurement Technology. R. R. Buckley, First AES Symposium Thickness Testing of Surface Finishing, N.Y.C., (March 1978), pp. 1–7.

THE BELL SYSTEM TECHNICAL JOURNAL
Vol. 58, No. 4, April 1979
Printed in U.S.A.

B.S.T.J. BRIEF

MAC-4: A Single-Chip Microcomputer

By W. F. CHOW and W. W. TROUTMAN

(Manuscript received January 30, 1979)

MAC-4 is a single-chip microcomputer designed to fill a rising need in many Bell System applications. Its instruction set promotes program memory efficiency and emphasizes bit manipulation. MAC-4 is implemented in CMOS technology, resulting in a low power dissipation which can be further reduced by using a special halt instruction. These features make it valuable as a controller in a telephone environment and for telephone loop power applications. Figure 1 is a photograph of the MAC-4 chip.

The MAC-4 contains a program memory (ROM), a data memory (RAM), and many input/output (I/O) features. Both the ROM and the RAM can be expanded through a simple layout modification. The ROM can vary in size between 1024 and 3840 4-bit nibbles, while the RAM size varies between 80 and 192 nibbles.

ARCHITECTURE

MAC-4 consists of five basic functional sections: the internal control, arithmetic-logic unit, special registers and address arithmetic unit, memories, and I/O circuits. The internal control coordinates and executes the sequence of events for an instruction. The arithmetic-logic unit performs the arithmetic/logic operation. All the I/O ports and special registers are addressable in units of 4-bit nibbles. The address width is 12 bits, giving a total directly addressable space of 4096 nibbles.

The user addressable special registers consist of a 12-bit program counter, a 12-bit DMA pointer, an 8-bit stack pointer, two 8-bit memory pointers, an 8-bit processor control register, an 8-bit I/O control register, a 4-bit extended memory pointer, a 4-bit page pointer, and a

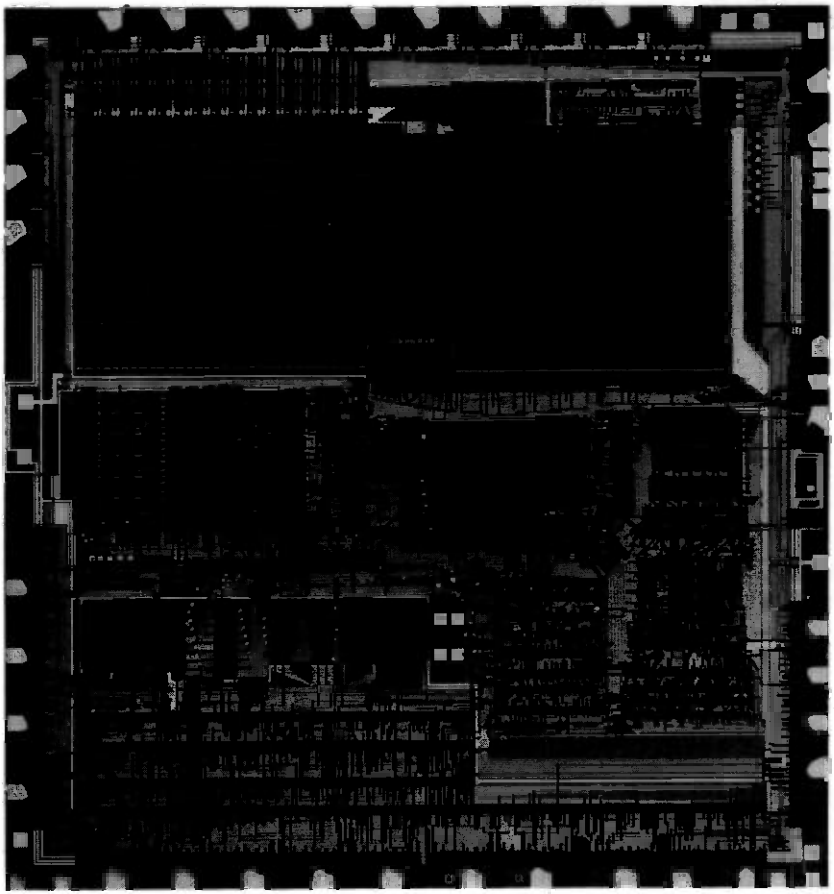

Fig. 1—MAC-4 chip.

4-bit condition register. The program counter stores the current program address. The DMA pointer stores the starting address of the data block for direct memory access operations, or as a count-up value when counting events. The 8-bit stack pointer stores the address of RAM where the return address of a routine call or an interrupt service will be stored. The two memory pointers are used to store operand addresses. The page pointer provides the middle 4-bit nibble of a 12-bit address. The 4-bit extended memory pointer is used together with other 8-bit pointers to provide the upper nibble of the 12-bit address. This offers flexibility by allowing access to ROM as a source, if this is desired.

MAC-4 has a 4-bit-wide data bus. It can, however, process operands of 4-, 8-, 12-, or 16-bit width. The operand width is determined by a 2-bit field in the processor control register, which is under user control.

Of the remaining six bits in the processor control register, four determine optional autoload and autoincrement functions and the remaining two are spares. An autoload operation replaces a specific pointer by the direct address, and an autoincrement operation adds the operand width to the specific pointer.

I/O and special registers appear in the memory address, where they can be used as source and destination for all instructions; this eliminates the need for special I/O instructions. There is no accumulator, but the addressing modes allow all the RAM space, as well as the memory pointer registers, to function as accumulators. This allows true memory-to-memory data transfer for dyadic operations. There are 43 instructions which can be grouped into four categories: the monadic, the dyadic, the program transfer, and the miscellaneous as shown in Table I.

I/O STRUCTURE

Since MAC-4 was conceived mainly as a controller, it is designed with a flexible I/O structure. Thirty-four out of the 40 pins are dedicated to I/O functions. The input/output modes are selected by the 8-bit I/O control register. The lower four bits control the flow of data among the inport, the I/O bus, and the internal data bus. The upper four bits control the data for DMA in/out, DMA serial/parallel, event counter enable, and interrupt enable.

MAC-4 includes a nonmaskable DMA. The user's program sets the appropriate bits of the I/O control register to handle serial or parallel

Table I—MAC-4 instruction set

Monadic	Dyadic
Add one	Add
Rotate right through carry	Add with carry
Rotate left through carry	Subtract
Subtract one	Subtract with borrow
Complement	Logical AND
Clear	Logical OR
Set	Logical exclusive OR
Set bit	Move bit
Clear bite	
Move	
Program Transfer	**Miscellaneous**
Branch or jump	Short call
Branch or jump if equal	Halt
Branch or jump if not equal	Return
Branch or jump if less than	Interrupt return
Decrement and branch or jump if not zero	PCR override
	Call
Branch or jump if bit is set	
Branch or jump if bit is cleared	
Branch or jump if zero	
Branch or jump if not zero	
Test for zero under mask and jump	

data. A DMA request, generated by pulling the DMA request pin low, causes the processor to complete the current instruction and then relinquishes control to the DMA controller. An asynchronous clock strobes the data in or out. The DMA pointer is incremented at every clock pulse for parallel operation or at every fourth clock pulse for serial operation. An interrupt is generated at the end of the DMA, when the DMA request pin goes high; the program then goes to a DMA service routine.

The DMA pointer can also serve as a 12-bit event counter. Each asynchronous clock pulse increments the pointer. A transition from FFF to 000 results in an overflow that generates an interrupt.

MAC-4 has a single-level maskable interrupt that can be activated by pulsing the pin low while the interrupt enable bit in the I/O control register is set. The interrupt takes place at the end of the current instruction. By using maskable interrupt, DMA, and event count features, three distinct interrupts can be generated.

The user-addressable I/O latches provide 16 pins that may be individually designated as either inputs or outputs. Each latch can be set or reset individually or in groups of four. A 4-bit input port relays data into internal memory directly or indirectly through the user PLA encoder. The user PLA is a mask-programmable matrix which can be used for fast code translation. In addition, data may be fed from the 4-bit input port through the PLA encoder directly to the 8-bit I/O bus. Data can also be written to or read from the I/O bus directly. The I/O bus can be used in a bus-structured environment by using four pins normally employed by the I/O latches for strobing data in or out and for handshaking in a master-slave, or multiprocessor, environment.

ACKNOWLEDGMENTS

MAC-4 is the result of teamwork by the members of the Low End Microprocessor Design Group of the Integrated Circuit Laboratory and the members of the Microcomputer Development Group of the Software and Microprocessor Technology Laboratory. Special thanks are due to D.C. Stanzione for his effort in supervising the Microcomputer Development Group at the beginning of this project.